AN ABSTRACT OF THE THESIS OF

Andrew Bakun for the degree of Doctor of Philosophy in Oceanography presented on October 20, 1987.

Title: Applications of Maritime Data to the Study of Surface Forcing of Seasonal and Interannual Ocean Variability in Eastern Boundary Regions

Redacted for privacy

Abstract Approved: _____

Robert L. Smith

Maritime weather reports are used to define characteristic seasonal patterns of wind stress curl, on a smaller spatial scale than heretofore available, for the four major eastern boundary current systems of the world ocean. Interregional comparisons indicate that: (1) cyclonic wind stress curl overlies regions of eastern boundary counterflows (in conformity with certain theoretical models of these phenomena), (2) surface current patterns parallel wind stress curl contours (suggesting a control on the baroclinic structure of the upper ocean by the horizontal gradient of wind stress curl through differential vortex stretching), and (3) the predominant direction of rotation of oceanic eddies is the same as that of curl of the characteristic regional wind stress pattern. A lack of interregional consistency casts doubt on the hypothesis of

local wind generation of tropical thermal domes.

Maritime data-based time series of monthly indices of sea surface wind stress, wind stress curl, wind-mixing intensity, and ocean-atmosphere heat exchange are produced for 5-degree latitude/longitude quadrangles off the Iberian Peninsula. These are related to interyear variability of coastal sea level and SST evolution by means of simple zero-lag linear regression analysis.

Use of analyzed meteorological fields as a basis for time series is explored. Such series represent variability on larger spatial scales than the 5-degree areal summaries of maritime reports. Higher correlations between alongshore wind stress and coastal sea level, and between wind stress curl and SST evolution, are produced by the larger scale indices of the wind effects. Nonseasonal SST evolution is better correlated with wind stress and wind-induced turbulent mixing (cube of wind speed) when the indices of these wind effects are formulated on the same spatial scale (5-degree areal summaries) as that used to define the SST variation.

Applications of Maritime Data to the Study of Surface Forcing of Seasonal and Interannual Ocean Variability in Eastern Boundary Regions

by

Andrew Bakun

A THESIS

submitted to

Oregon State University

in partial fulfillment of
the requirements for the
degree of

Doctor of Philosophy

Completed October 20, 1987

Commencement June 1988

APPROVED:

Redacted for privacy

Professor of Oceanography in Charge of Major

Redacted for privacy

Dean of the College of Oceanography

Redacted for privacy

Dean of the Graduate School

Date thesis is presented October 20, 1987

Typed by Author

ACKNOWLEDGEMENT

I wish to thank my Major Professor, Dr. Robert L. Smith, and the other members of my Doctoral Committee, Dr. Adriana Huyer, Dr. John S. Allen, Dr. Roger G. Petersen, and Dr. Victor A. Madsen, for their continued help and interest over the extended period of development of this thesis.

The thesis (along with the major portion of my other professional accomplishments) has benefitted greatly from my years of association and collaboration with Craig S. Nelson. Discussions with my colleagues at Pacific Fisheries Environmental Group, Dr. Richard H. Parrish, Dr. Roy Mendelssohn, Mr. Gunter R. Seckel and Mr. David M. Husby, have been extremely helpful. Mr. Art Stroud, of Compass Systems Inc., has made important contributions.

Finally, the continued support and encouragement of the Director of Southwest Fisheries Center, Dr. Izadore Barrett, is gratefully acknowledged.

TABLE OF CONTENTS

LIST OF FIGURES

LIST OF TABLES

APPLICATIONS OF MARITIME DATA TO THE STUDY OF SURFACE FORCING OF SEASONAL AND INTERANNUAL OCEAN VARIABILITY IN EASTERN BOUNDARY REGIONS

I. INTRODUCTION

I.1 "Intermediate" Time and Space Scales

Historically, physical oceanographic science has concentrated a major amount of effort on two quite different combinations of temporal and spatial scales of ocean variation: (1) the oceanwide, climatological-average scales, and (2) the much smaller scales on which field experiments are practical.

Early expeditions were designed to explore the range of observable phenomena and so tended to choose ocean basin scale, and even inter-ocean scale, cruise tracks; because of practical limits on the time spent at sea between port calls, the station spacing tended to be very coarse. Since a particular location would ordinarily be visited only once, the temporal focus was on the climatological mean. The customary method for defining ocean flow features has been the "dynamic method" of geostrophic current calculations based on arrays of hydrographic stations. The method assumes stationarity over the periods required to occupy a large scale station array, leading again to a focus on the nonvarying components. The other major source

of information on ocean flow has been the "ship drift" observations which are assembled to aid navigation. The flow features that have been of greatest interest to navigators are the intense western boundary currents and equatorial currents of the Atlantic and Pacific Oceans, for which the variability in transport is rather subtle compared to the mean flow. Thus, in the years following the Second World War, an awakened interest in physical oceanographic theory tended to focus primarily on the long term mean behavior of the ocean system on the scale of such grandiose features as the great subtropical current gyres and their major components, i.e., the western boundary currents, the equatorial currents, etc.

More recently, as physical oceanography has begun to work through the maturation process typical of a scientific field, i.e., from the exploratory phase toward the experimental phase, focus has shifted to the time and space scales that can be addressed by reasonably-sized field efforts. A tendency has been to address variability on the atmospheric event scale time scales of about one day to several weeks, and on spatial scales of tens of kilometers or less.

However, some of the most important applications of ocean science to the larger problems of human society lie in the range of scales between these two extremes. Because the seasonal cycle is not only the largest signal of

variability in the system but also the most regular and predictable, the activities of human beings and the life cycles of marine organisms of economic interest are highly tuned to the normal march of the seasons. Disruptions of the regular seasonal progression, represented by interyear (nonseasonal) variability, can provoke unfortunate consequences, even when rather small (compared to the expected, and adapted for, seasonal range).

A characteristic of most marine organisms is that they have at least one "weak link" in their life cycle processes, in which their survival is nearly entirely at the mercy of the ocean system. Complex, highly-tuned larval drift strategies (e.g., Parrish et al., 1981), stringent requirements for sporadically-abundant specific types of food particles (e.g., Lasker, 1978), etc., result in extreme variations in annual reproductive success. For example, in populations of fishes such as anchovies, sardines, and mackerels, the ratio between parental stock size and eventual recruitment of their progeny to the adult population, typically varies from year to year by factors up to several hundred.

Recent abrupt declines of important fishery stocks around the world (e.g., Fig. I.1) have had severe socio-economic impact. In conventional fishery management models and procedures, the portion of the production of a fish stock which is available for exploitation is assumed to be

a relatively constant function of stock size. However, recent events have proven this assumption to be woefully inadequate to the task of managing fishery resources under environment perturbation. In order to focus the efforts of the oceanographical scientific community on this crucial set of problems, a new program entitled "Ocean Science in Relation to Living Resources (OSLR)" (e.g., Bakun et al., 1982) has been adopted by the Intergovernmental Oceanographic Commission (IOC) as a major new international scientific initiative; the Food and Agriculture Organization of the United Nations (FAO) has joined IOC as a full co-sponsor of the OSLR program.

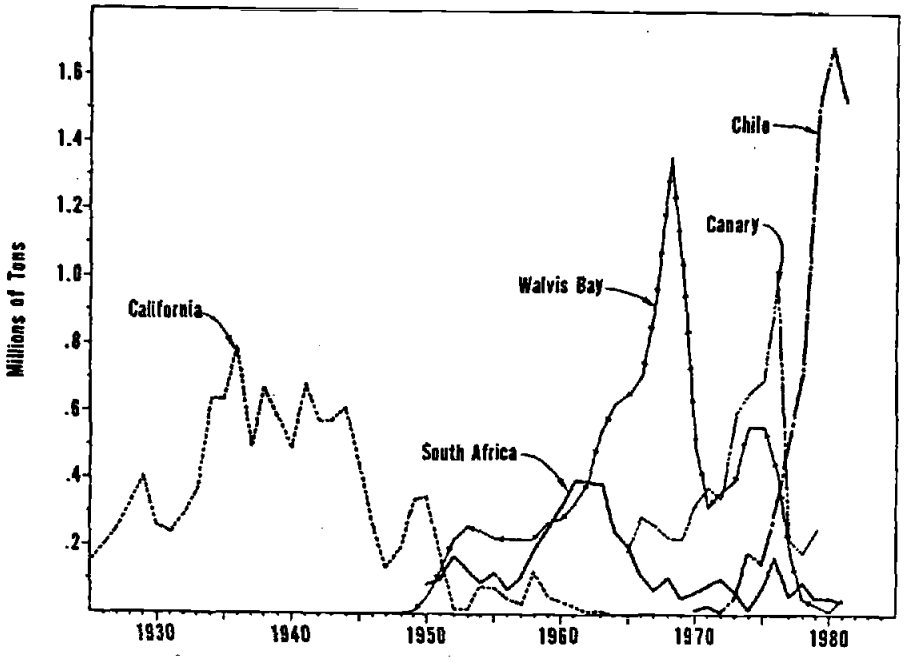

Figure I.1. Annual sardine landings from several eastern boundary current stocks (after Parrish et al., 1983). "Walvis Bay" and "South Africa" refer to the two major Benguela Current stocks.

The scales on which important marine fish stocks grow and reproduce (and fluctuate) are the spatial scales of tens to hundreds of kilometers which define feeding and reproductive habitats, and temporal scales from weeks to decades. These are the scales that must be addressed to promote the most immediate application of ocean scientific findings to living marine resource problems.

The other major impact of ocean variability on human society is through the linkage of the ocean to short term climatic variability. Most major scientific efforts in this problem area, e.g., the international "El Nino", "TOGA", and "WOCE" programs, etc., address the very large spatial scales representing the major couplings of the earth's atmosphere-ocean system. However, there is evidence that ocean conditions on a regional or sub-regional scale may be capable of exerting significant influence on the local climate of adjacent coastlands (e.g., Bakun, 1978).

Using expensive dedicated platforms such as research ships to secure continuous data coverage of seasonal and interannual scales of variability, on regional spatial scales, has not generally proven practical.

I.2 Maritime data

By international convention, weather observations are recorded routinely by a variety of ships operating at sea. These maritime reports remain the primary source of

information on variability in the marine environment. Even with the rapid development of satellite-based observation systems, analysis of time series of inter-decadal length must continue to depend heavily on maritime reports for some time to come. Observations of wind speed and direction, sea and air temperature, atmospheric pressure, humidity, and cloud cover included in these reports provide a basis for estimating a number of environmental variables pertinent to the scientific study of ocean variability.

Maritime reports are subject to a variety of errors, of which improper positioning is perhaps the most troublesome, sometimes introducing very large errors in all derived quantities (e.g., when a wrong hemisphere is indicated in report coding.). It is difficult to establish effective procedures for rejecting erroneous reports without running the risk of suppressing indications of real variability. For example, early indications of the 1982-83 El Nino event went unnoticed by meteorological agencies in Europe and North America because the reports, which clearly indicated an event of unprecedented intensity, were so far from the norm that they were rejected as erroneous by the automated data-editing procedures (Siegal, 1983). In addition, even where no actual errors are involved, irregular distribution of reports, in both time and space, may introduce biases and non-homogeneities into time series constructed from these data.

However, time series of ocean properties and processes, constructed from simple areal summaries of such reports, have been presented as indicators of ocean variability (e.g., Bakun, 1987). This thesis explores the scientific utility of maritime data and demonstrates several approaches to their application.

I.3 The Comparative Method.

The comparative method and the better-known experimental method are "the two great methods of science" (Mayr, 1982). The comparative method is particularly applicable to situations not amenable to controlled experiments; for example, it has been the basis for nearly all of the revolutionary advances in evolutionary biology (ibid.). Certainly, the ocean-atmosphere system qualifies as being nearly totally uncontrollable in its dynamic aspects. In addition, to comparison among different geographical situations, etc., comparison among different time periods (i.e., time series analysis), can also be viewed as an application of the comparative method, although care must be taken to remove serial correlation that would invalidate the assumption that we are viewing independent realizations of a process of interest.

The following two chapters of this thesis constitute an application of the comparative scientific method to the different regional eastern ocean boundary systems.

Seasonal and geographical patterns of curl of the wind stress on the sea surface are defined from the historical maritime data base. Patterns of correspondence to known aspects of ocean conditions, particularly flow, provide insights into the effects of vorticity transfer from the atmosphere on the ocean vorticity budget. In the final two chapters, the comparative focus switches to time series analysis, exploring the problems involved in (1) the production of time series based on maritime data and (2) the application of such series in empirical studies of the processes leading to interyear variability in the marine ecosystem.

II. THE ANNUAL CYCLE OF WIND STRESS CURL IN SUBTROPICAL EASTERN BOUNDARY CURRENT REGIONS

II.1 Introduction

The curl of the wind stress acting on the sea surface is a fundamental forcing agent for dynamic ocean processes. It stands out as the external input term in ocean model formulations expressed in terms of vorticity balance. The same process, when considered from the point of view of vertical structure in the flow field, appears as the divergence of surface Ekman transport. Wind stress curl thus controls 'Ekman pumping' and associated vertical advection in regions seaward of the immediate effects of coastal boundaries, and so has a variety of physical, chemical, and biological consequences to the ocean ecosystem. These include alterations of the internal density structure of the upper ocean, corresponding alterations of the horizontal flow field, and vertical transfers of physical and chemical properties having well known biological effects.

No actual measurements of wind stress curl are available except in rare instances where arrays of research ships or buoys take coordinated wind measurements. Synoptic samplings of maritime reports may adequately define very large scale variations (i.e., thousands of km)

in the wind stress curl pattern, but not the intermediate scales (tens to hundreds of km) on which very important ocean responses and biological effects are expected to occur.

In this chapter, the characteristic annual variations of wind stress curl patterns over the eastern ocean boundary regions containing the California, Canary, Benguela, and Peru Current systems are defined on smaller spatial scales than have been previously achieved. Maritime data from a large number of years are composited together to yield mean wind stress patterns on much smaller scales than ever definable in synoptic samples of these data. Because the seasonal cycle is highly periodic, interyear variability is suppressed by compositing many years together, revealing characteristic seasonalities. Since the curl is a linear mathematical operator, the field of curl of the mean stress will, as sampling error decreases, tend increasingly to resemble the true mean field of the curl of the stress.

Various estimates of larger scale characteristic wind stress curl fields over the oceans have been published. Evenson and Veronis (1975) used spline functions to smooth Hellerman's (1967) 5-degree latitude/longitude average stress estimates to compute very large scale wind stress curl fields for the oceans. Leetmaa and Bunker (1978) presented seasonal charts for the North Atlantic based on

finite difference derivatives computed among 2-degree latitude by 5-degree longitude areal samples of wind stress estimates. Hastenrath and Lamb (1977) presented monthly charts for the tropical Atlantic and eastern tropical Pacific based on one-degree summaries of mean monthly wind velocity; since the estimate of stress from wind velocity is a nonlinear procedure, the validity of their results depends on an assumption of no substantial seasonal, spatial or directional dependence of the functional relationship of the variance of the wind velocity to its mean. Thus, the procedures of Nelson (1977) and Leetmaa and Bunker (1978), whereby the stress is estimated from each observation before averaging, are definitely preferable. In addition, Hastenrath and Lamb apply a spatial smoothing filter, covering 5 degrees of both latitude and longitude, to their stress estimates before calculating the curl; thus they obscure the one-degree resolution of their original report summaries. Wyrtki and Meyers (1976) computed curl from averages of reports within 2-degree latitude by 10-degree longitude quadrangles in the tropical Pacific Ocean. Goldenberg and O'Brien (1981) subjectively transferred Wyrtki and Meyers' distributions to a 2-degree grid, a procedure that does not improve the actual data-based resolution. Hellerman and Rosenstein (1983) used 2-degree latitude/longitude areas for summarizing stress estimates for the world ocean, and

suppressed small scale detail with a sixteen-point linear smoother.

The finest-scale distributions of wind stress curl that have been published are Nelson's (1977) mean monthly charts for the California Current region. The curl is computed from one-degree summaries of stress estimates made from individual reports. No smoothing of data was performed before or after the curl calculation. As the taking of spatial derivatives amplifies sampling errors present in the stress fields, the resulting curl fields are quite "noisy". However spatial coherence of independent curl estimates reveals significant features previously unknown.

For example, a lobe of anticyclonic curl extends from the offshore region, where anticyclonic curl generally predominates, to the coast of central Baja California. This feature is evident in all twelve independent monthly distributions. During the season of relaxed upwelling the surface circulation pattern appears to break up into cyclonic gyres occupying the regions of cyclonic curl to the north and south, separated by the lobe of anticyclonic curl (Bakun and Nelson, 1977).

Hickey (1979) has compared the seasonal features in Nelson's charts with known features in California Current flow patterns; she suggests that except for the near-coastal region north of Cape Mendocino, flow throughout the region may be directly driven by the wind stress curl in a

"Sverdrup balance" sense. Chelton (1980) has indicated that interyear variability in zonal shear in the flow of the California Current may be linked to wind stress curl through a mechanism of alteration of the baroclinic structure by Ekman pumping.

Correspondence to biological features has also been noted. Areas of cyclonic curl near the coast appear to be favorable for fish reproduction, being occupied by separate subpopulations of pelagic fishes (Nelson, 1977). Parrish and MacCall (1978) found long term variations in wind stress curl, indicated in monthly mean atmospheric pressure distributions, to be correlated with indices of reproductive success of Pacific mackerel. Parrish, Nelson, and Bakun (1981) point out that large stocks of migratory pelagic fishes feed in the offshore region where anticyclonic wind stress curl (i.e., Ekman convergence) predominates; the suggestion is that oceanic food web organisms may be concentrated in convergent surface fronts in that region, providing particularly favorable feeding conditions for the large fishes.

Hellerman and Rosenstein (1983) show anticyclonic curl over the majority of the California Current region during winter (their January distribution). This is at variance with Nelson's (1977) distributions which show cyclonic curl prevailing within several hundred km of the coast from San Francisco to Punta Baja in Northern Mexico. Apparently,

Hellerman and Rosenstein's procedures, being designed to indicate features affecting ocean basin scale circulation, fail to resolve near-coastal features in the wind stress curl distributions which are probably very important dynamically and ecologically along eastern ocean boundaries.

Nelson's (1977) computational grid contains intersections at one-degree latitude/longitude intervals, each intersection being the center of a one-degree "square" area within which stress estimates, based on each individual available report, are averaged by component. The curl calculation employs central difference derivatives, except at the grid edges. These derivatives span three grid intersections in both the zonal and meridional directions, thereby incorporating data over spans of three degrees of both latitude and longitude in each computed value of the curl; the distance scale for the derivative is fixed at two degrees latitude or longitude (Fig. II.1a). This scale of computation is comparable to the sizes of important features which we wish to resolve.

For example, the indicated line of zero curl, where divergence in the large scale surface Ekman transport field changes to convergence, Ekman pumping changes from upward to downward, "Sverdrup transport" changes from poleward to equatorward, etc., appears to lie at about two degrees longitude distance off much of the west coast of the United

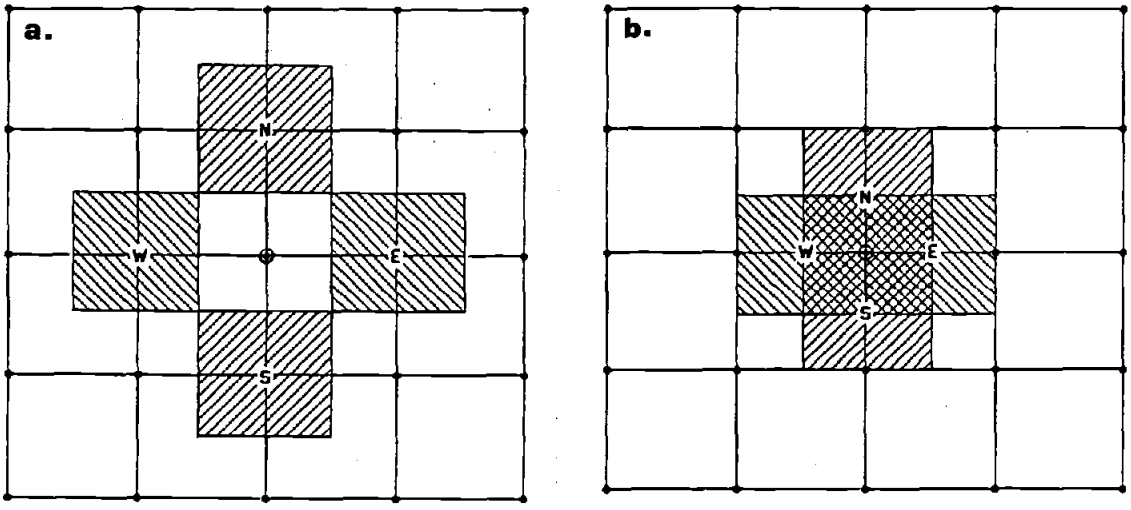

Figure II.1. Illustrations of spatial aspects of wind stress curl calculations on one-degree latitude/longitude computation grids. Meridional derivatives at circled grid intersection in the center of each illustrated grid segment are formed from averages of zonal stress component observations occurring in the hatched one-degree areas labeled 'N' and 'S'. Zonal derivatives are formed from meridional stress components observed in the hatched areas marked 'E' and 'W'. **(a)** Central difference scheme of Nelson (1977); centers of summary areas are 2 degrees apart, yielding a 2-degree basic length scale for the derivative computations. **(b)** Scheme used in the present study; summary areas for the separate components overlap, allowing a one-degree basic length scale for the respective derivative computations.

States. This is a scale where the coastward end of the zonal derivative computation is affected by reports that may lie in the lee of capes, within coastal bights, etc., which may thereby control the derived curl features at some distance offshore. An indication of this effect is seen in Nelson's distributions as seaward extentions of coastal cyclonic curl features north and south of Cape Blanco and in the coastal bight near San Francisco Bay.

In the present work, sea surface wind stress patterns are generated on an even smaller scale (one-degree rather than two-degree distance scale for the derivative computation). An additional first-order correction for non-even distribution of reports within a given one-degree square summary area is also added, by adjusting for the differences between the mean latitude and longitude of the reports and the geographic center of the summary area; this avoids the possibility of grossly erroneous curl magnitudes in cases where reports may be concentrated along narrow shipping lanes which may not cross near the center of the one-degree square, etc. These higher resolution distributions are intended to serve as checks for scale-related artifacts in Nelson's results for the California Current region. Corresponding distributions for the similar eastern boundary current regions of the North and South Atlantic, and of the South Pacific, are intended to provide indications of the generality of the various features and

to constitute a basis for applying the comparative method to draw conclusions as to their dynamical and ecological significances.

2.2 Computational Method

Sampling errors in the stress summaries are amplified by the differencing procedures in the curl computation. Thus it is especially important to minimize sampling errors by incorporating the largest possible data base in each sample. Therefore we wish to retain the one-degree areal sample size in the basic stress summaries as used by Nelson (1977). The reduced scale of the computation is herein achieved by "staggering" the grids of one degree areal samples of the respective zonal and meridional stress components by one-half degree in both latitude and longitude (Fig. II.1b). This allows derivatives on a finite difference span of basically one degree, while retaining independent one-degree areal samples of the respective components involved in each curl calculation.

The vertical component of the curl of the wind stress on the sea surface, $\vec{k}\cdot\nabla\times\vec{\tau}$, is calculated as

$$\vec{k}\cdot\nabla\times\vec{\tau} = \frac{1}{R}\left(\frac{1}{\cos\phi}\frac{\partial\tau_\phi}{\partial\lambda} - \frac{\partial\tau_\lambda}{\partial\phi} + \tau_\lambda\cos\phi\right) \qquad (2.1)$$

where R is the mean radius of the earth, ϕ and λ are the latitudinal and longitudinal coordinates (in radians), and

$\frac{\partial \tau_\lambda}{\partial \phi}$ and $\frac{\partial \tau_\phi}{\partial \lambda}$ are the meridional derivative of zonal stress and the zonal derivative of meridional stress respectively.

In finite difference form, equation 2.1 becomes

$$\vec{k} \cdot \nabla \times \vec{\tau} = \frac{1}{R \cos\phi} \left(\frac{\tau_{\phi(N)} - \tau_{\phi(S)}}{\Delta \lambda} - \frac{\tau_{\lambda(E)} \cos\phi_{(N)} - \tau_{\lambda(W)} \cos\phi_{(S)}}{\Delta \phi} \right) \qquad (2.2)$$

where $\tau_{\lambda(N)}, \tau_{\lambda(S)}, \tau_{\phi(E)}, \tau_{\phi(W)}$, are the averages of the stress component estimates in the four one-degree summary areas involved in a given calculation (Fig. II.1b) and $\Delta\phi$ and $\Delta\lambda$ are the respective differences in the mean latitudes in the two areal segments involved in the meridional derivative and the mean longitudes in the two segments involved in the zonal derivatives.

The stress estimates are computed from individual reports according to the usual formula

$$\vec{\tau} = \rho_a C_D U \vec{v} \qquad (2.3)$$

where $\vec{\tau}$ is the stress vector, ρ_a is the density of air, C_D is a dimensionless drag coefficient, $\vec{v}$ is the wind velocity, and U is the wind speed. C_D and ρ_a are held constant (0.0013 and 0.00122 g cm^{-3}). Nelson (1977) compared climatological stress and stress curl patterns produced in this manner to corresponding patterns produced using drag coefficients which vary with wind speed and boundary layer stability; no significant differences in

locational aspects appeared.

For estimating sampling error, the characteristic long term seasonal stress distributions are considered to be sufficiently well sampled for the standard error of the mean to provide a reasonable estimate of error. Accordingly, the variances of the one-degree stress component samples are carried through the curl calculation according to the usual rules (e.g., Beers, 1953), i.e.,

$$\sigma^2_{CURL} = \frac{1}{R\Delta\phi}\left(\cos\phi(N)\,\sigma^2_{\tau_{\lambda(N)}} + \cos\phi(S)\,\sigma^2_{\tau_{\lambda(S)}}\right) + \frac{1}{R\cos\phi\Delta\lambda}\left(\sigma^2_{\tau_{\phi(E)}} + \sigma^2_{\tau_{\phi(W)}}\right) \qquad (2.4)$$

where σ^2_{CURL} represents the variance of the curl estimate; $\sigma^2_{\tau_{\lambda(N)}}$, $\sigma^2_{\tau_{\lambda(S)}}$, $\sigma^2_{\tau_{\phi(E}}$, $\sigma^2_{\tau_{\phi(W)}}$, represent the variances of the estimates of the stress components appearing in Eq. 2.2.

II.3 Construction of the Maps

The computational grids are set along the mainly meridional portions of the continental boundaries of the four regions (Fig. II.2), so as to cover the "classical" equatorward eastern boundary current flows and the associated "temperate" coastal upwelling systems. Available data density is highly variable among regions and within regions (Fig. II.3).

Previous to 1950, a large percentage of the available maritime reports contain positions reported only to the nearest whole degree of latitude. These are not amenable

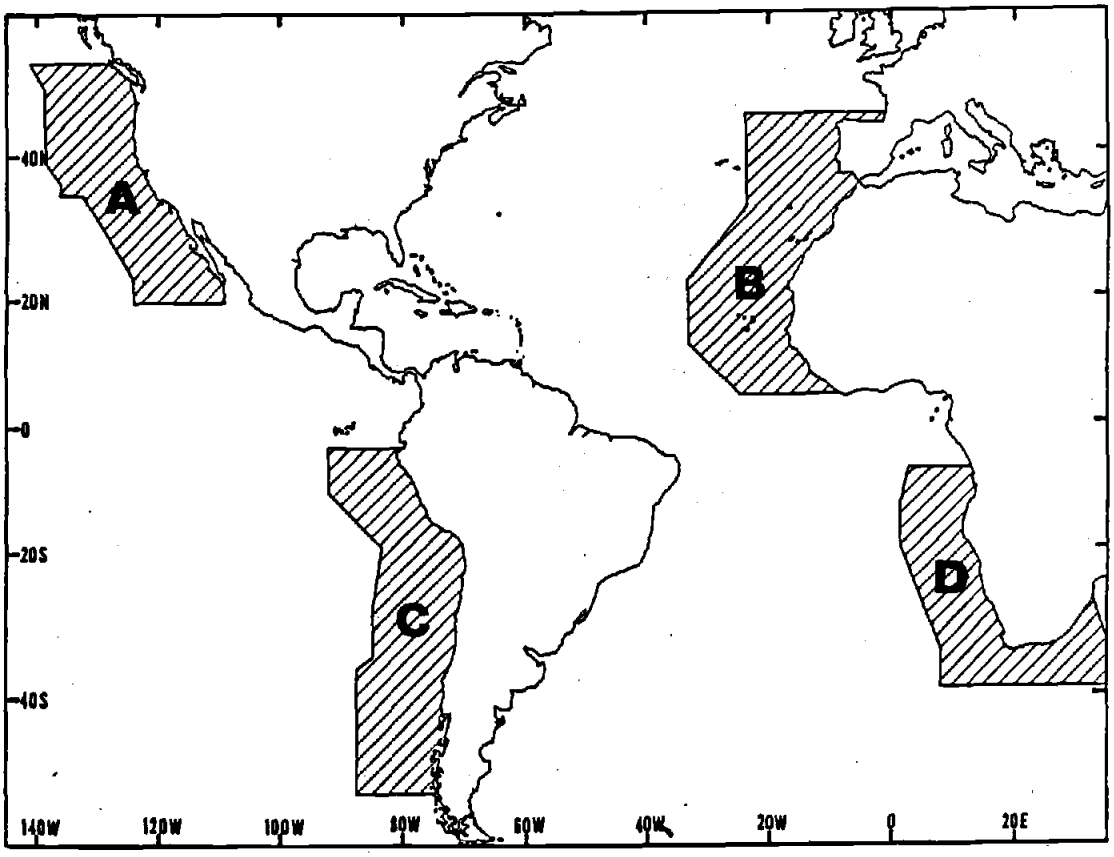

Figure II.2. Geographic orientation of study areas. Hatched areas delineate the areas within which wind data were summarized by one-degree areal quadrangles, as a basis for calculation of the wind stress curl distributions herein presented. A. California Current region; B. Canary Current region; C. Peru/Humboldt Current region; D. Benguela Current region.

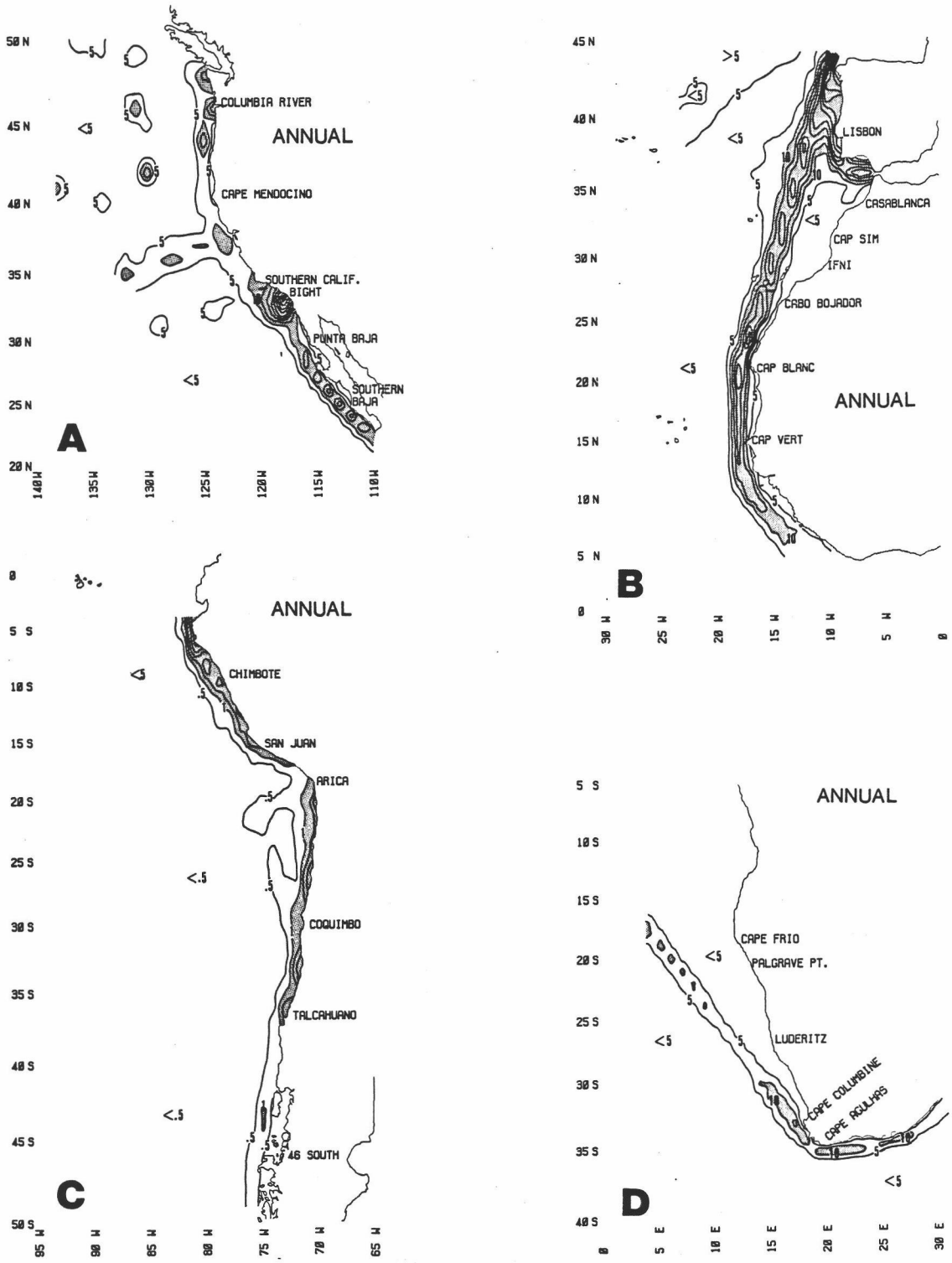

Figure II.3. Density of maritime wind observations (up to 1979) available in the historical data files (after Parrish et al., 1983). Units are thousands of observations per one-degree latitude/longitude quadrangle. The four panels depict the areas defined in Fig. II.2: A. California Current region; B. Canary Current region; C. Peru/ Humboldt Current region; D. Benguela Current region.

to the staggered grid computation scheme in which the samples of the respective stress components are offset by one-half degree in each coordinate direction. Accordingly, the 30-year period, 1950-79, has been chosen as the basic time frame for compositing data to construct the stress fields. One deviation from this procedure, applied in the construction of the Peru-Humboldt Current regional distributions, is discussed in Section II.7.

No smoothing of the stress component fields is performed prior to the curl computation. This results in quite noisy computed curl distributions, particularly in regions of low data density where substantial sampling errors are amplified by the process of taking spatial derivatives. However the choice was made to maintain spatial independence on the small scale (only directly adjacent curl estimates share data) in order to reveal small scale features which are substantial enough to stand out from the noise. Several steps were taken to deal with the noise to yield significant, recognizable wind stress curl patterns.

In addition to the 2-month segments of the seasonal cycles presented in Figs. II.4 to II.7, independent one-month mean distributions were also prepared and submitted to the various treatments enumerated below; these provide dual independent checks on the features defined in the 2-month composite distributions. Preliminary machine-

contoured maps of all the one-month and two-month distributions, in their original untreated state, were prepared as a first step in the process of constructing characteristic distributions.

Companion maps of discrete symbols indicating both magnitude and standard error for each grid point estimate were also prepared for all the one-month and two-month distributions. These provided a readily referenced estimate of the reliability of each computed curl value. Another guide to significance was provided by the degree of spatial and temporal coherence of independent estimates (features coherently indicated on larger scales than 2-degree quadrangles and in both single-month subsamples of a two-month set were assigned high probability of reality). The intention was to lean toward conservatism in the subjective construction process, i.e., to avoid defining features of questionable reality.

Finally, maps of spatially smoothed two-month curl distributions were prepared and objectively contoured by machine. A nonlinear smoother was employed. The usual linear smoothing techniques were deemed inadequate in this case as they merely spread the intense "bulls-eyes" which largely obscured the underlying significant pattern in the more data-poor areas. Rather, a 3 by 3 gridpoint version of the median smoother (Tukey, 1977) was employed, whereby the value at each grid location was replaced by the median

of the nine values in the 3 by 3 grid segment centered at the location. The alongshore and offshore directions were considered to be more appropriate as coordinates for smoothing than the geographical (latitude/longitude) coordinates and so the filter was applied along the grid with the 3 by 3 elements oriented so as to most closely align with the alongshore and offshore normal directions with respect to the general trend of the coast at the given latitude.

These filtered maps formed an initial basis for the construction of the distributions. Details that may have been lost in the filtering process, but were indicated as significant by the examinations described above, were added by overlaying the smoothed and unsmoothed contoured distributions on a light table and drawing in the final contours while continually referring to the one-month subsample distributions, and to the maps of discrete symbols carrying the standard error indicators, etc., as guides. This subjective process was necessary to extract the maximum amount of information supported by the data. Note that the entire process was applied independently to each two-month sample set. No conscious transfer of information between sample sets was allowed. In fact, efforts were made to ensure that any error would be on the side of overavoidance of any possible transfer of information. The maps presented in Figs. II.4 to II.7 are thus

based as independently of one another as possible, in spite of the subjective aspects of their construction. No "after the fact" re-contouring, etc., to bring indicated features into better conformity among different maps, even where the data might have (after re-examination) supported it, has been performed.

Regions characterized by anticyclonic curl, i.e., clockwise in the northern hemisphere and anti-clockwise in the southern hemisphere, are shaded in the maps (Figs. 2.4 to 2.7). Thus, shaded regions are those in which the surface Ekman transport is convergent, Ekman pumping is downward from the surface Ekman layer, and theoretical depth-integrated Sverdrup transport is equatorward. Conversely, unshaded areas indicate cyclonic curl (anti-clockwise in the northern hemispere and clockwise in the southern hemisphere) and corresponding characteristic surface Ekman divergence, upward Ekman pumping, oceanic upwelling, and poleward Sverdrup transport.

II.4 The California Current Region

Anticyclonic wind stress curl, associated with the generally equatorward wind flow within the eastern leg of the North Pacific Subtropical Anticyclone, dominates the offshore portions of the California Current region (Fig. II.4). Adjacent to the coast, the wind stress curl tends to be cyclonic. Thus Ekman divergence dominates at the

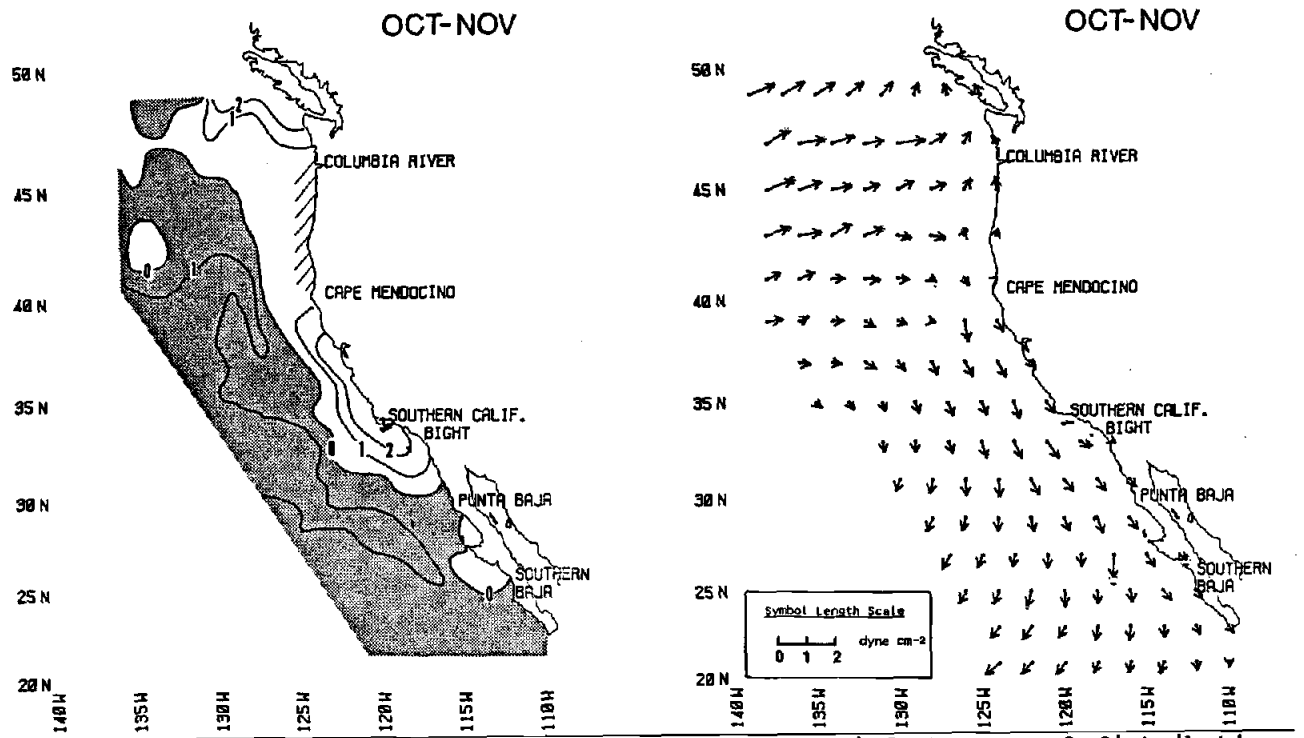

Figure II.4a. California Current region. *Left panel:* Wind stress curl distribution during October-November. Units are dyne cm^{-2} per 1000 km; regions of anticyclonic wind stress curl are shaded and regions of cyclonic wind stress curl are unshaded. *Right panel:* Sea surface wind stress vectors (shown only at alternate grid intersections); symbol length scale shown at lower left of panel; dotted ellipses at head of vector symbols indicate computed standard errors of the vector components.

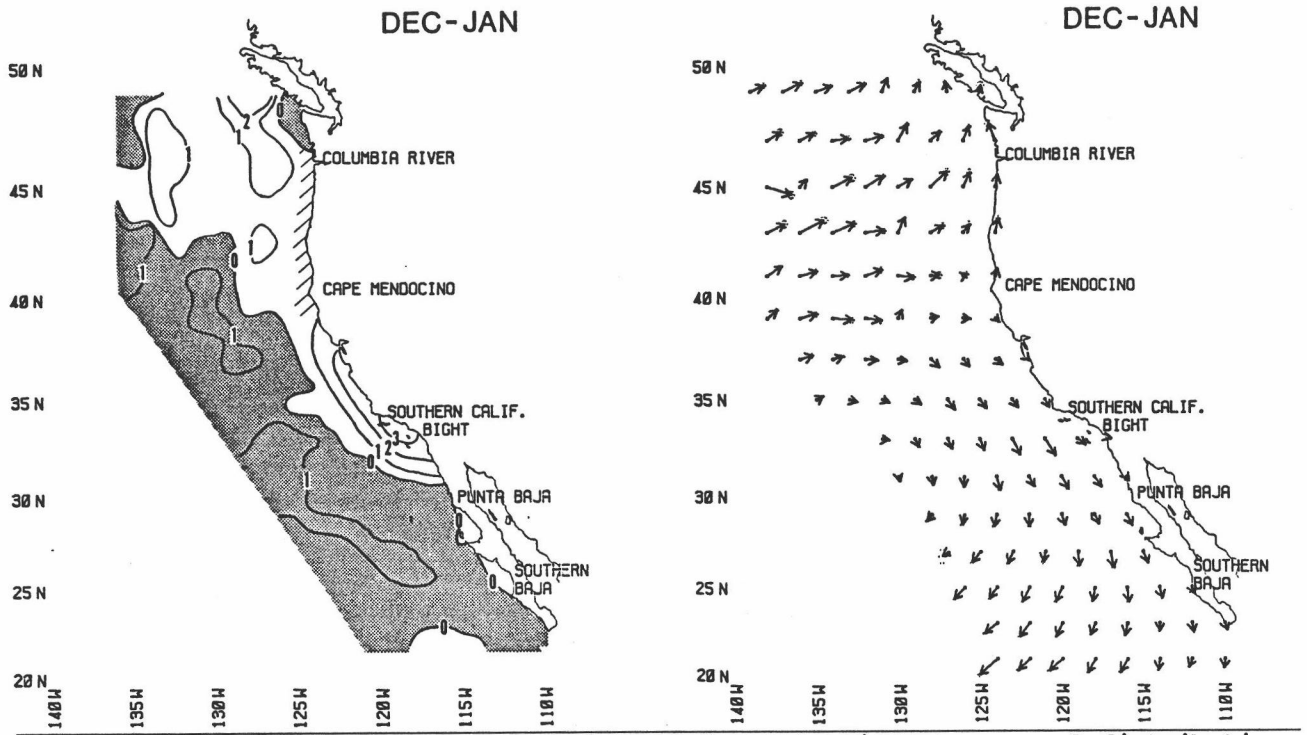

Figure II.4b. California Current region. *Left panel:* Wind stress curl distribution during December-January. Units are dyne cm^{-2} per 1000 km; regions of anticyclonic wind stress curl are shaded and regions of cyclonic wind stress curl are unshaded. *Right panel:* Sea surface wind stress vectors (shown only at alternate grid intersections); symbol length scale shown at lower left of panel; dotted ellipses at head of vector symbols indicate computed standard errors of the vector components.

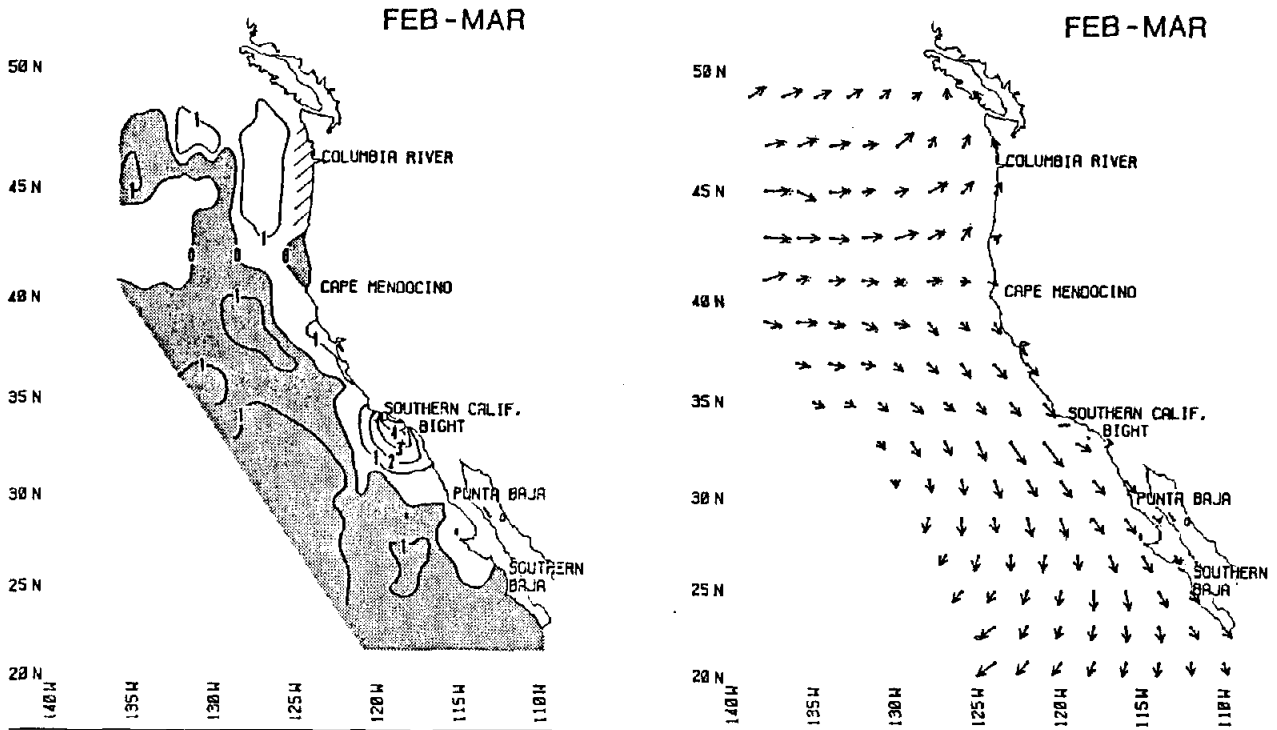

Figure II.4c. California Current region. *Left panel:* Wind stress curl distribution during February-March. Units are dyne cm^{-2} per 1000 km; regions of anticyclonic wind stress curl are shaded and regions of cyclonic wind stress curl are unshaded. *Right panel:* Sea surface wind stress vectors (shown only at alternate grid intersections); symbol length scale shown at lower left of panel; dotted ellipses at head of vector symbols indicate computed standard errors of the vector components.

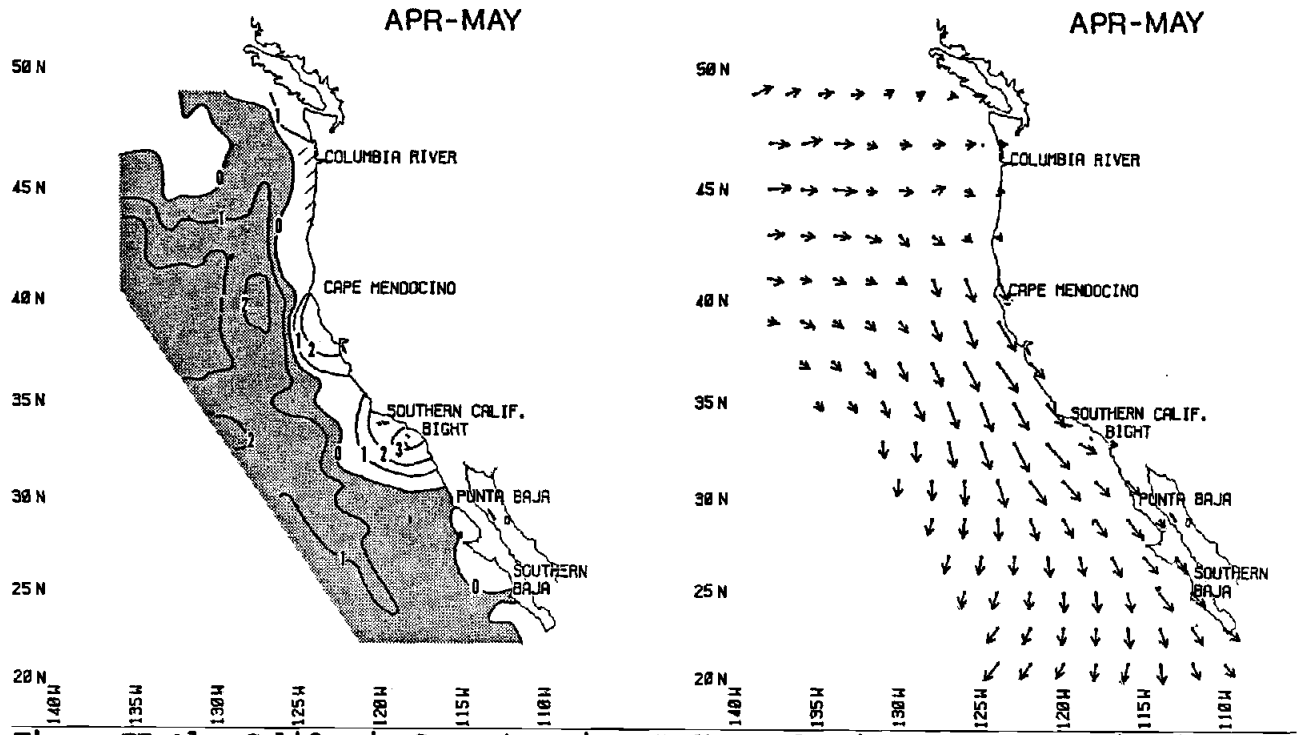

Figure II.4d. California Current region. *Left panel:* Wind stress curl distribution during April-May. Units are dyne cm^{-2} per 1000 km; regions of anticyclonic wind stress curl are shaded and regions of cyclonic wind stress curl are unshaded. *Right panel:* Sea surface wind stress vectors (shown only at alternate grid intersections); symbol length scale shown at lower left of panel; dotted ellipses at head of vector symbols indicate computed standard errors of the vector components.

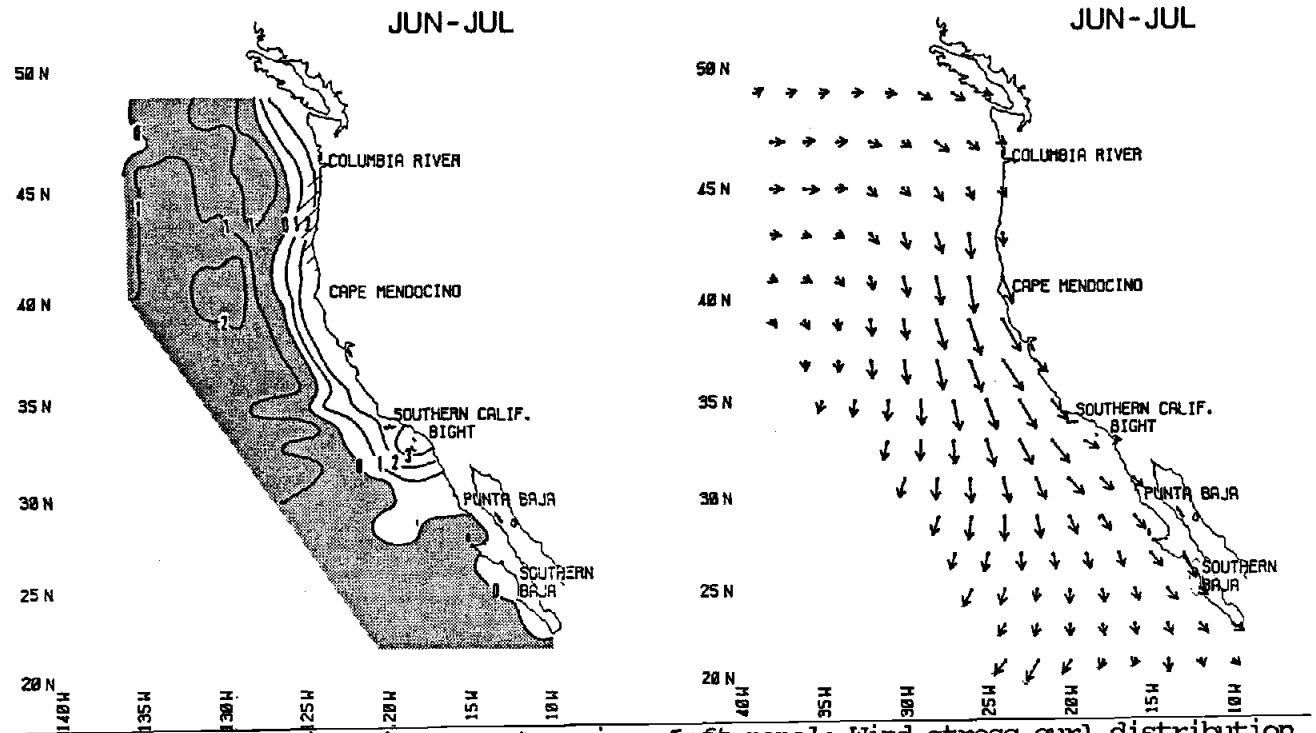

Figure II.4e. California Current region. *Left panel:* Wind stress curl distribution during June-July. Units are dyne cm^{-2} per 1000 km; regions of anticyclonic wind stress curl are shaded and regions of cyclonic wind stress curl are unshaded. *Right panel:* Sea surface wind stress vectors (shown only at alternate grid intersections); symbol length scale shown at lower left of panel; dotted ellipses at head of vector symbols indicate computed standard errors of the vector components.

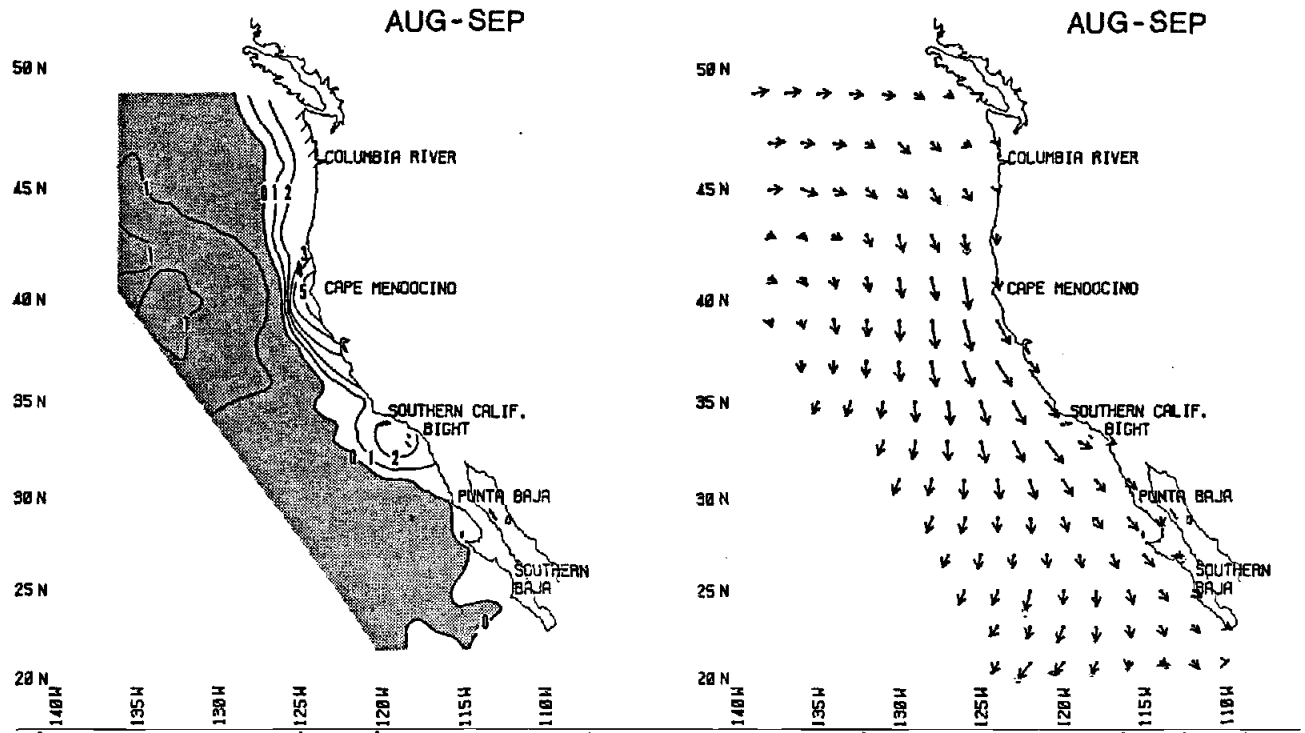

Figure II.4f. California Current region. *Left panel:* Wind stress curl distribution during August-Seeptember. Units are dyne cm^{-2} per 1000 km; regions of anticyclonic wind stress curl are shaded and regions of cyclonic wind stress curl are unshaded. *Right panel:* Sea surface wind stress vectors (shown only at alternate grid intersections); symbol length scale shown at lower left of panel; dotted ellipses at head of vector symbols indicate computed standard errors of the vector components.

ocean surface near the coast and Ekman convergence is dominant in the offshore region.

A local maximum of cyclonic curl is associated with the Southern California Bight, throughout the year. During fall and winter (Figs. II.4a and II.4b) there is a tendency for a lobe of substantial cyclonic curl to extend northward along the coast from the Southern California Bight, nearly reaching Cape Mendocino. In late winter and spring (Figs. II.4c and II.4d) this lobe has divided to form a second local maximum extending south from Cape Mendocino to include the area off San Francisco and Monterey Bays. By early summer, when the seasonal coastal upwelling regime has extended northward to occupy essentially the entire coastline of the region (Bakun, et al., 1974), strong cyclonic curl is the rule along nearly the entire coastline of the region (Fig. II.4e). In late summer, the strongest wind stress curl in the region tends to be located adjacent to Cape Mendocino (Fig. II.4f).

Throughout the year, there is a consistent tendency for a lobe of anticyclonic curl to penetrate coastward from the offshore region to contact the coast of Baja California in the vicinity of Punta Baja, separating cyclonic curl regions to the north and south. Punta Baja is the site of the local maximum in coastal upwelling (Bakun and Nelson, 1977); this then is an exception to a pattern noted elsewhere in the region (and also in the other regions shown in

Figs. II.5, II.6, and II.7), of cyclonic curl extending some hundreds of km seaward of coastal upwelling regimes (although, in view of lateral frictional effects, it seems likely that a boundary layer of cyclonic curl, which may be too narrow to be resolved by our procedures, may exist very near the coast in the vicinity of Punta Baja).

Diagonal hatching in the area off the coast of the Pacific Northwest, shown in Fig. II.4, is inserted to indicate an apparent tendency for anticyclonic wind stress curl to exist very near the coast. The unsmoothed monthly distributions in this region have a particularly noisy appearance, with indications of generally cyclonic curl being interrupted by intense "bulls-eyes" of anticyclonic curl, which are generally confined to a single gridpoint and are characterized by particularly large computed standard errors. When the averaging period is expanded these bulls-eyes tend to coalesce, so that in the composite annual mean the area directly adjacent to the coast is predominently occupied by anticyclonic wind stress curl. On the scale of these computations, the situation very near the Oregon and Washington coasts appears to be a variable mixture of more persistent weak cyclonic curl (perhaps related to lateral boundary layer effects in situations where winds are directed equatorward), broken intermittently by more intense episodes of anticyclonic curl (perhaps related to poleward winds associated with storm

systems). Craig S. Nelson (personal communication) has summarized stress estimates on an even smaller scale (0.2 degree latitude/longitude summary areas) and found certain indications of a characteristic maximum of equatorward wind stress within about 10 km of the coast.

In general, the offshore scale of major wind stress curl features exhibited in Fig. II.4 is not greatly different than shown in Nelson's (1977) distributions. The conclusion is that the effect of scale of the computations has not produced any significant misrepresentations of offshore extents, etc., in Nelson's earlier work.

II.5 The Canary Current Region

North of about 15° N lat, the Canary Current region (Fig. II.5) exhibits a similar general dominance of anticyclonic wind stress curl in the offshore area and cyclonic curl adjacent to the coast. Near 15° N lat, the anticyclonic curl tends to be truncated by a zonal band of cyclonic curl that extends seaward to beyond the area treated in this study. During fall (Fig. II.5a) cyclonic curl maxima are located in coastal bights off Ifni and between Cap Blanc and Cap Vert. As the season progresses the maxima shift to positions more directly associated with major capes. Particularly strong curl lies directly adjacent to Cap Sim during the spring and summer (Figs. II.5d and II.5e), the seasons of vigorous coastal upwelling

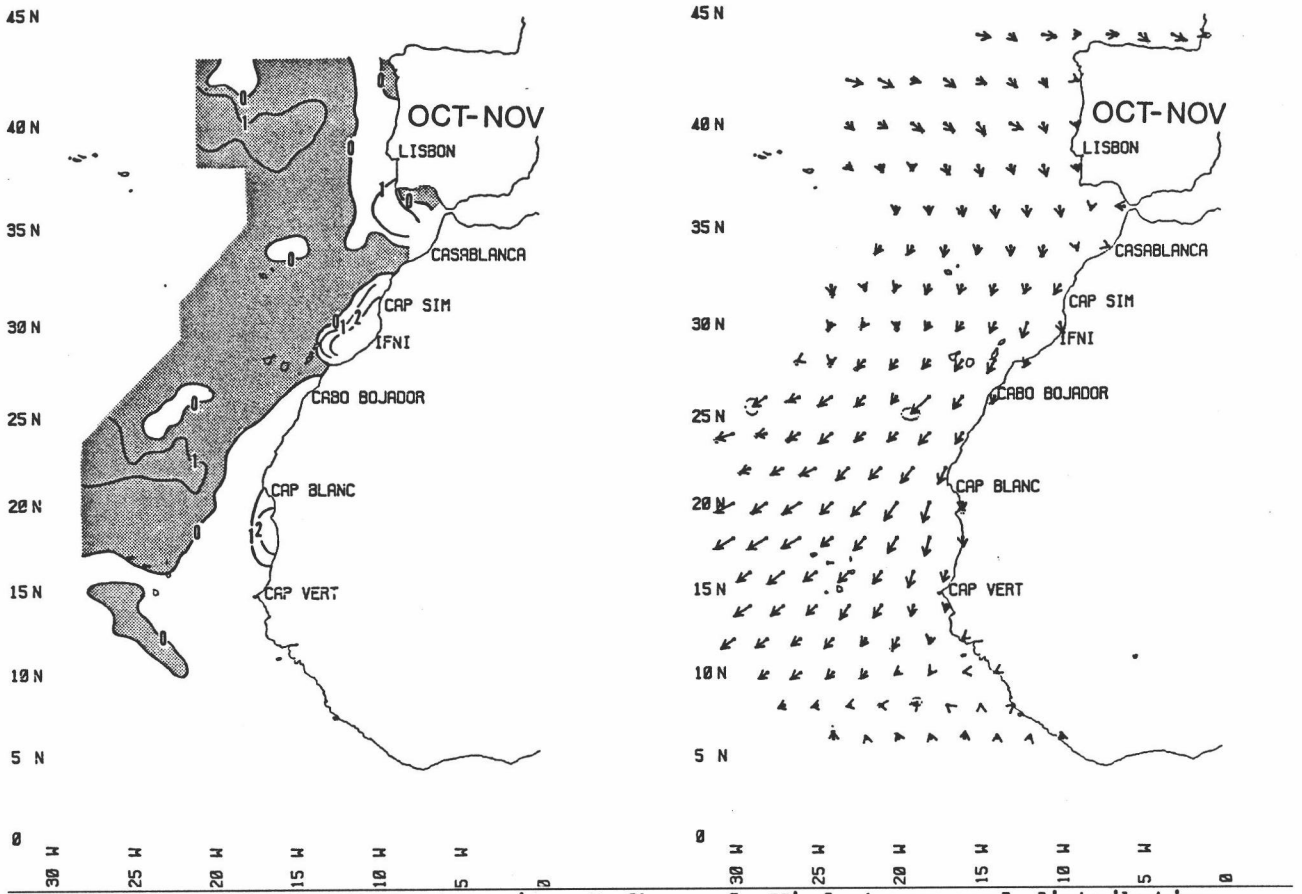

Figure II.5a. Canary Current region. *Left panel:* Wind stress curl distribution during October-November. Units are dyne cm^{-2} per 1000 km; regions of anticyclonic wind stress curl are shaded and regions of cyclonic wind stress curl are unshaded. *Right panel:* Sea surface wind stress vectors (shown only at alternate grid intersections); symbol length scale shown at lower left of panel; dotted ellipses at head of vector symbols indicate computed standard errors of the vector components.

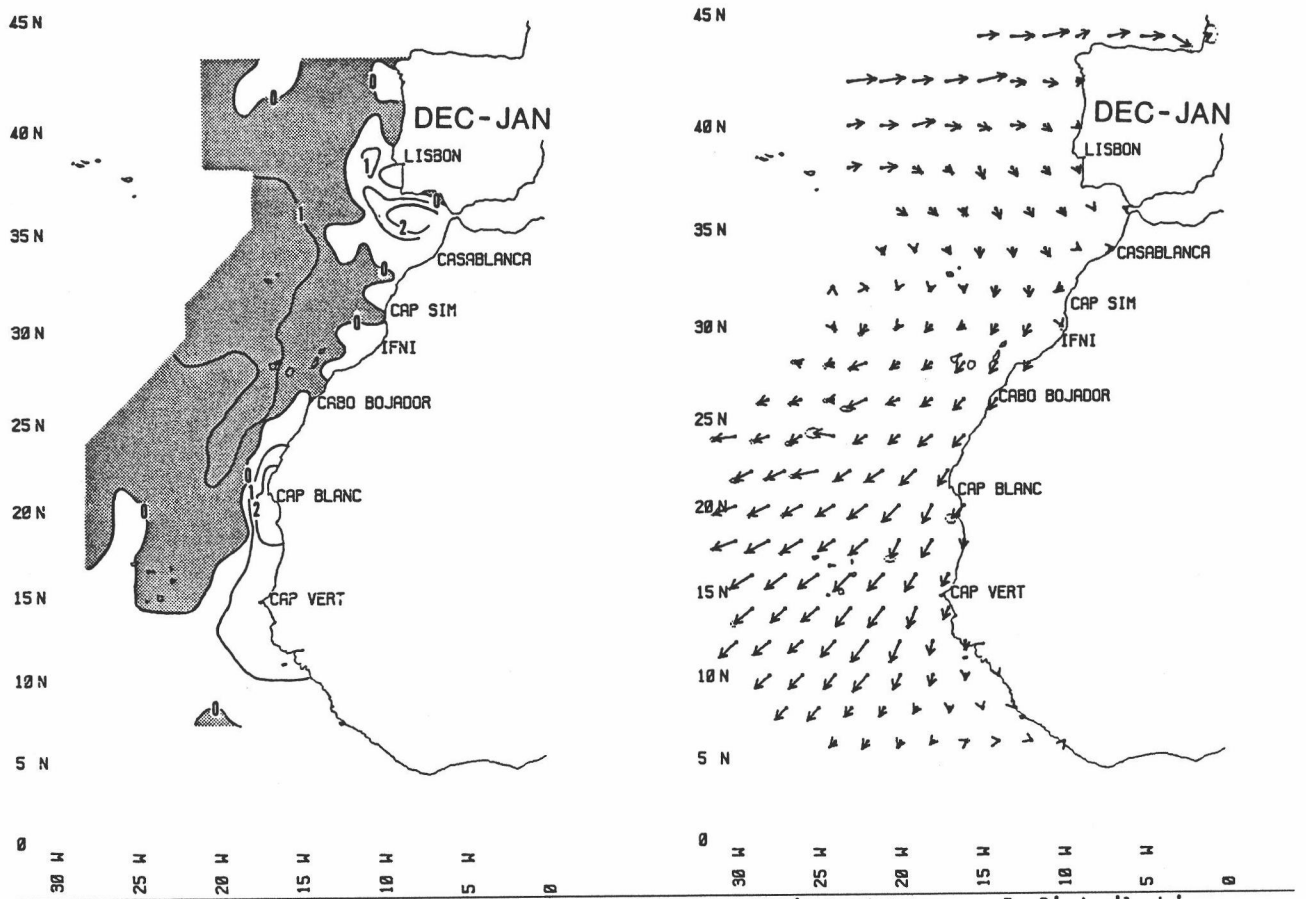

Figure II.5b. Canary Current region. *Left panel:* Wind stress curl distribution during December-January. Units are dyne cm^{-2} per 1000 km; regions of anticyclonic wind stress curl are shaded and regions of cyclonic wind stress curl are unshaded. *Right panel:* Sea surface wind stress vectors (shown only at alternate grid intersections); symbol length scale shown at lower left of panel; dotted ellipses at head of vector symbols indicate computed standard errors of the vector components.

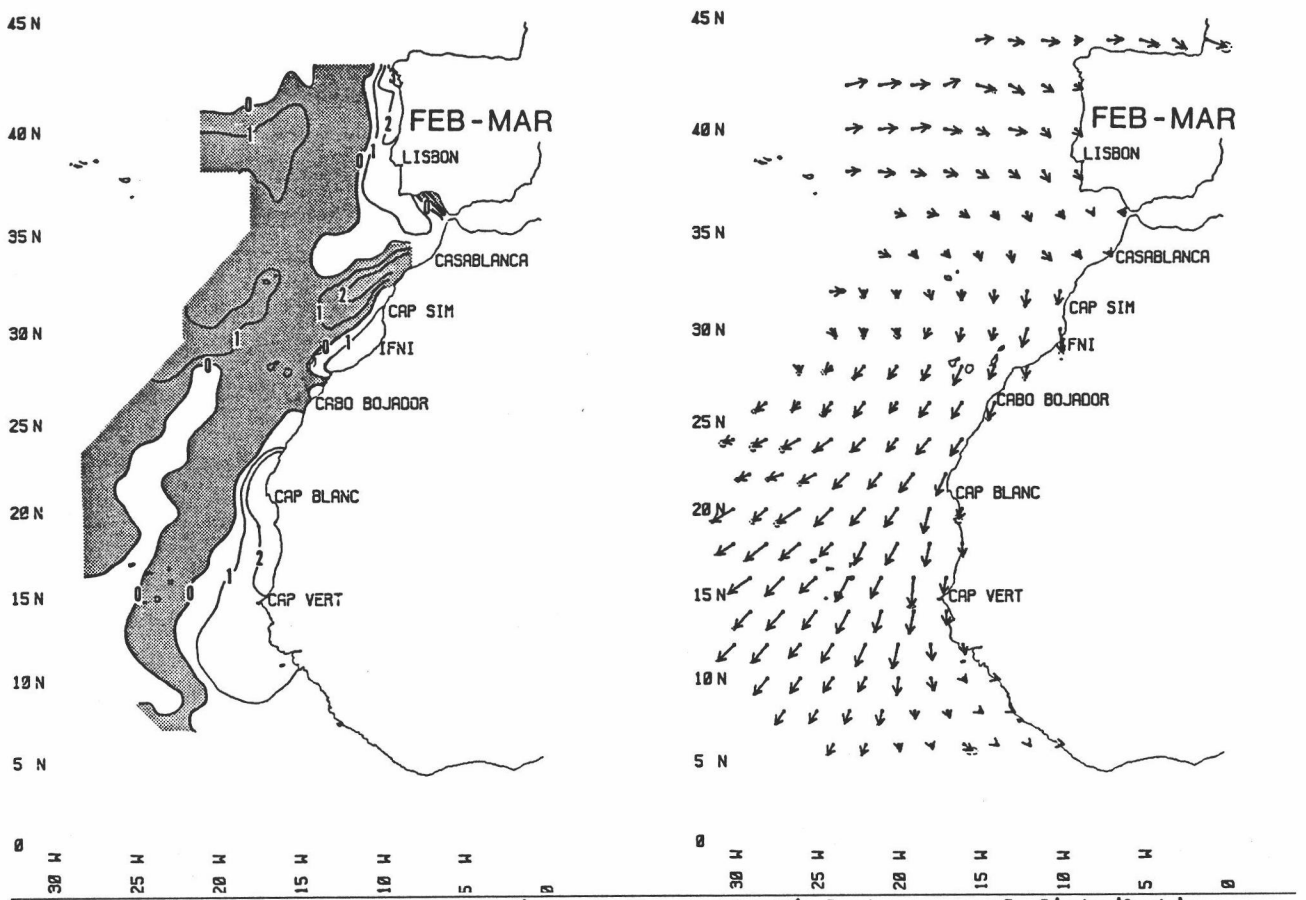

Figure II.5c. Canary Current region. *Left panel:* Wind stress curl distribution during February-March. Units are dyne cm^{-2} per 1000 km; regions of anticyclonic wind stress curl are shaded and regions of cyclonic wind stress curl are unshaded. *Right panel:* Sea surface wind stress vectors (shown only at alternate grid intersections); symbol length scale shown at lower left of panel; dotted ellipses at head of vector symbols indicate computed standard errors of the vector components.

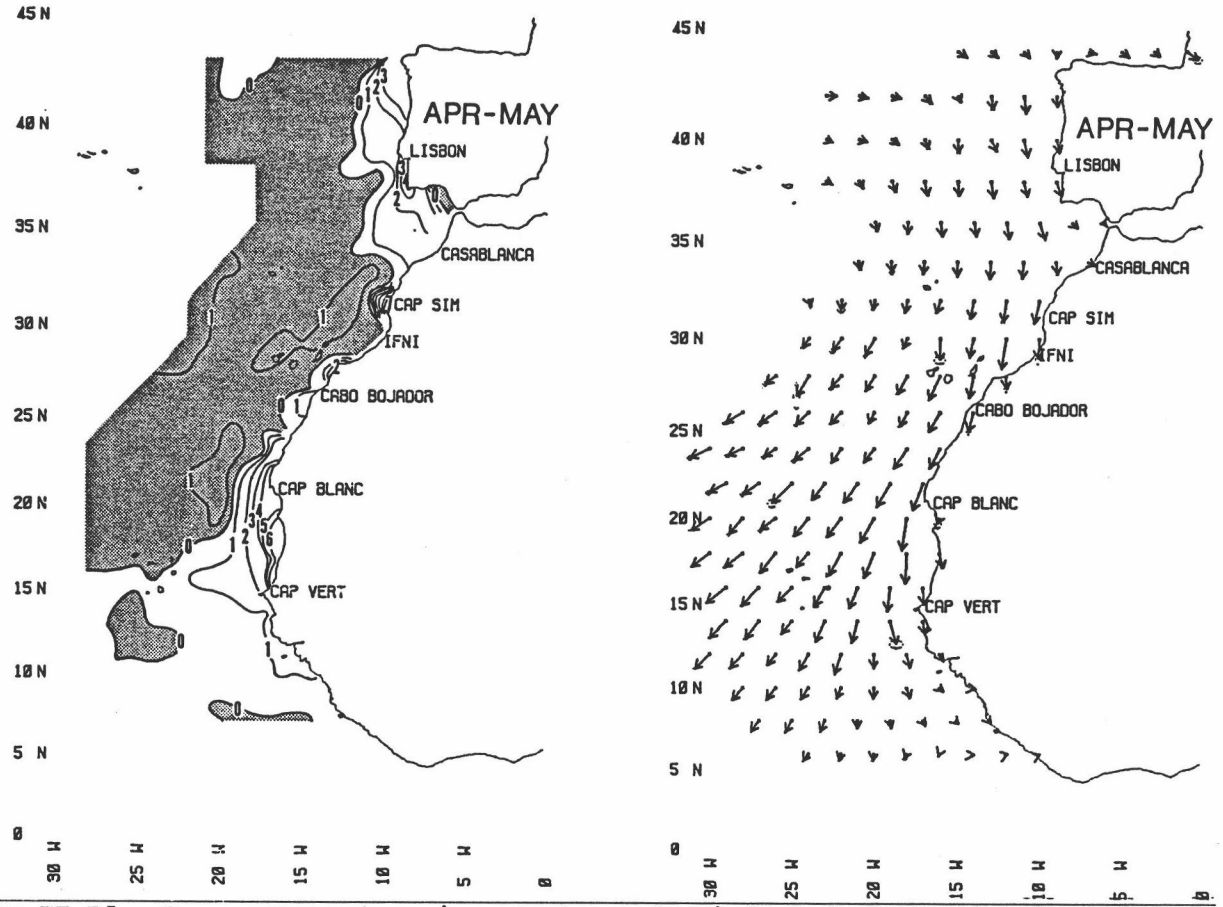

Figure II.5d. Canary Current region. *Left panel:* Wind stress curl distribution during April-May. Units are dyne cm^{-2} per 1000 km; regions of anticyclonic wind stress curl are shaded and regions of cyclonic wind stress curl are unshaded. *Right panel:* Sea surface wind stress vectors (shown only at alternate grid intersections); symbol length scale shown at lower left of panel; dotted ellipses at head of vector symbols indicate computed standard errors of the vector components.

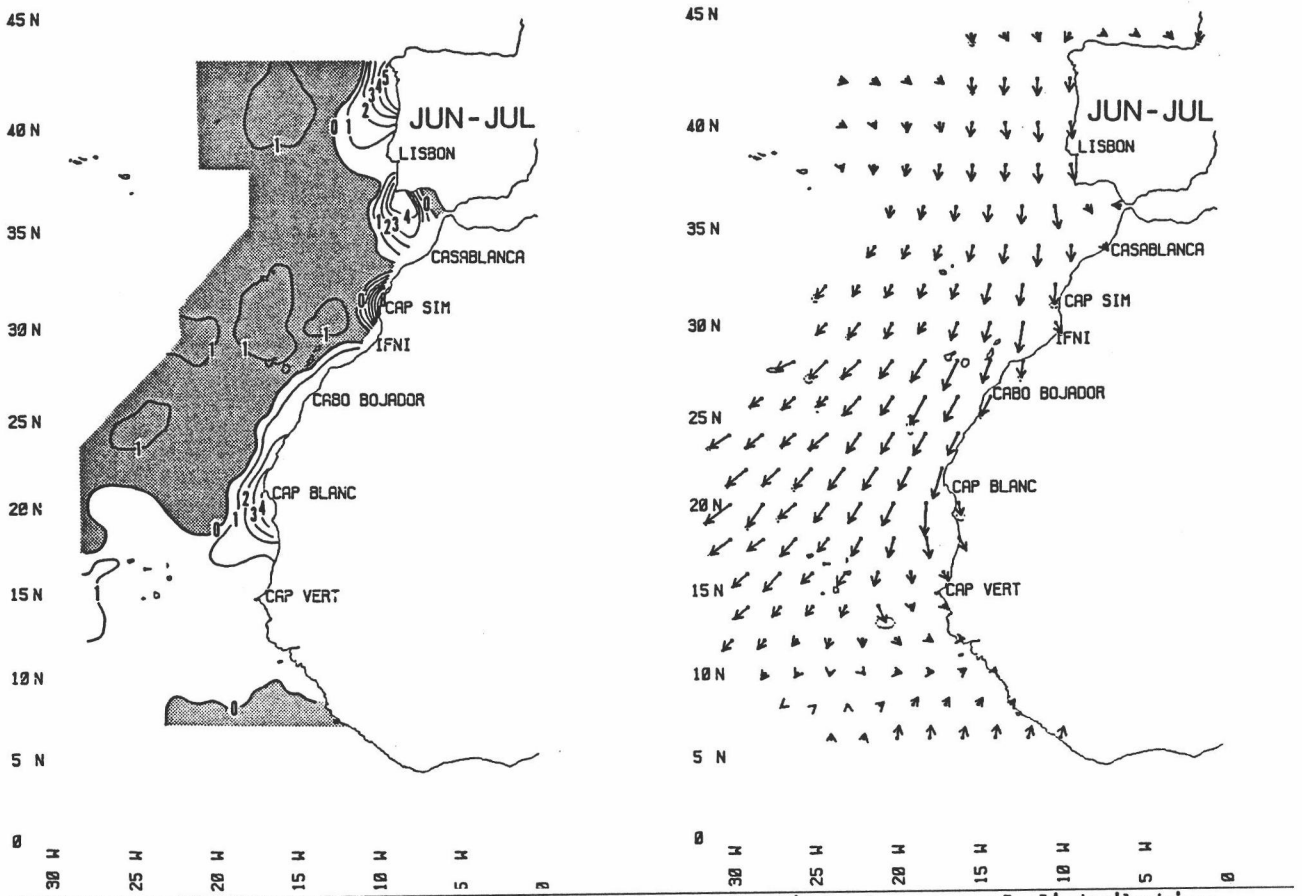

Figure II.5e. Canary Current region. *Left panel:* Wind stress curl distribution during June-July. Units are dyne cm^{-2} per 1000 km; regions of anticyclonic wind stress curl are shaded and regions of cyclonic wind stress curl are unshaded. *Right panel:* Sea surface wind stress vectors (shown only at alternate grid intersections); symbol length scale shown at lower left of panel; dotted ellipses at head of vector symbols indicate computed standard errors of the vector components.

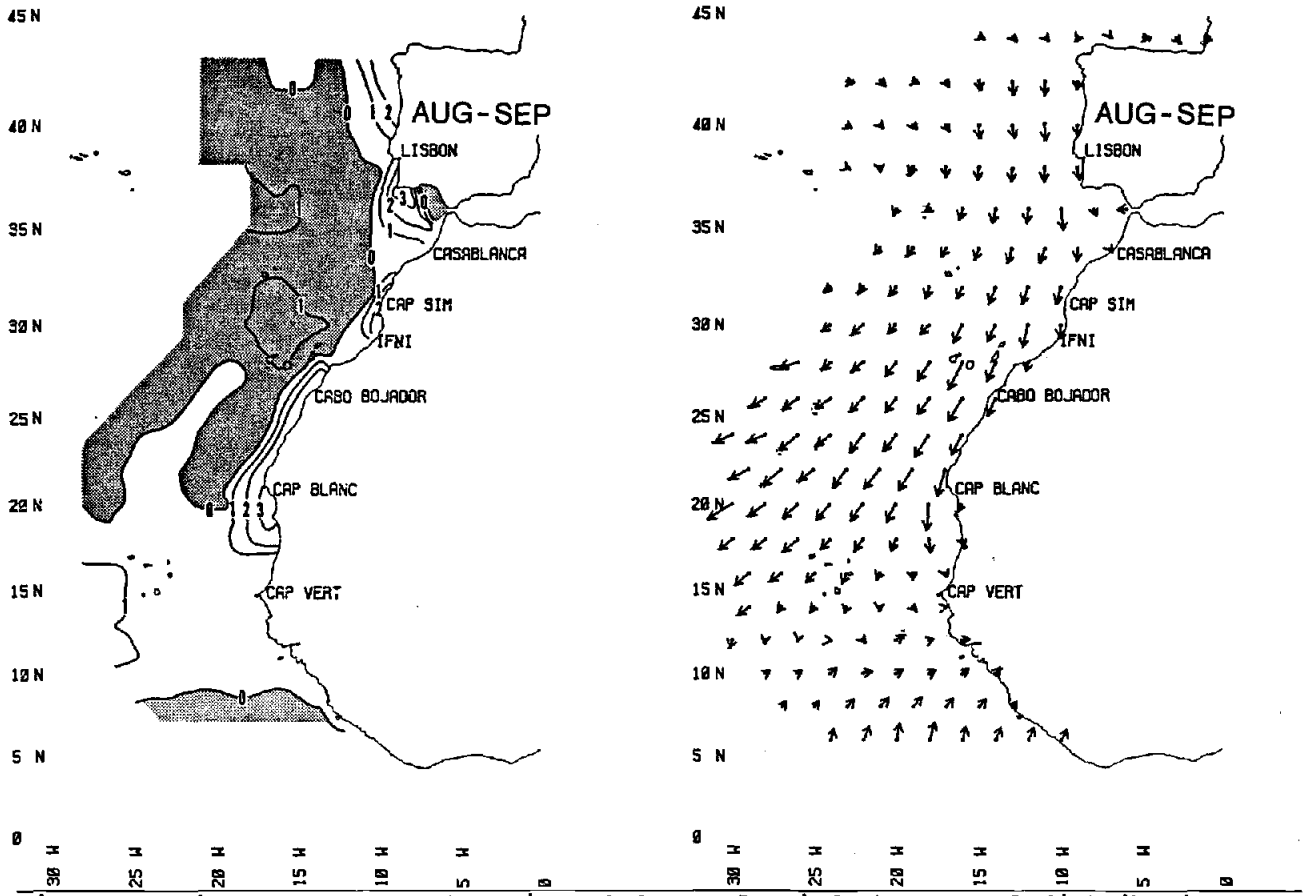

Figure II.5f. Canary Current region. *Left panel:* Wind stress curl distribution during August-Seeptember. Units are dyne cm^{-2} per 1000 km; regions of anticyclonic wind stress curl are shaded and regions of cyclonic wind stress curl are unshaded. *Right panel:* Sea surface wind stress vectors (shown only at alternate grid intersections); symbol length scale shown at lower left of panel; dotted ellipses at head of vector symbols indicate computed standard errors of the vector components.

(Wooster, et al., 1976). Near the coast of the Iberian Peninsula, the mean curl distribution is rather weak and irregular during fall and early winter, but becomes strongly cyclonic during the spring and summer, when spatially separated wind stress curl maxima appear adjacent to the northwestern coast of the Penninsula and off southern Portugal.

A lobe of anticyclonic wind stress curl extends to the coast near Cabo Bojador during fall and winter (Figs. II.5a, II.5b, II.5c). This lobe is at a fairly similar latitude to that of the persistent Punta Baja lobe in the California Current region. However, the lobe off Cabo Bojador and a similar lobe north of Cap Sim do not exhibit the same degree of persistence through the spring and summer upwelling season. In fact the areas off Cap Sim and Cabo Bojador tend to be sites of strong cyclonic curl in the spring through late summer (Figs. II.5d, II.5e, II.5f). Moreover, a lobe of anticyclonic wind stress curl, rather than being associated with any coastal protuberence, appears to extend directly into into the coastal bight near Ifni during late spring and early summer.

An interesting tendency for the offshore anticyclonic curl area to be split by a region of cyclonic (or very weak anticyclonic) curl in the region some 5 to 10 degrees offshore, from Cabo Bojador to somewhat south of Cap Blanc, appears in most of the Canary Current distributions.

The area from about 10° N lat to 20°N lat is characterized by cyclonic wind stress curl during the summer months (Figs. II.5e and II.5f). However at the other seasons of the year a region of anticyclonic curl extends to the south of Cap Vert between 21° and 25° W long.

II.6 The Benguela Current Region

In the Benguela region, the coastal cyclonic wind stress curl region appears as a wedge extending from the vicinity of 20°S lat, narrowing in offshore extent toward the south. The wedge has its most limited poleward extent in austral winter (Fig. II.6b) when it reaches to just south of Luderitz. By early spring the wedge has extended to Cape Columbine (Fig. II.5c) and beyond the Cape of Good Hope by late spring (Fig. II.5d) where it remains until it retreats northward again with the approach of austral winter.

North of 20° S lat, the distributions are less distinct. A sparcity of observations in that region (Fig. II.3), and associated large sampling errors, make the computed curl distributions very noisy and somewhat uncertain. However, one very persistent feature is an area of cyclonic curl, some hundreds of km in diameter lying about 200 km off, and extending somewhat northward of, Cape Frio. Evidence of this particular feature is found in all twelve of the independent monthly distributions.

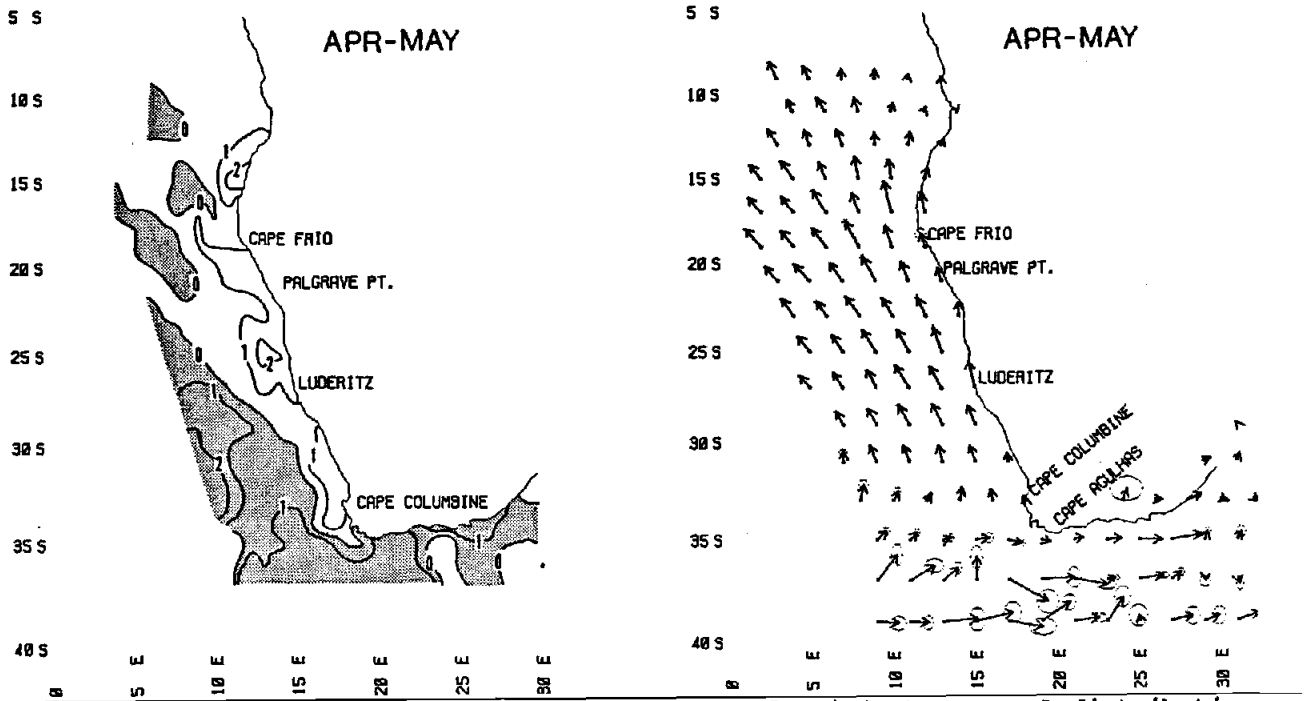

Figure II.6a. Benguela Current region. *Left panel:* Wind stress curl distribution during April-May. Units are dyne cm^{-2} per 1000 km; regions of anticyclonic wind stress curl are shaded and regions of cyclonic wind stress curl are unshaded. *Right panel:* Sea surface wind stress vectors (shown only at alternate grid intersections); symbol length scale shown at lower left of panel; dotted ellipses at head of vector symbols indicate computed standard errors of the vector components.

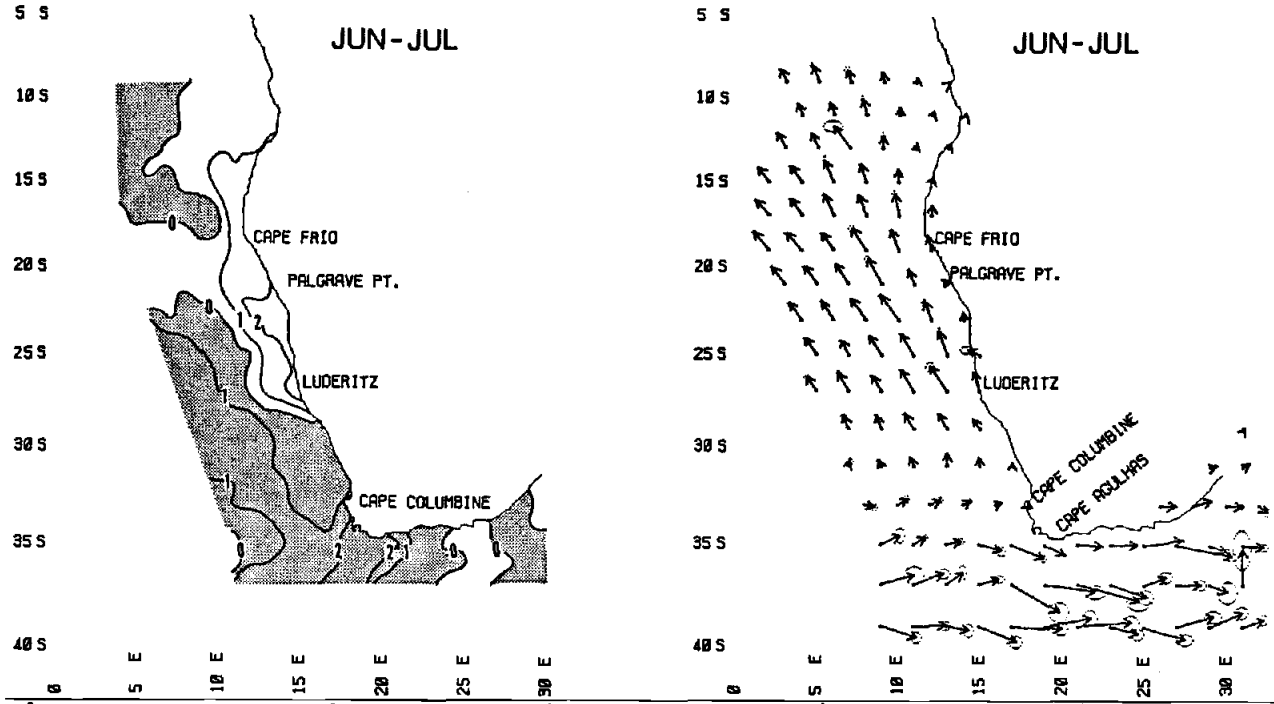

Figure II.6b. Benguela Current region. *Left panel:* Wind stress curl distribution during June-July. Units are dyne cm^{-2} per 1000 km; regions of anticyclonic wind stress curl are shaded and regions of cyclonic wind stress curl are unshaded. *Right panel:* Sea surface wind stress vectors (shown only at alternate grid intersections); symbol length scale shown at lower left of panel; dotted ellipses at head of vector symbols indicate computed standard errors of the vector components.

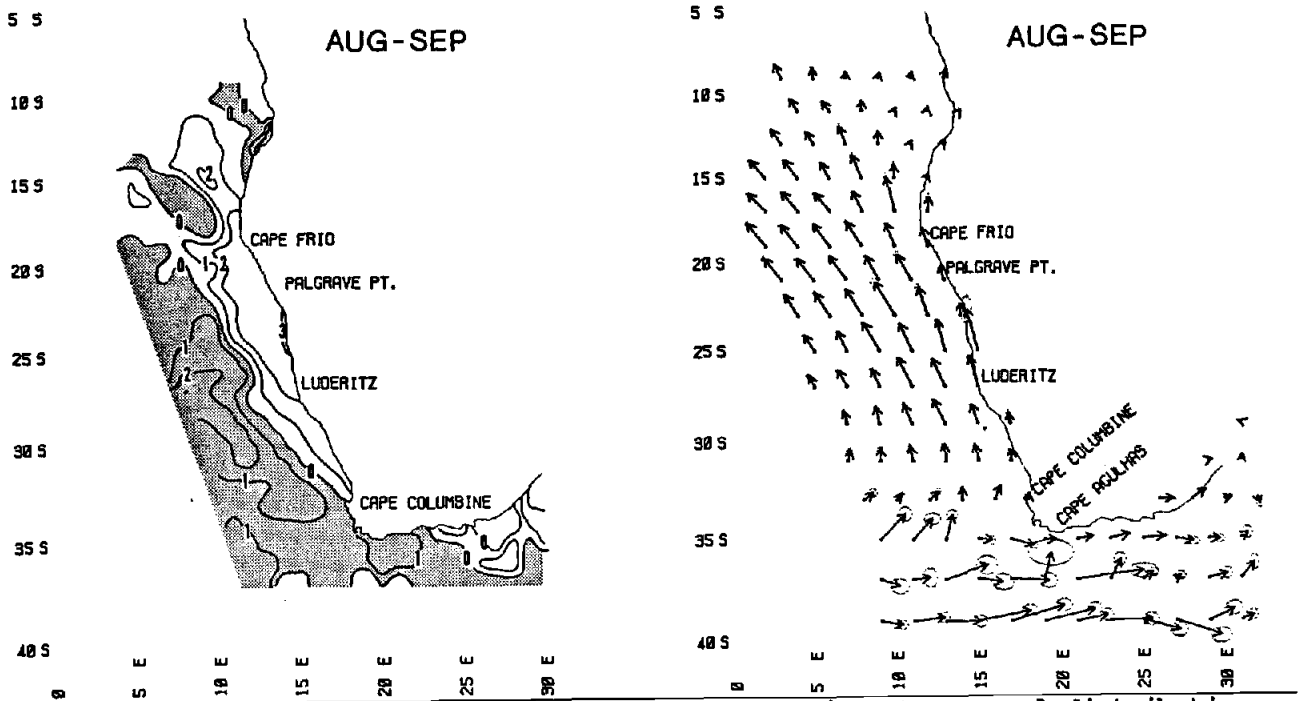

Figure II.6c. Benguela Current region. *Left panel:* Wind stress curl distribution during August-Seeptember. Units are dyne cm^{-2} per 1000 km; regions of anticyclonic wind stress curl are shaded and regions of cyclonic wind stress curl are unshaded. *Right panel:* Sea surface wind stress vectors (shown only at alternate grid intersections); symbol length scale shown at lower left of panel; dotted ellipses at head of vector symbols indicate computed standard errors of the vector components.

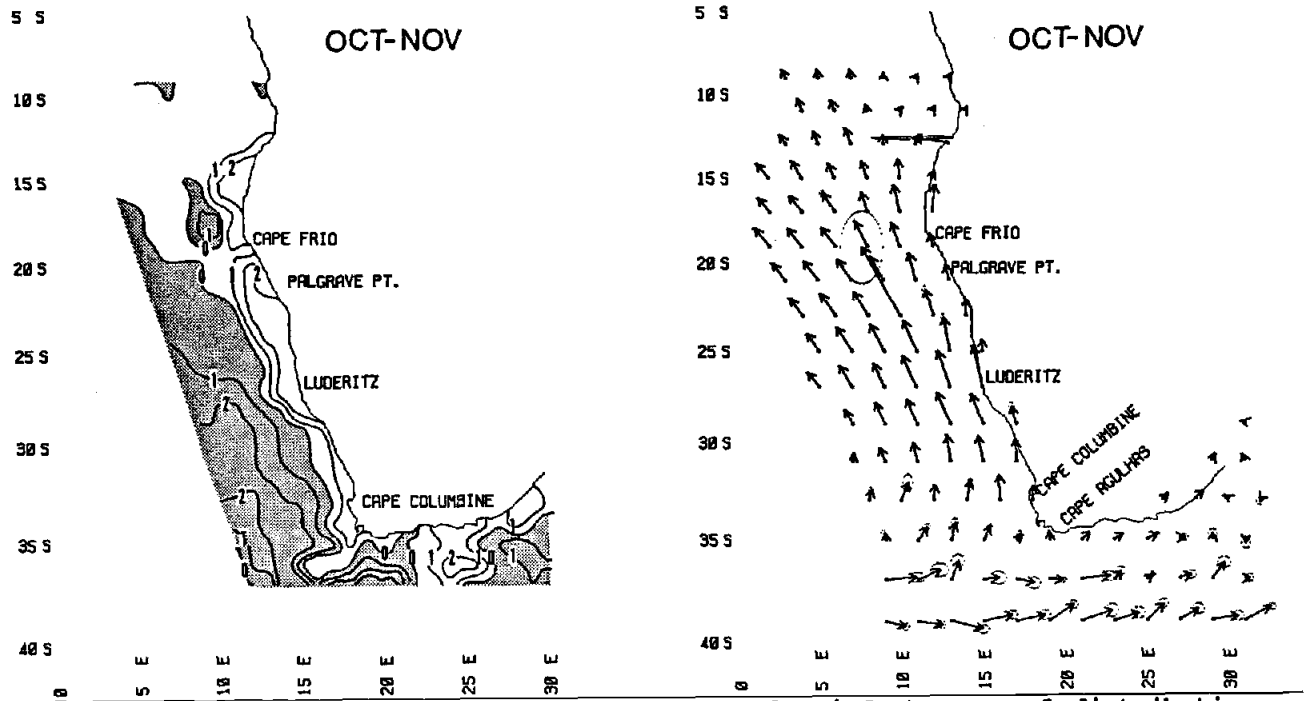

Figure II.6d. Benguela Current region. *Left panel:* Wind stress curl distribution during October-November. Units are dyne cm^{-2} per 1000 km; regions of anticyclonic wind stress curl are shaded and regions of cyclonic wind stress curl are unshaded. *Right panel:* Sea surface wind stress vectors (shown only at alternate grid intersections); symbol length scale shown at lower left of panel; dotted ellipses at head of vector symbols indicate computed standard errors of the vector components.

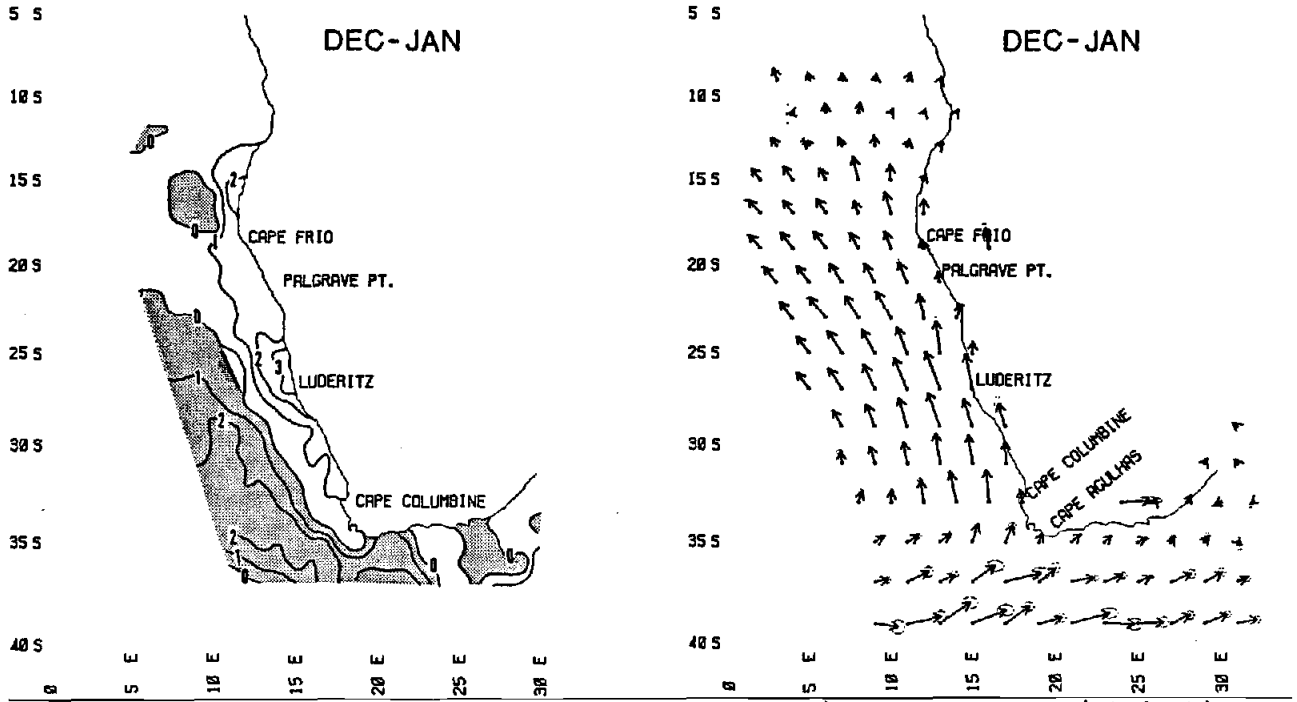

Figure II.6e. Benguela Current region. *Left panel:* Wind stress curl distribution during December-January. Units are dyne cm^{-2} per 1000 km; regions of anticyclonic wind stress curl are shaded and regions of cyclonic wind stress curl are unshaded. *Right panel:* Sea surface wind stress vectors (shown only at alternate grid intersections); symbol length scale shown at lower left of panel; dotted ellipses at head of vector symbols indicate computed standard errors of the vector components.

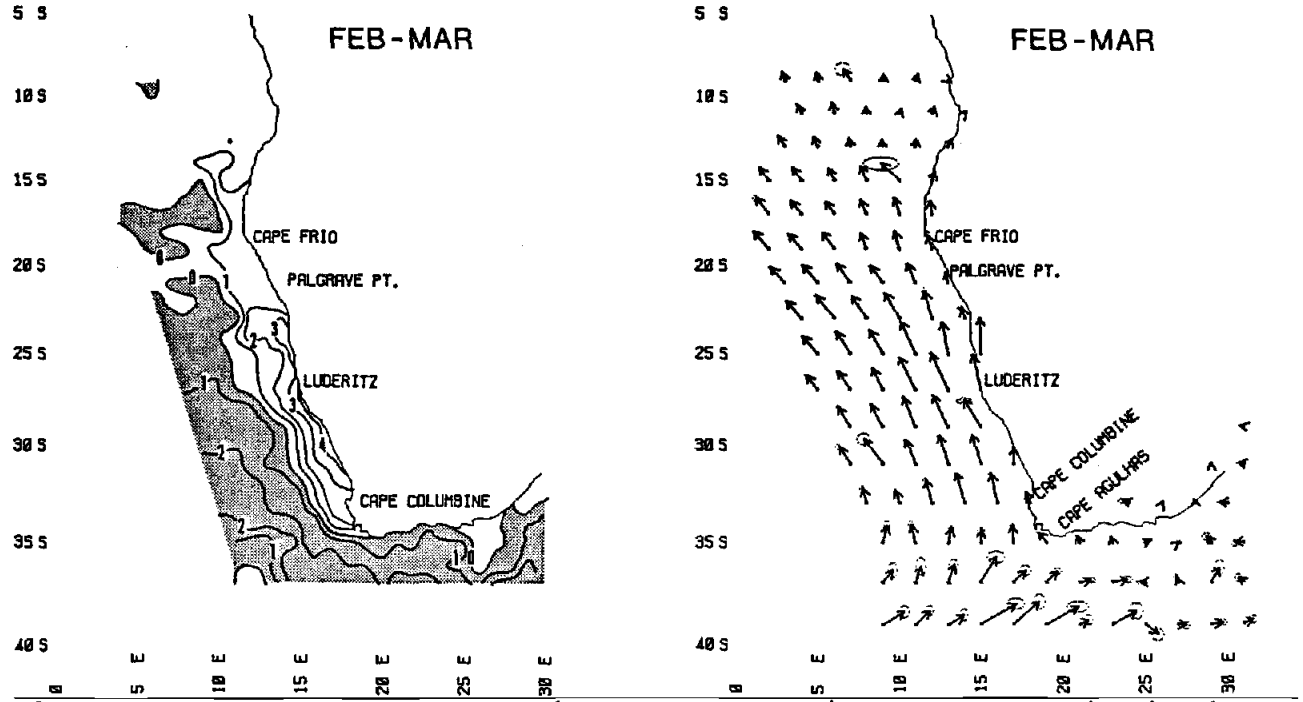

Figure II.6f. Benguela Current region. *Left panel:* Wind stress curl distribution during February-March. Units are dyne cm^{-2} per 1000 km; regions of anticyclonic wind stress curl are shaded and regions of cyclonic wind stress curl are unshaded. *Right panel:* Sea surface wind stress vectors (shown only at alternate grid intersections); symbol length scale shown at lower left of panel; dotted ellipses at head of vector symbols indicate computed standard errors of the vector components.

In the region north of 15° S lat, there appears to be some tendency for anticyclonic curl near the coast in late austral winter to spring; in austral summer and fall the region within 700 km of the coast appears to be dominated by cyclonic wind stress curl.

II.7 The Peru/Humboldt Current Region

The region off western South America has an order of magnitude lower density of available maritime data than the other three regions (Fig. II.3). When the data are restricted to the same 30-year period, 1950-79, there are very large areas where there are less than 10 observations per one-degree square per composite two-month sample. Wind stress curl fields computed from these severely undersampled stress fields are chaotic. It was deemed necessary, in this case, to violate the rigorous application of the staggered grid system as described in Sections II.2 and II.3. Accordingly, a second set of maps, incorporating all the available data in the historical record (1850-1979), was produced. Positions reported only to whole degrees of latitude and longitude are treated as if they were actually accurately positioned at the integral one-degree intersections. The resulting less accurate determination of the magnitudes of the derivatives in Eq. 2.2 is considered preferable to arbitrarily drawing contours through large data gaps over much of the region.

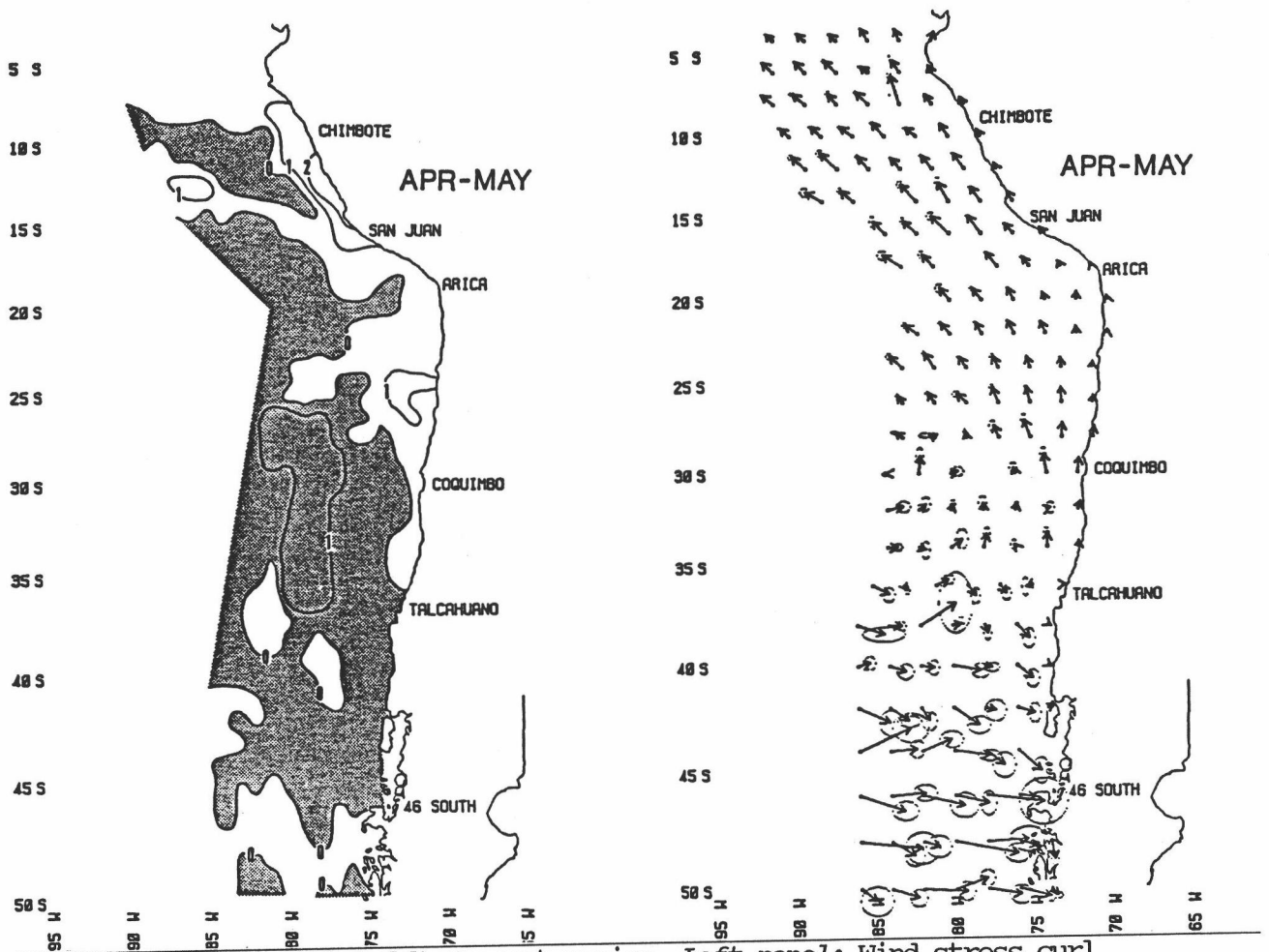

Figure II.7a. Peru/Humboldt Current region. *Left panel:* Wind stress curl distribution during April-May. Units are dyne cm^{-2} per 1000 km; regions of anticyclonic wind stress curl are shaded and regions of cyclonic wind stress curl are unshaded. *Right panel:* Wind stress vectors (shown only at alternate grid intersections); symbol length scale shown at lower left of panel; dotted ellipses at head of vector symbols indicate computed standard errors of the vector components.

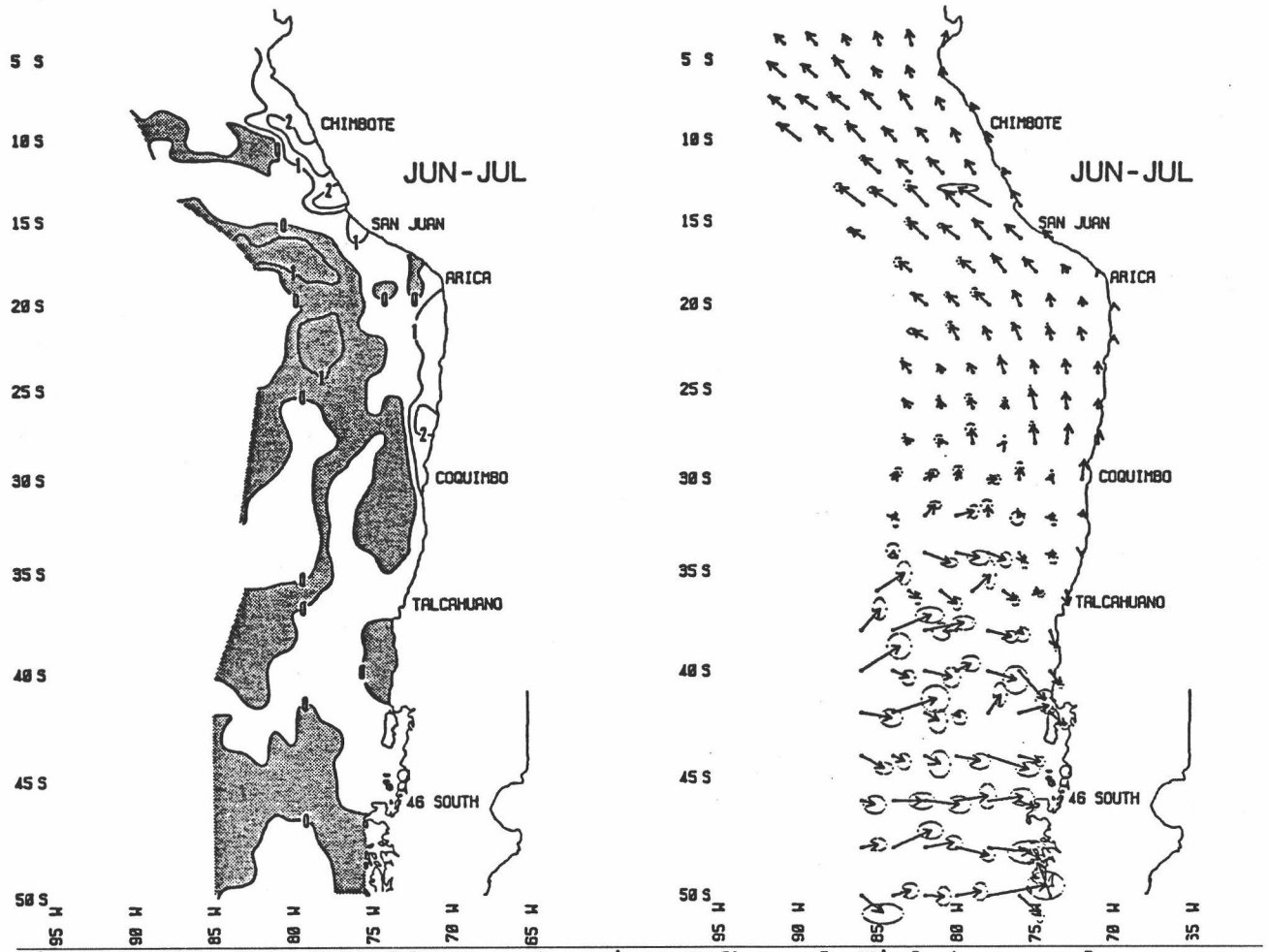

Figure II.7b. Peru/Humboldt Current region. *Left panel:* Wind stress curl distribution during June-July. Units are dyne cm^{-2} per 1000 km; regions of anticyclonic wind stress curl are shaded and regions of cyclonic wind stress curl are unshaded. *Right panel:* Wind stress vectors (shown only at alternate grid intersections); symbol length scale shown at lower left of panel; dotted ellipses at head of vector symbols indicate computed standard errors of the vector components.

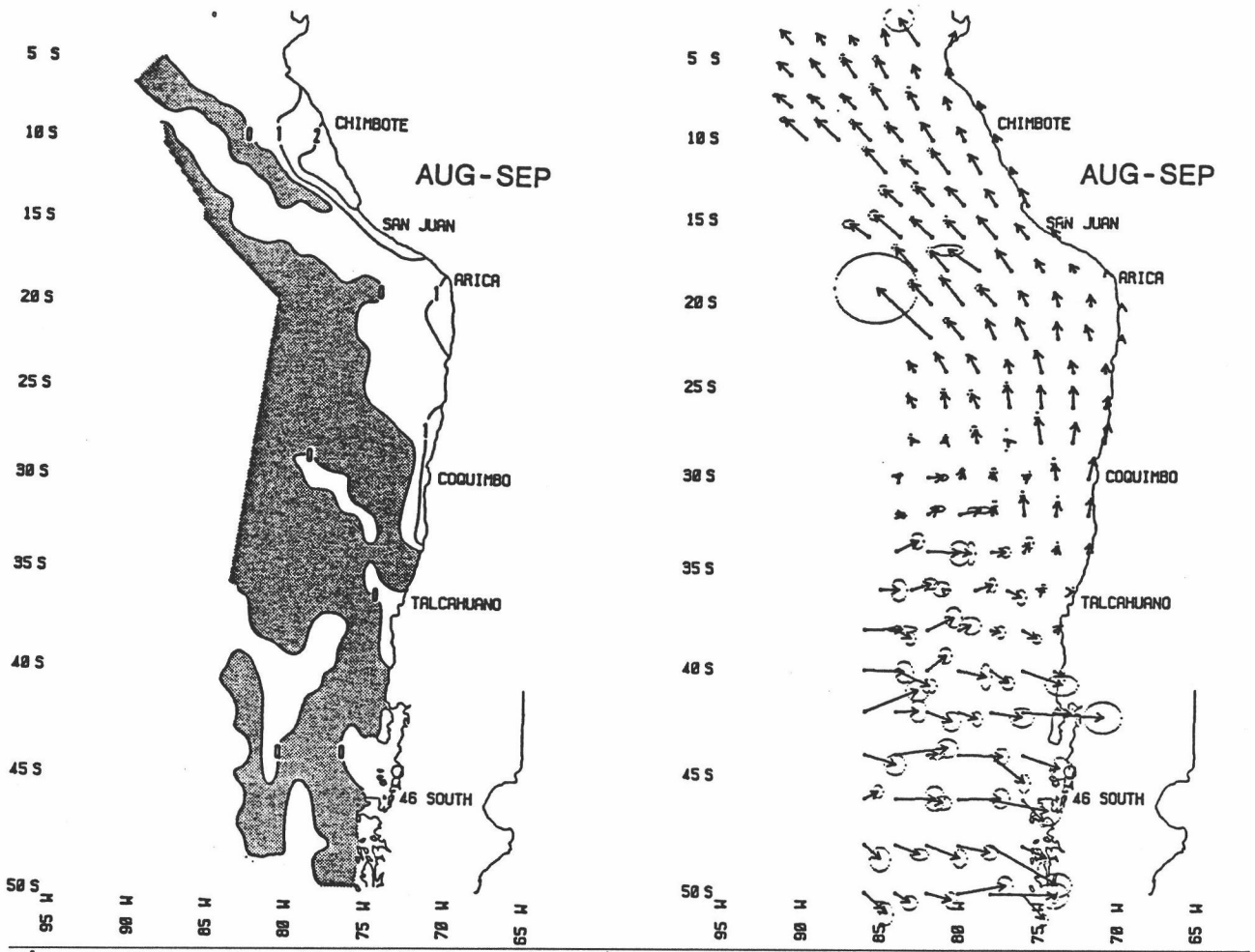

Figure II.7c. Peru/Humboldt Current region. *Left panel:* Wind stress curl distribution during August-Seeptember. Units are dyne cm^{-2} per 1000 km; regions of anticyclonic wind stress curl are shaded and regions of cyclonic wind stress curl are unshaded. *Right panel:* Wind stress vectors (shown only at alternate grid intersections); symbol length scale shown at lower left of panel; dotted ellipses at head of vector symbols indicate computed standard errors of the vector components.

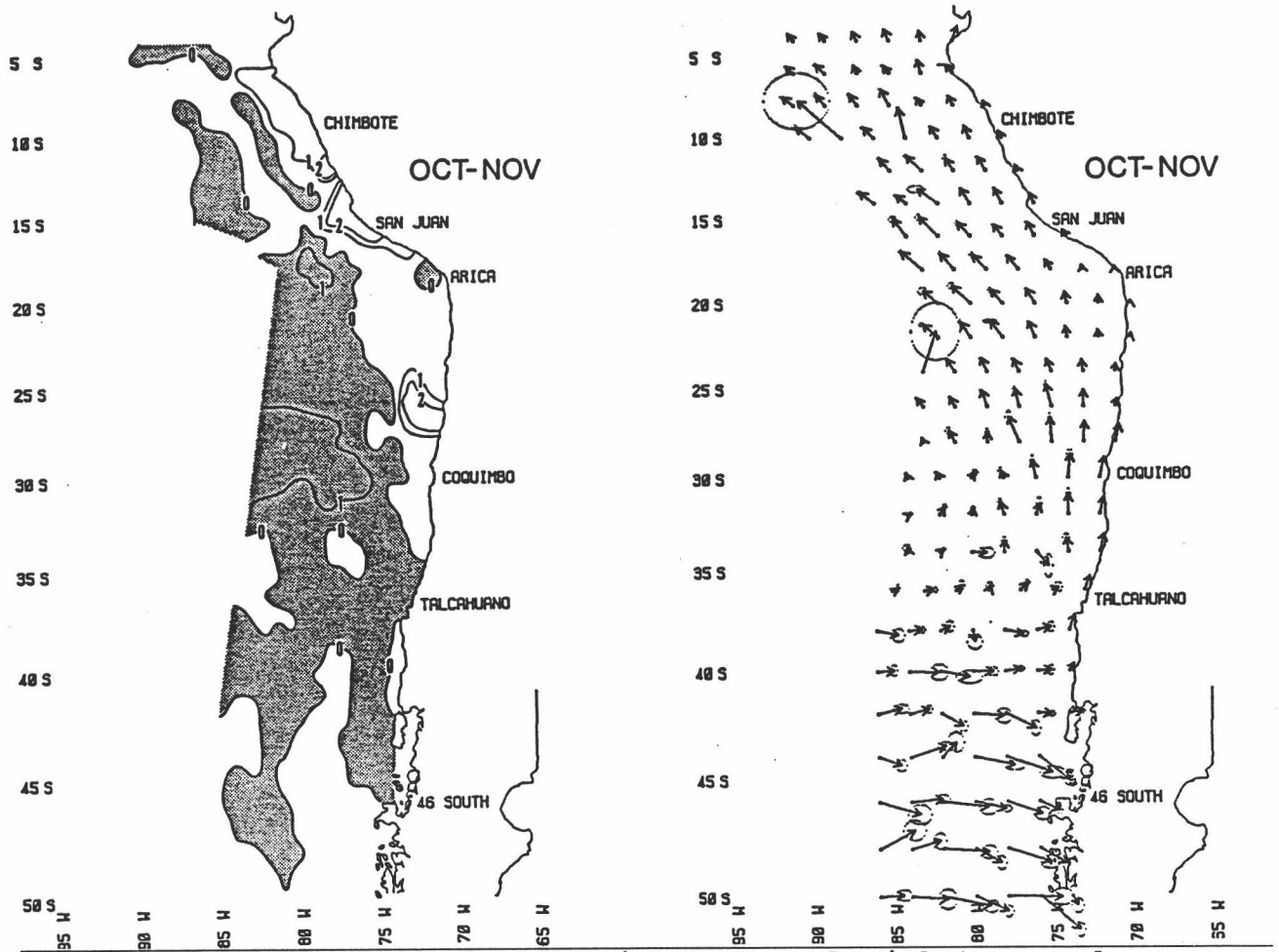

Figure II.7d. Peru/Humboldt Current region. *Left panel:* Wind stress curl distribution during October-November. Units are dyne cm^{-2} per 1000 km; regions of anticyclonic wind stress curl are shaded and regions of cyclonic wind stress curl are unshaded. *Right panel:* Wind stress vectors (shown only at alternate grid intersections); symbol length scale shown at lower left of panel; dotted ellipses at head of vector symbols indicate computed standard errors of the vector components.

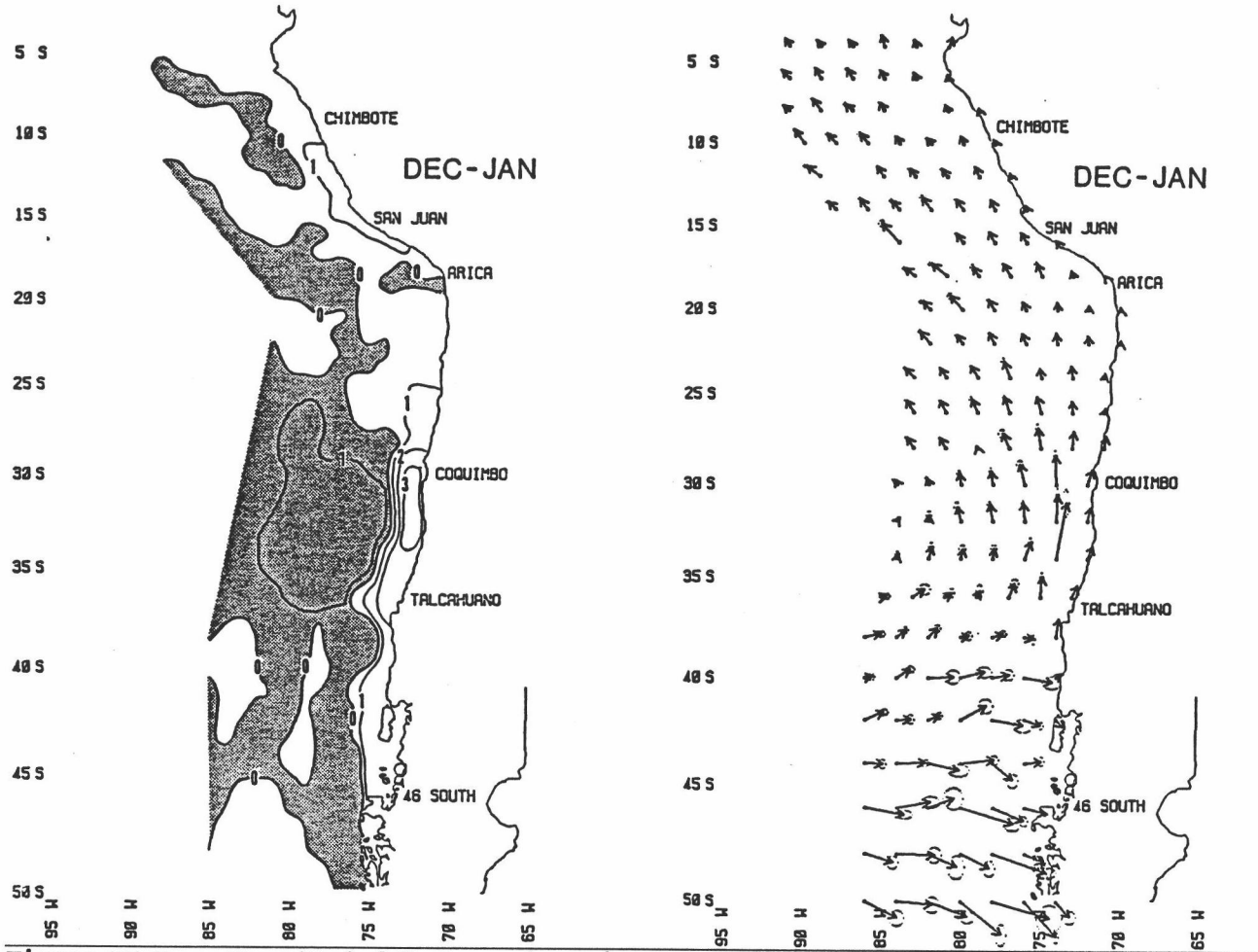

Figure II.7e. Peru/Humboldt Current region. *Left panel:* Wind stress curl distribution during December-January. Units are dyne cm^{-2} per 1000 km; regions of anticyclonic wind stress curl are shaded and regions of cyclonic wind stress curl are unshaded. *Right panel:* Wind stress vectors (shown only at alternate grid intersections); symbol length scale shown at lower left of panel; dotted ellipses at head of vector symbols indicate computed standard errors of the vector components.

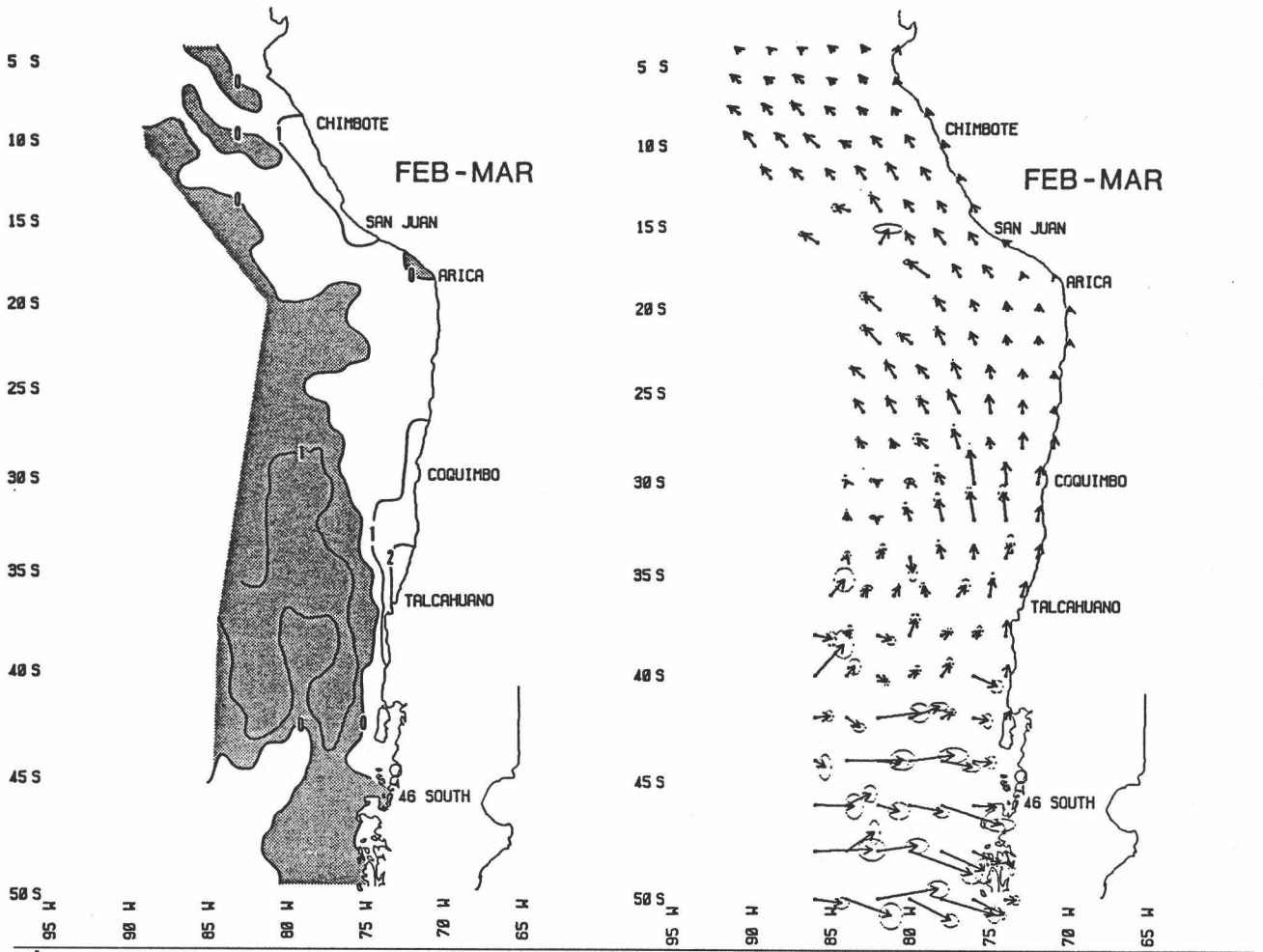

Figure II.7f. Peru/Humboldt Current region. *Left panel:* Wind stress curl distribution during February-March. Units are dyne cm^{-2} per 1000 km; regions of anticyclonic wind stress curl are shaded and regions of cyclonic wind stress curl are unshaded. *Right panel:* Wind stress vectors (shown only at alternate grid intersections); symbol length scale shown at lower left of panel; dotted ellipses at head of vector symbols indicate computed standard errors of the vector components.

Thus the two-month climatological distributions of wind stress curl for the Peru/Humboldt Current region (Fig. II.7) were produced by applying the procedures described in Sections II.2 and II.3 for two different data bases. For the bulk of the region, the total historical data base is incorporated, thereby degrading the precision of the computations. However, where sufficient data is available (e.g., in the extreme northern part of the grid area) the contours are drawn to conform to computations from the 1950-79 data base.

During the austral fall season (Fig. II.7a), cyclonic curl adjacent to the coast extends south to the vicinity of Talcahuano; local maxima appear along the coast of Peru from the vicinity of San Juan to north of Chimbote, and off Chile at about 25° S lat. The maximum off Peru appears to maintain its location throughout the year, strengthening in austral winter and relaxing somewhat in summer. The wind stress curl maximum off Chile moves southward from winter to summer, reaching maximum intensity off the stretch of coastline from 30° to 34° S lat, in austral summer (Fig. II.7e); it appears to move even further south in late summer (Fig. II.7f) to a position just north of Talcahuano, before weakening greatly and retreating back northward in fall.

There are consistent indications of influence of anticyclonic curl within the coastal bight near Arica. This

is in contrast to the consistent cyclonic curl found to characterize major coastal bights in other eastern boundary current regions, e.g., in the Southern California Bight (Fig. II.4) and between Cap Blanc and Cap Vert (Fig. II.5). This is probably due to the fact that the coastal shape here is such that the equatorward wind, which flows along the Chilean coast, blows uninterruptedly into the bight, rather than being deflected by a major change in coastline trend at the upwind edge of the bight.

A persistent elongate lobe of anticyclonic curl, definitely separated from the general anticyclonic curl in the offshore region to the south, exists off northern Peru. In view of the low data density available for the region, its consistency in location and general shape among these independently-prepared distributions is remarkable. It appears to be aligned along the axis of the tradewind flow which veers westward, away from the coast, in that area.

II.8 Generalizations

Eastern boundary current regions appear to be characterized by anticyclonic wind stress curl in their offshore portions. Nearer the coastal boundary, the wind stress curl tends to be cyclonic, particularly during the coastal upwelling seasons (i.e., seasons in which substantial wind stress is directed alongshore and equatorward). These cyclonic curl areas typically extend 200 to 500 km

offshore. Thus the coastal upwelling which occurs within several tens of km from the coast is typically augmented by upward Ekman pumping (oceanic upwelling) over a much larger offshore extent. Accordingly, there tends to be a transition zone several hundreds of km off the coast where the surface Ekman transport changes from divergent to convergent. This zone is a likely area for frontal formations, where organisms associated with the upwelling-enriched areas nearer the coast may be concentrated to yield efficient feeding grounds for large predatory fishes such as tunas (Parrish, et al., 1981). Cyclonic wind stress curl adjacent to the coast has been cited as an explanation for poleward coastal countercurrents and undercurrents in eastern boundary current regions via a depth-integrated Sverdrup transport argument (e.g., Munk, 1950).

The coastal cyclonic curl regions tend to have their greatest alongshore extents during the summer seasons in the respective hemispheres. Particularly intense curl is found adjacent to capes during summer coastal upwelling maxima. During the season of relaxed upwelling the most intense cyclonic curl is associated with coastal bights.

These characteristics suggest that during seasons of strong equatorward alongshore wind stress, the offshore profile of stress least a qualitative resemblance to a lateral frictional boundary layer, characterized by an offshore wind velocity maximum and decay of velocity toward

the coast. In that case, coastal protuberences would tend to narrow the layer locally, leading to intensified cyclonic curl. On the other hand, during winter seasons, the regime tends to be intermittently broken by the passage of cyclonic storms, which often involve intense winds having poleward and onshore components. Although maritime data cannot define synoptic situations on these small spatial scales, it would seem reasonable that such winds might tend to reach maximum velocities as they are narrowed, and deflected toward a more alongshore direction, directly adjacent to the barrier presented by the coastal boundary; such effects might tend to be strongest where the wind flow was directed into coastal bights, leading to the tendency during winter for cyclonic curl maxima to lie within such concave coastal segments.

In various locations, certain lobes or "blobs" of anticyclonic curl are persistently maintained either in contact with, or within several hundred km of, the coastal boundary. These appear most often to be associated with a veering offshore of the equatorward wind flow as it begins to merge into the tropical tradewind circulation.

III. THE LARGE SCALE VORTICITY BALANCE IN EASTERN BOUNDARY CURRENT SYSTEMS: A COMPARATIVE APPROACH

III.1 The comparative framework

In this chapter, we look for correspondences between the wind stress curl distributions and available information on the flow patterns in the several regions. The goal is to identify consistent patterns of correspondence, within and among regions, that may be useful in clarifying the dynamical linkages.

We should note at the outset that this case does not constitute an ideal example of application of the comparative method. Ideally, the two fields should be independent of common influence by any third factor. In the present case, both the atmosphere and the ocean are similarly subject to influences of the adjacent continental boundary. This sometimes makes it difficult to separate features which may be driven by overlying features in the wind pattern from features which are lateral boundary effects occurring similarly, and largely independently, in the oceanic and atmospheric fluid flows. However, even where multiple alternative explanations may result, these may at least help to point out some narrowed probable range of dominant linkage mechanisms and thereby provide useful conceptual framework on which to base further research

activities.

An additional problem is the paucity of available flow information. Thus, the available flow patterns, even when constituting averages of data taken from different years, may not directly match the averaging period implicit in our long-term average wind stress curl distributions. Also, the formulation of mean surface geostrophic flow patterns is customarily based on scalar-averaging of dynamic height data, rather than vector-averaging of velocity data; the result is that areal biases in distributions of data from specific cool or warm groups of years can result in artificial dynamic height gradients which delineate flow features which may never have existed in any actual synoptic situation. In addition, lacking time series of wind stress curl estimates, we cannot be confident that any particular synoptic dynamic height pattern may not represent responses to quite different wind stress curl patterns from the long term composite fields which we are using for comparison. We will need to keep these limitations in mind in "tempering" our interpretations.

As a framework for the comparisons, we form the vorticity equation for geophysical fluid flow. The time-averaged Navier-Stokes equations for large scale horizontal ocean flow, using eddy coefficient parameterizations for the lateral Renolds stresses, are:

$$\frac{\partial u}{\partial t} + \vec{v}\cdot\nabla u - fv = -\frac{1}{\rho}\frac{\partial p}{\partial x} + A_H\left(\frac{\partial^2 u}{\partial x^2} + \frac{\partial^2 u}{\partial y^2}\right) + \frac{1}{\rho}\frac{\partial \tau_x}{\partial z}$$

$$\frac{\partial v}{\partial t} + \vec{v}\cdot\nabla v + fu = -\frac{1}{\rho}\frac{\partial p}{\partial y} + A_H\left(\frac{\partial^2 v}{\partial x^2} + \frac{\partial^2 v}{\partial y^2}\right) + \frac{1}{\rho}\frac{\partial \tau_y}{\partial z} \qquad (3.1)$$

where $\vec{v}$ is the velocity, having components u and v in the x (northward) and y (eastward) coordinate directions; p is pressure; f is the Coriolis parameter; ρ is density; τ_x and τ_y are components of Reynolds stress due to vertical shear in the horizontal velocity field ; A_H is the horizontal eddy viscosity. (We consider A_H to be a constant with respect to the horizontal coordinates; this is an unrealistic assumption for flow adjacent to a coastal boundary, but here we are looking for qualitative effects and so would not gain by introducing higher order complexity into the lateral frictional aspect.) For convenience, we define a "horizontal gradient" operator, $\nabla_H \equiv \vec{i}\frac{\partial}{\partial x} + \vec{j}\frac{\partial}{\partial y}$.

Because the rotation of the earth exerts such a strong control on large scale fluid flows, it is possible to express much of the essential dynamics of the vector velocity field in terms of a single scalar quantity, the vorticity, $\zeta \equiv \vec{k}\cdot\nabla\times\vec{v}$. This allows the major dynamical balance between pressure force and Coriolis deflection to be incorporated implicitly rather than explicitly.

Cross-diffentiating and subtracting the component equations of Eq. 3.1, interchanging order of differention, and rearranging, yields a quite general form of the

vorticity equation for horizontal ocean flow,

$$\rho\left\{\frac{\partial \zeta}{\partial t} + \vec{v}\cdot\nabla\zeta + (f+\zeta)\nabla_H\cdot\vec{v} + v\frac{df}{dy} - A_H\left(\frac{\partial^2\zeta}{\partial x^2}+\frac{\partial^2\zeta}{\partial y^2}\right)\right\} = \frac{\partial}{\partial z}\left(\vec{k}\cdot\nabla\times\vec{\tau}\right) \qquad (3.2)$$

wherein the pressure term no longer explicitly appears; here we have neglected the "tilting term", $\frac{\partial w}{\partial x}\frac{\partial v}{\partial z} - \frac{\partial w}{\partial y}\frac{\partial u}{\partial z}$, which can be shown to be much smaller than other terms in the equation for the scales addressed in this study.

III.2 Sverdrup Balance?

In investigating the large scale, long-term mean dynamics of the ocean, the time-dependent, advective, and lateral frictional terms of Eq. 3.2, are often assumed to be negligible. This leaves a balance between: (A) vortex stretching, (B) advection of planetary vorticity, and (C) vertical Reynolds stress, i.e.,

$$\underset{(A)}{\rho(f+\zeta)\nabla_H\cdot\vec{v}} + \underset{(B)}{\rho v\frac{df}{dy}} = \underset{(C)}{\frac{\partial}{\partial z}\left(\vec{k}\cdot\nabla\times\vec{\tau}\right)} \qquad (3.3)$$

We use the equation of continuity for incompressible flow to replace $\nabla_H\cdot\vec{v}$ by $-\frac{\partial w}{\partial z}$, and vertically integrate Eq. 3.3 from the ocean bottom (z=-h) to the sea surface (z=0), i.e.,

$$-\int_{-h}^{0}\rho(f+\zeta)\frac{\partial w}{\partial z}\,dz + \frac{df}{dy}\int_{-h}^{0}\rho v\,dz = \int_{-h}^{0}\frac{\partial}{\partial z}\left(\vec{k}\cdot\nabla\times\vec{\tau}\right)dz \qquad (3.4)$$

On the large time and space scales we are addressing here, relative vorticity of ocean flow is generally small compared to planetary vorticity. Since we are interested here only in considering the order of magnitude of the vortex stretching effect, we will neglect the relative vorticity in order to make the equation linear with respect to velocity; we can safely neglect variation in density. We "change variables" and rewrite Eq. 3.4 as

$$-\rho f \int_{\omega_b}^{0} d\omega + V\frac{df}{dy} = \int_{\vec{k}\cdot\nabla\times\vec{\tau}_b}^{\vec{k}\cdot\nabla\times\vec{\tau}_s} d(\vec{k}\cdot\nabla\times\vec{\tau}) \tag{3.5}$$

where V represents the depth-integrated mass transport, i.e., $V = \int_{-h}^{0} \rho v\, dz$; $\vec{\tau}_s$ and $\vec{\tau}_b$ represent the respective tangential stresses at the sea surface and at the sea floor; ω_b is the vertical component of velocity at the sea floor. Performing the integrations yields

$$\underset{(A)}{\rho f \omega_b} + \underset{(B)}{V\frac{df}{dy}} = \underset{(C)}{\vec{k}\cdot\nabla\times\vec{\tau}_s} - \underset{(D)}{\vec{k}\cdot\nabla\times\vec{\tau}_b} \tag{3.6}$$

which expresses a balance between (A) vortex stretching due to bathymetric variations, (B) meridional advection of planetary vorticity, (C) input of vorticity at the sea surface by wind stress curl, and (D) dissipation of vorticity in the frictional boundary layer at the ocean bottom.

The condition of no flow through the ocean bottom yields

$$-w_b = u_b \frac{\partial h}{\partial x} + v_b \frac{\partial h}{\partial y} \tag{3.7}$$

where u_b and v_b represent the horizontal velocity components near the sea floor (just outside of the frictional boundary layer). Thus the vertical component of velocity near the ocean bottom, on the large temporal/spatial scales with which we are dealing, results when flow near the ocean floor crosses bathymetric contours; alteration of the vorticity balance by vortex stretching (term A of Eq. 3.6) results whenever bottom flow is not precisely parallel to isobaths. Combining Eqs. 3.6 and 3.7 yields:

$$\underset{(A)}{-\rho f\left(u_b \frac{\partial h}{\partial x} + v_b \frac{\partial h}{\partial y}\right)} + \underset{(B)}{V \frac{df}{dy}} = \underset{(C)}{\vec{k} \cdot \nabla \times \vec{\tau}_s} - \underset{(D)}{\vec{k} \cdot \nabla \times \vec{\tau}_b} \tag{3.8}$$

If the effect of the ocean bottom is regarded as insignificant, terms A and D of Eq. 3.6 drop out and we are left with the classical "Sverdrup balance"

$$V \frac{df}{dy} = \vec{k} \cdot \nabla \times \vec{\tau} \tag{3.9}$$

proposed by Sverdrup (1947), wherein the vorticity input by the surface wind stress is exactly balanced by planetary vorticity advection. Equivalently, Eq. 3.9 expresses the fact that in a steady-state ocean, in which the only flow components are geostrophic currents and pure Ekman wind drift and in which bottom and lateral boundary effects are

not allowed, local conservation of fluid mass requires that surface Ekman divergence (convergence) due to wind stress curl must be exactly balanced by the geostrophic convergence (divergence) which is intrinsic to meridional geostrophic motion on a spherical earth.

Munk (1950) proposed maintenance of Sverdrup balance as an explanation for the poleward undercurrent off California. On viewing Nelson's (1977) California Current wind stress curl distributions, Hickey (1979) suggested that many of the seasonal and geographical features of the California Current flow system could be related to wind stress curl via a Sverdrup balance connection.

In considering the likelihood of depth-integrated Sverdrup Balance in eastern boundary current flow, it is instructive to estimate the possible magnitude of the terms (terms A and D in Eqs. 3.6 and 3.8) related to influences of the ocean bottom,which are neglected in the Sverdrup balance expression (Eq. 3.9).

Bottom Friction

We deal first with term D, the frictional effect. It is often assumed that the bottom stress can be estimated from the same quadratic stress law (Eq. 2.3) used to estimate the surface stress, using a drag coefficient of similar magnitude, but with the major difference that the density of water is used rather than the density of air. The density of water is about 820 times that of air and so

a ratio of wind speed 10 meters above the water surface to current speed 1 meter above the bottom equal to the square root of the reciprocal of 820, or 0.035, will yield roughly equivalent sea surface and ocean bottom stress magnitudes. We know little about the pattern of bottom currents. However, Stokes' theorem tells us that scales of variation of bottom stress curl which happen to be substantially smaller than those of the surface stress curl would cancel one another in their effect on Sverdrup balance. This implies that we need consider only scales comparable to the scales of surface stress variability for this purpose. Thus we can derive a useful gauge of the relative importance by simply comparing the likely stress magnitudes at large scale spatial maxima (i.e., by assuming the length scales over which the large scale stresses at the sea surface and at the ocean floor would vary from essentially zero to maximum values are the same).

For example, one could choose one dyne cm^{-2} per 1000 km (10^{-7} kg m^{-2} sec^{-2}) as a characteristic long term mean curl magnitude (Fig. III.1) for eastern boundary current regions. A stress of one dyne cm^{-2} would correspond to an instantaneous wind speed of 8 m sec^{-1}. A similar magnitude of bottom stress would result from flow velocities near the sea floor of 3.5 percent of this, or about 0.28 m sec^{-1}.

It is unlikely that velocities of this magnitude (i.e., greater than half a knot) exist over extensive areas

of the ocean bottom on anything but very short time scales. Therefore this particular term is unlikely to constitute a major interference to the maintenance of Sverdrup balance in eastern boundary current flows.

Bottom Slope

With respect to vortex stretching due to flow along a sloping ocean bottom (term A in Eq. 3.8), the situation is quite different. A slope of 0.04 is a reasonable choice for characteristic bottom slope (this is similar to the average inclination of the continental slope at depths shallower than 2000 m at about 45 degrees latitude off the coast of Oregon). With this choice, term A of Eq. 3.9 reaches a similar magnitude to the characteristic wind stress curl value we have chosen (i.e., 10^{-7} kg m^{-2} sec^{-2}) when cross-isobath flow velocities reach about 0.000025 m sec^{-1} (or about 0.00005 knots). Steady flows of such small magnitude are not unlikely near the ocean bottom and there are no convincing dynamical arguments to preclude their crossing isobaths. The conclusion is that vortex stretching due to flow across bottom contours might well be capable of overiding Sverdrup balance in these current systems.

III.3 The Long Term Annual Mean Wind Stress Curl and Depth-integrated Ocean Flow Features

We can expect the assumptions leading to Sverdrup balance to be more valid as time scales of variation become

longer. The time dependent term would be expected to become smaller when the energetic seasonal and shorter-scale variations have been filtered. Also, processes of baroclinic compensation, which would lead to more rapid attenuation of geostrophic flow with depth and correspondingly lessened influence of bottom boundary effects (terms A and D in Eq. 3.6), would be more complete at longer time scales.

Surface wind stress curl distributions constructed via the same procedures as described in Chapter 2, but based on long term annual composite stress summaries, are presented in Fig. III.1. (Note that we can discuss both northern and southern hemisphere dynamics in terms of Eqs. 3.5 to 3.9, as long as we consider the positive sense of the symbol sets ζ and $\vec{k} \cdot \nabla \times \vec{\tau}$ to be cyclonic, i.e., anti-clockwise in the northern hemisphere and clockwise in the southern hemisphere, and the positive directional sense of V to be poleward in either case.) Fig. III.1 indicates a general tendency for the ocean areas within several hundred km of the coast to be under the influence of cyclonic wind stress curl in all four regions illustrated.

Existence of poleward coastal undercurrents has been reported for all four regions. In addition, poleward surface currents tend to appear at seasons and locations of relaxed equatorward wind stress. Parrish et al. (1983) briefly review regional incidence of such flows. Cited

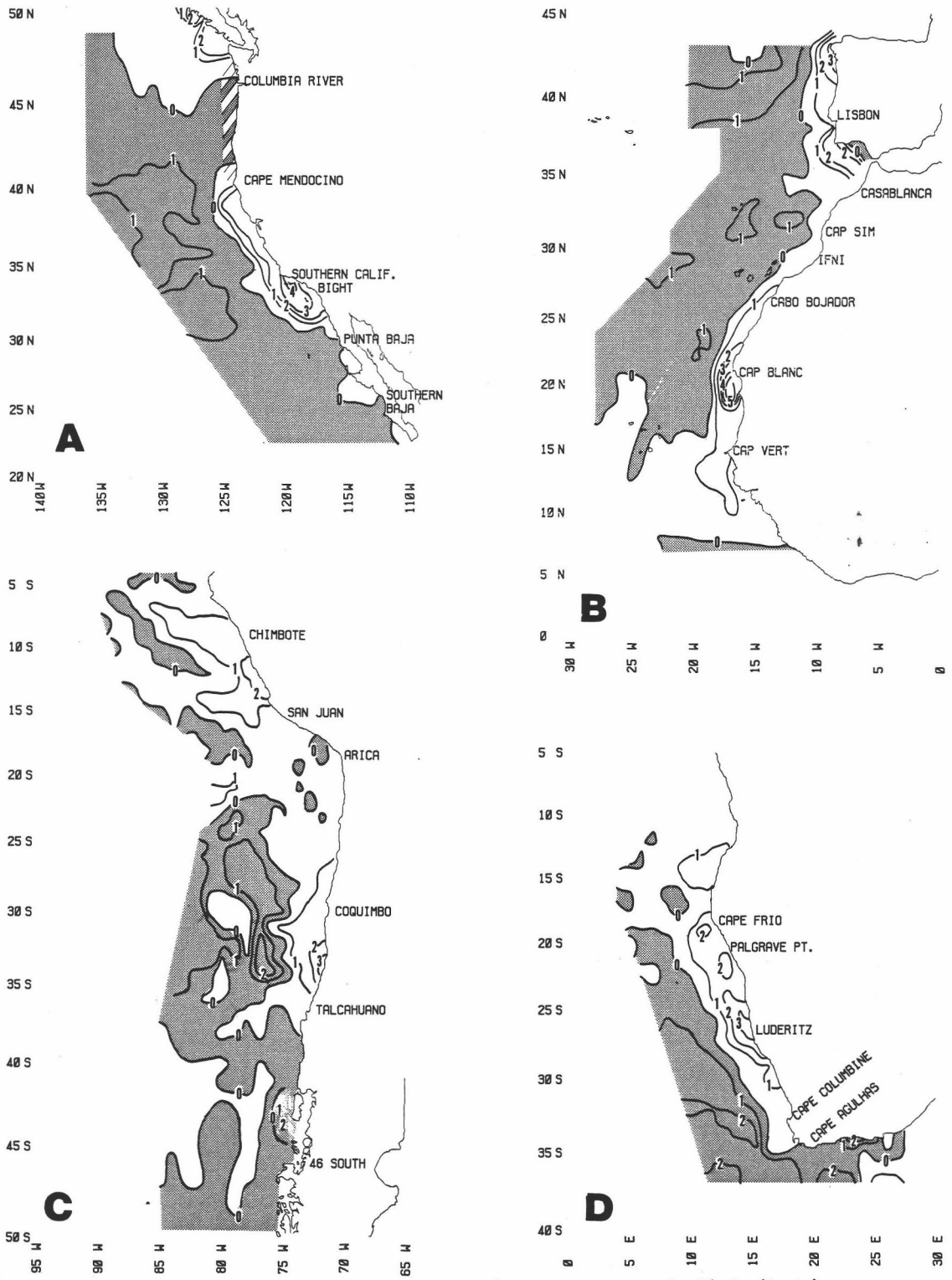

Figure III.1. Long term annual mean wind stress curl distributions. Units are dyne cm^{-2} per 1000 km (10^{-7} kg m^{-2} sec^{-2}); regions of anticyclonic wind stress curl are shaded and regions of cyclonic wind stress curl are unshaded. The four panels depict the areas defined in Fig. II.2: A. California Current region; B. Canary Current region; C. Peru/ Humboldt Current region; D. Benguela Current region.

references for the California Current region include Wooster and Jones (1970), Reed and Halpern (1976); for the Peru Current region , Wyrtki (1965) and Silva and Neshyba (1979); for the Canary Current region, Mittlestaedt (1974) and Hughes and Barton (1974); for the Benguela Current region, Hart and Currie (1960), Stander (1964), Nelson and Hutchings (1983).

Thus, the general pattern of large-scale equatorward flow in the offshore regions and existence of poleward counterflows near the coast is consistent with the long term mean wind stress curl patterns interpreted in a Sverdrup balance sense. However, the cautions presented earlier in this chapter may be appropriately reiterated here. We have indicated the ease with which Sverdrup balance might be destroyed by even a very slight degree of cross-isobath flow near the ocean bottom. We have also recognized that the coastal boundary is a feature which is common to all of the regional systems we are examining. Therefore it is difficult to separate effects of mechanistic linkages of the ocean flow to boundary-related features in the wind stress pattern from boundary effects which might be occurring independently and separately in the atmospheric and oceanic fluid flows.

In any case, authors of theoretical models of eastern ocean boundary poleward undercurrent dynamics which feature cyclonic wind stress curl as a contributing factor (e.g.,

Hurlburt and Thompson, 1973; Pedlosky, 1974; McCreary, Kundu, and Chao, 1987) can be comfortable in the fact that, on a long term average basis, cyclonic curl is a general characteristic of the regions where these flows are known to occur.

III.4 Poleward Subsurface Coastal Flows Where the Long Term Mean Wind Stress Curl is Anticyclonic

Certain exceptions to the generality stated in the previous paragraph deserve mention. These include the area off the Mexican coast near Punta Baja, the area off the coast of Chile south of Talcahuano, and the area off the western U.S.A. from somewhat north of Cape Mendocino to the vicinity of the Columbia River.

Punta Baja

As discussed in Section II.4, the area off Punta Baja exhibits a consistent tendency for a lobe of anticyclonic curl to extend from the offshore region to the coast, at all seasons of the year. However a poleward undercurrent is reported for this region (Wooster and Jones, 1970). Note however that Wooster and Jones cite the width of the undercurrent in this area as being only 20 km. In fact Wyllie's (1966) long-term mean seasonal charts of geostrophic flow at 200 m relative to 500 db (e.g., Fig. III.2) show the undercurrent to narrow greatly in this region relative to the areas to the north and south, which are characterized

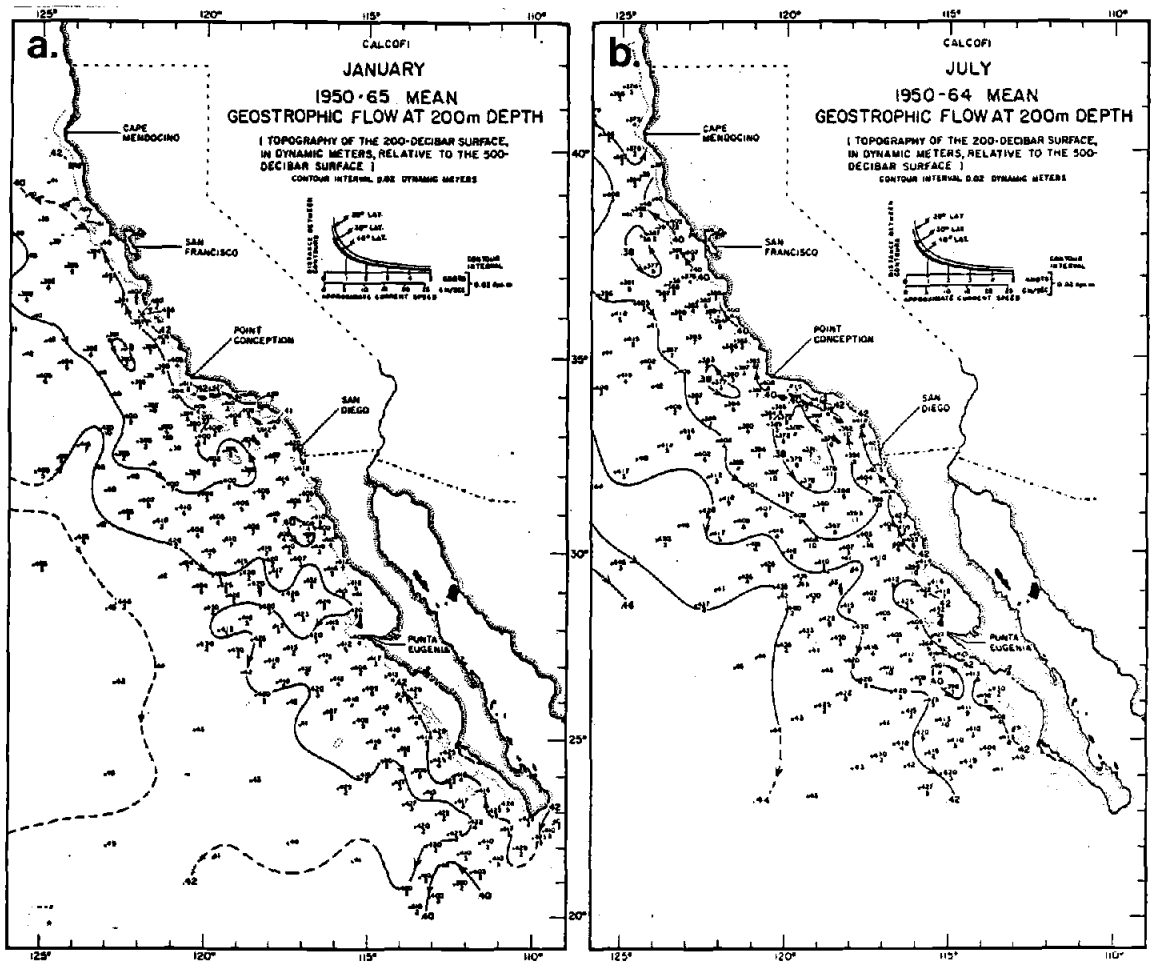

Figure III.2. Long term (1950-65) monthly mean dynamic topography (dyn. m) at 200 m relative to 500 db (after Wyllie, 1966). **(a)** January. **(b)** July.

by cyclonic wind stress curl (Fig. III.1a).

The wind stress curl estimates are computed as differences of adjacent one-degree latitude/longitude areal averages (see Section II.1), and so the scale of resolution is much larger than 20 km. Punta Baja is a local upwelling center (Bakun and Nelson, 1977) and represents a local maximum of equatorward alongshore stress. As discussed in Section II.8, the stress distribution off capes during upwelling seasons tends to have an offshore profile which resembles a lateral frictional boundary layer (i.e., retardation of the wind at the coast and an offshore maximum). It is almost inconceivable that similar frictional effects would not act, on some scale, off Punta Baja. Therefore, it seems safe to postulate the existence of a subgrid-scale lateral coastal boundary layer of cyclonic wind stress curl at this location. The variation in width of the subsurface poleward flow would conform to the variation in width of the characteristic zone of coastal cyclonic wind stress curl off the Mexican coast. In view of these considerations, rather than being an exception to the general pattern that cyclonic curl characterizes the long-term mean wind stress field overlying regions of eastern boundary poleward undercurrents, the situation near Punta Baja appears to offer the sort of special case which "proves the rule".

The Area South of Talcahuano

The area off the Chilean Coast, from somewhat south of Talcahuano to just north of the major coastal indentation at the Golfo de Ancud (39° S lat), is characteristically under the influence of anticyclonic wind stress curl (Fig. III.1), although this may vary seasonally (Fig. II.7). Because of the paucity of surface marine data for this region it is difficult to draw any categorical conclusion.

Likewise, hydrographic data are nearly lacking. However, Sandoval (1971) has presented distributions which include a few stations in the area. He shows poleward flow at 200 m (relative to 500 db) to be greatly narrowed in seaward extent compared to areas to the north and south (Fig. III.3a); at 100 m he finds poleward flow to be entirely absent within 600 km of the coast from about latitudes 36° S to 39° S. (Fig. III.3b). Silva and Neshyba (1979), while indicating subsurface properties suggesting continuous poleward subsurface advection to 48° S lat, have no station data within the area in question and so must extapolate dynamic topography through the area from station lines to the north and to the south; thus their distributions yield no real information as to variation in undercurrent width in this location.

In general, the little information that is available suggests an effect on the seaward extent of subsurface poleward flow of an apparent lack of large scale cyclonic

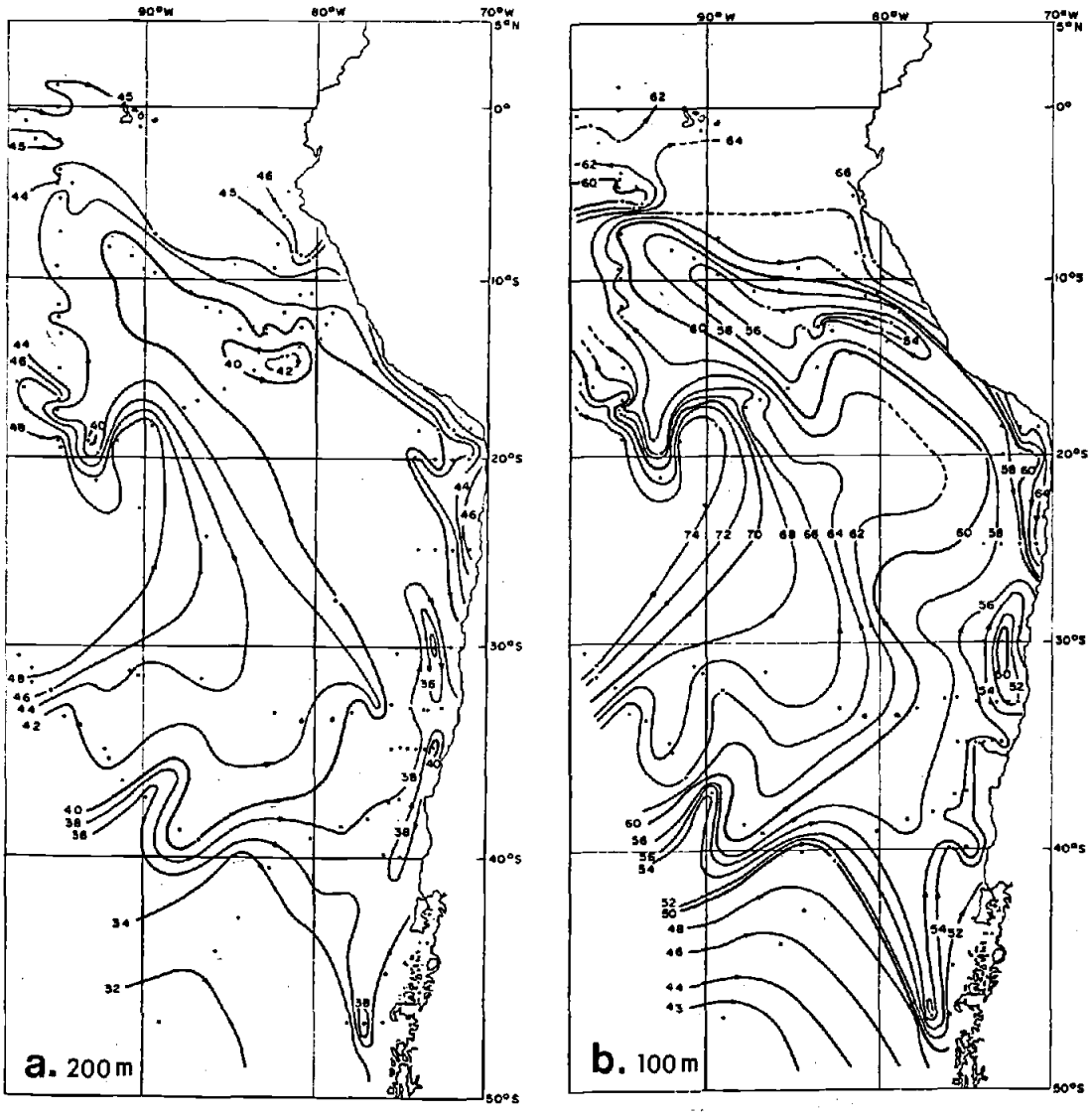

Figure III.3. Geopotential topography (dyn. cm) relative to 500 db (after Sandoval, 1971), **(a)** at 200 m depth; **(b)** at 100 m depth.

wind stress curl near the coast, similar to the effect observed off Punta Baja in the California Current region.

The Oregon Coast

The situation of ambiguous characteristic wind stress curl, in the near-coastal region from somewhat north of Cape Mendocino to the vicinity of the Columbia River, has been discussed in Section II.4. A strong seasonality has been noted such that moderately intense large scale cyclonic curl occupies the area from June through September (Fig. II.4). Hickey (1979) notes that most of the observations of a poleward undercurrent within the area are from the summer and early fall seasons, and also that the percentage of water which appears to be of southern origin increases significantly from July to September, evidently decreasing at some time during the remaining portion of the year.

Poleward of about 45° lat in both hemispheres, there is a tendency for strong wind stress to be directed onshore or poleward during the respective winter seasons (Figs. II.4b, and II.7b). Since the winter situations are by far the more energetic in terms of atmospheric activity, these regions are really part of a regime which is basically different from that of the classical eastern boundary upwelling regions. The alongshore forcing tendencies are poleward rather than equatorward, and so discussing countercurrents in the same "comparative analogue" context may be

inappropriate.

III.5 Vorticity Balance in the Near-surface Flow Field

Depth-integrated flow is difficult to indicate unequivocally without direct flow measurements, which are not generally available on the scales we are attempting to address in these comparisons. Surface flow patterns are easier because the geostrophic velocity field at the surface is generally fairly large compared to the uncertainties in the velocity field at the reference depth, at least at periods of variation longer than about a day. To focus consideration on the vorticity balance near the sea surface we integrate Eq. 3.2 over the relatively homogeneous surface layer, from a level geopotential surface, $z=-\delta$, near the top of the pycnocline, to the sea surface; i.e.,

$$\rho\left\{\underbrace{\int_{-\delta}^{0}\frac{\partial\zeta}{\partial t}\,dz}_{(A)}+\underbrace{\int_{-\delta}^{0}\vec{v}\cdot\nabla\zeta\,dz}_{(B)}+\underbrace{\int_{-\delta}^{0}(f+\zeta)\nabla_H\cdot\vec{v}\,dz}_{(C)}+\underbrace{\frac{df}{dy}\int_{-\delta}^{0}v\,dz}_{(D)}\right.$$

$$\left.-\underbrace{\int_{-\delta}^{0}A_H\left(\frac{\partial^2\zeta}{\partial x^2}+\frac{\partial^2\zeta}{\partial y^2}\right)dz}_{(E)}\right\}+\underbrace{\vec{k}\cdot\nabla\times\vec{\tau}_\delta}_{(F)}=\underbrace{\vec{k}\cdot\nabla\times\vec{\tau}_s}_{(G)} \qquad (3.10)$$

where $\vec{\tau}_s$ and $\vec{\tau}_\delta$ refer to the wind stress on the sea surface and the horizontal shear stress at the bottom of the mixed layer, respectively. Eq. 3.10 expresses the balance in the

upper "mixed" layer among: (A) local rate of change of relative vorticity averaged over the layer, (B) advection of relative vorticity averaged over the layer, (C) vortex stretching due to horizontal flow divergence averaged over the layer, (D) advection of planetary vorticity averaged over the layer, (E) lateral eddy diffusion of vorticity averaged over the layer, (F) vertical transfer of vorticity by frictional coupling through the interface at the bottom of the layer, and (G) input of vorticity at the sea surface due to wind stress curl.

It is useful, at this point, to briefly discuss the likely general tendencies of the terms in Eq. 3.10. The relative vorticity observed in surface current distributions computed geostrophically from hydrographic data is invariably small compared to f. For example, consider the case of the elongate gyre situated in the band from 10 to 12 degrees latitude off the coast of Peru in the distributions presented by Sandoval (1971), where tight dynamic height contours (perhaps drawn more tightly than justified by the station pattern) yield velocity component differences of the order of 30 cm sec^{-1} over a length scale of less than 3 degrees latitude (Fig. III.3b). In spite of the low-latitude location, f exceeds the relative vorticity by a factor of about twenty. Thus, on the scales of this comparison, terms A and B of Eq. 3.10 are generally small compared to term D.

Term C - vortex stretching

The balance between terms C and G in Eq. 3.10, i.e., between wind stress curl and vortex stretching against absolute vorticity, represents the effect of Ekman pumping. This balance regulates, for example, "oceanic upwelling" (Smith, 1968), i.e., moderately long-period, directly wind-driven divergence or convergence seaward of the coastal boundary zone (of width comparable to the baroclinic Rossby radius).

Spatial variation in this balance will result in differential rearrangements of mass due to spatial gradients in rate of either uplift of heavier water or downward forcing of lighter surface water. Continuation of this process over time leads to growth of a baroclinic horizontal pressure gradient in the region of the surface mixed layer and upper pycnocline. The result after some time interval will be development of geostropic current flow perpendicular to the pressure gradient, and thus perpendicular to the horizontal gradient of wind stress curl. More detailed discussion of the evolution of baroclinic current in the upper ocean layer, related to horizontal gradient of wind stress curl will be presented in Section III.6.

Term D - advection of planetary vorticity

'Beta'(i.e., $\frac{df}{dy}$) varies from 2.25×10^{-11} sec^{-1} m^{-1} at 10° lat to 1.47×10^{-11} sec^{-1} m^{-1} at 50° lat; we choose a characteristic value of 2×10^{-11} for comparison. We

choose 50 m as a reasonable typical depth of the surface relatively homogeneous layer (e.g., see Table 5 in Parrish et al., 1983). With these choices, and an upper layer mean meridional velocity of 0.1 m sec^{-1}, term D is equal to the characteristic wind stress curl value of 1 dyne cm^{-2} per 1000 km (10^{-7} kg m^{-2} sec^{-2}) chosen in Section III.2. We thus see that equivalence in order of magnitude of terms D and G in Eq. 10.3 is likely and that Sverdrup balance within the surface layer is a possibility.

Term E - lateral diffusion of vorticity

In the vicinity of the coastal boundary, diffusion of vorticity from the coastal boundary layer may be appreciable. Where the alongshore flow is equatorward, a frictional boundary layer at the coast would generate cyclonic vorticity. We have seen that the same tendency occurs in the overlying wind field. Thus, lateral diffusion from a coastal frictional boundary layer would tend to augment the input of vorticity from the wind rather than counteract it.

However, it has been noted that there is often an alongshore equatorward "jet" associated with coastal upwelling (Allen, 1973), which is "sub-scale" with respect to the wind stress curl distributions presented herein (and therefore sub-scale with respect to flow features which we are able consider in this comparison). In this case, vorticity generation on the seaward side, i.e., available for diffusion to the larger offshore scales, would be

anticyclonic.

In general, the class of distinctly coastal processes which have offshore scales comparable to the baroclinic Rossby radius of deformation, (e.g., coastal upwelling, etc.) must all be considered as sub-scale boundary effects in terms of the wind stress curl comparisons attempted herein.

Term F - vertical transfer of vorticity through the lower interface

Little is known about vertical frictional coupling through the thermocline. It is often considered to be small, i.e., that the interface at the lower boundary of the upper layer is essentially frictionless. Certainly, vertical eddy diffusion is inhibited at the thermocline, as indicated by the steep vertical gradients in various properties. On the large time and space scales which are addressed in this study, horizontal velocity tends to decrease with depth. Thus, any effect of term F would act to dissipate the vorticity existing in the upper layer. On the other hand, in areas known to contain strong shallow subsurface counterflows, it is possible that vertical diffusion of vorticity could have substantial effects on the vorticity balance within the upper layer.

III.6 Evolution of Baroclinic Surface Current Associated With the Horizontal Gradient of Wind Stress Curl

Consider a situation of balance of terms C and G in Eq. 3.10, i.e.,

$$\int_{-\delta}^{0} \rho(f+\zeta)\nabla_H \cdot \vec{v}\, dz = \vec{k} \cdot \nabla \times \vec{\tau}_s \tag{3.11}$$

Eq. 3.11 represents a situation where the total effect, on the surface layer of interest, of the curl of the wind stress on the sea surface is manifested as Ekman pumping through the bottom of the layer. For example, substiing the equation of continuity, $\nabla_H \cdot \vec{v} = -\frac{\partial w}{\partial z}$, neglecting ζ compared to f, neglecting variation in ρ, and changing variable in the integral, yields

$$-\rho(f+\zeta)\int_{w(z=-\delta)}^{0} dz = \vec{k} \cdot \nabla \times \vec{\tau}_s \tag{3.12}$$

Performing the integration yields

$$\rho(f+\zeta)\, w_\delta = \vec{k} \cdot \nabla \times \vec{\tau}_s \tag{3.13}$$

where w_δ refers to the upward velocity at the bottom of the layer.

If we take the horizontal gradient of Eq. 3.13, this time considering ρ and $(f+\zeta)$ to be essentially constants with respect to the horizontal scale of variation in Ekman

pumping, the result is

$$\rho (f+\zeta) \nabla_H w_s = \nabla_H \left(\vec{k} \cdot \nabla \times \vec{\tau}_s \right) \qquad (3.14)$$

The horizontal gradient in vertical vertical velocity at the bottom of the layer, expressed in Eq. 3.14, implies alteration of the horizontal density field in the upper layer, leading to alteration in the field of horizontal pressure gradient force in the direction of the gradient of wind stress curl (Fig. III.4). On the time scales addressed in this discussion, the modified pressure gradient force would be accompanied by corresponding modifications in the geostrophic flow field, directed perpendicularly to the pressure gradient. Thus, to the extent that the vorticity balance in the upper layer is largely between wind stress curl and vortex stretching (i.e., Ekman pumping), a horizontal gradient in wind stress curl would lead, over time, to inducement of upper layer geostrophic flow directed perpendicularly to that gradient. The proper directional sense is such that a person facing in the direction of flow, will have anticyclonic wind stress curl tendency directed toward his right (left) in the northern (southern) hemisphere.

Thus, in our comparative examination of eastern boundary surface current distributions, we merely look (on

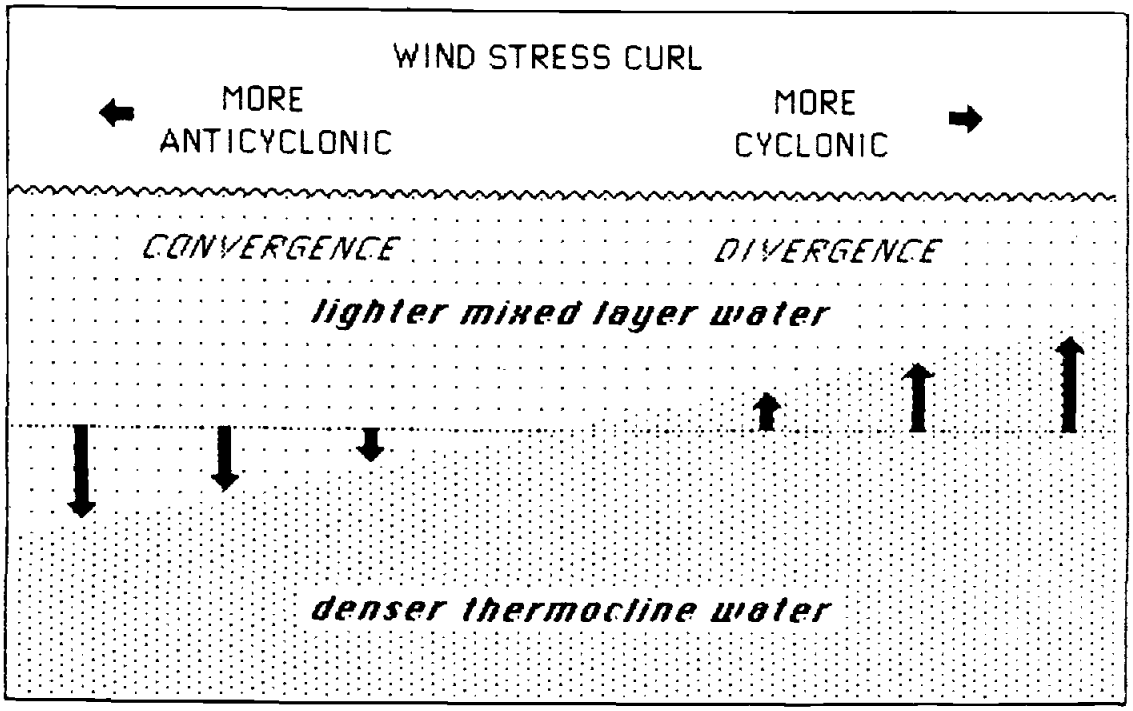

Figure III.4. Schematic diagram of the '*gradient of the wind stress curl / differential vortex stretching*' mechanism. To the extent that vorticity input at the sea surface due to wind stress curl is balanced by vortex stretching in the upper layer, horizontal gradients in wind stress curl induce corresponding gradients in rate of vortex stretching (i.e., Ekman pumping). This generates sloping of the internal density structure of the upper ocean in the direction of the wind stress curl gradient (upward slope toward greater cyclonic wind stress curl tendency; downward slope toward greater anticyclonic wind stress curl tendency), leading to the development of a baroclinic pressure gradient force directed from greater anticyclonic tendency toward greater cyclonic tendency in the wind stress curl pattern. Geostrophic surface current, in equilibrium with this force, is directed perpendicular to the wind stress curl gradient (i.e., parallel to wind stress curl contours).

whatever time scale data may be available) for patterns of correspondence of maxima in horizontal gradient of wind stress curl with perpendicularly-directed surface flow maxima (i.e., for surface dynamic topography contours to follow wind stress curl contours), in the proper directional sense, in order to evaluate the importance of this particular mechanism.

III.7 Long Term Annual Mean Surface Geostrophic Flow

Parrish et al. (1983) presented long term annual mean distributions of surface dynamic topography for the four regions (Fig. III.5). These were computed from analyzed fields of annual mean temperature and salinity constructed by Levitus (Levitus and Oort, 1977; Levitus, 1982). The analysis procedures were designed for ocean basin-scale, rather than regional-scale, flow descriptions and so the derived flow patterns are very highly smoothed with respect to spatial variation. However, there are no higher-resolution fields available, on a consistent basis, for all four of the regions which we wish to compare. Therefore, we will look for initial insights into the upper layer vorticity balance on this highly smoothed scale, and then look to available anecdotal flow patterns for smaller scale tuning of these insights. (To facilitate comparison, the general locations of anticyclonic curl features, from Fig. III.1, are indicated by stippled shading in Fig. III.5.)

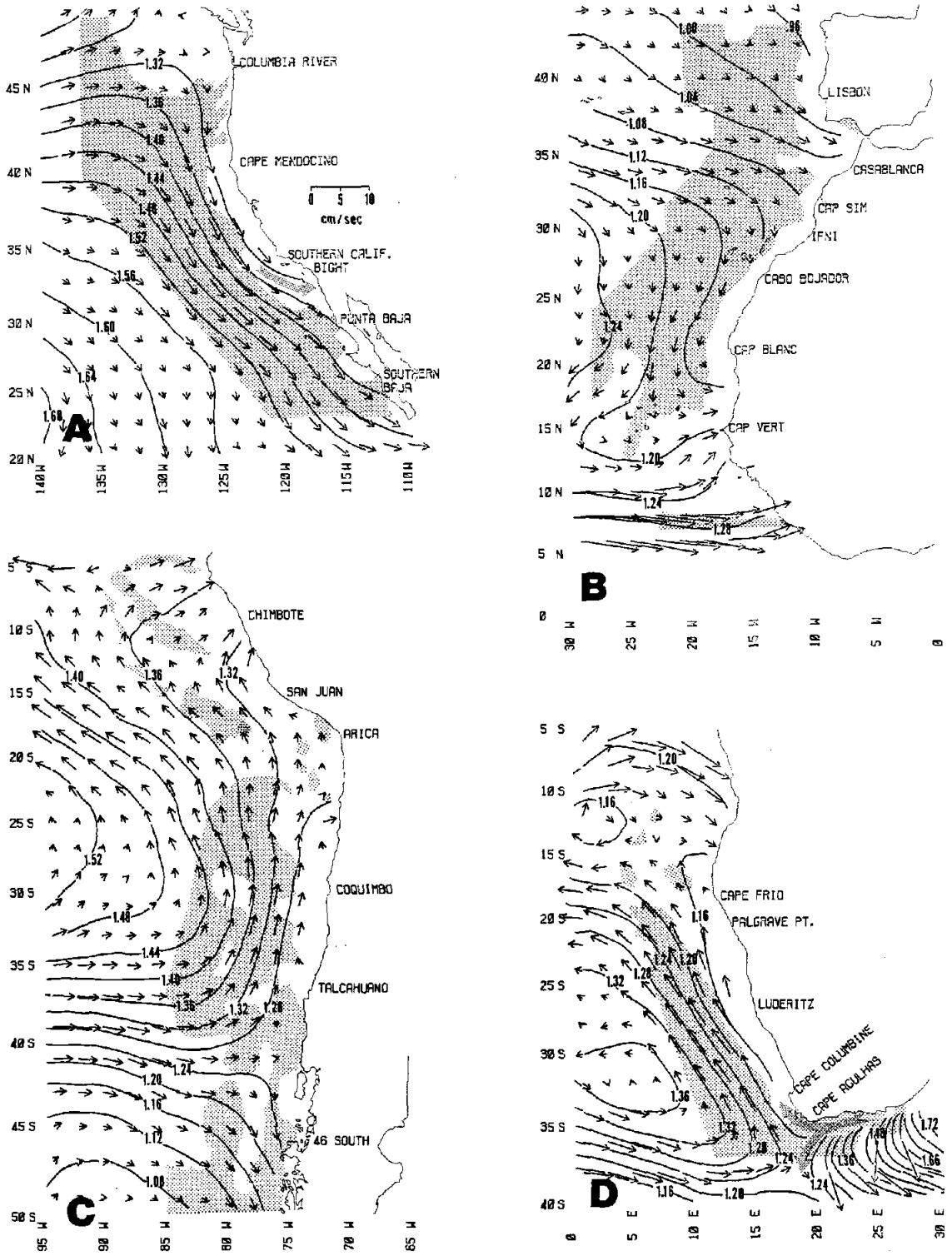

Figure III.5. Long term mean surface dynamic topography (dyn. m) relative to 500 db (after Parrish et al., 1983). Vector symbols indicate surface velocity (a symbol length scale appears on upper left diagram). Areas of anticyclonic curl (Fig. III.1) are superimposed via stipled shading. A. California Current region; B. Canary Current region; C. Peru/Humboldt Current region; D. Benguela Current region.

In Section III.5, it was shown that Sverdrup balance in the upper 50 m would occur for meridional velocity of about 10 cm sec^{-1} for wind stress curl magnitude of 1 dyne cm^{-2} per 1000 km. We see that many regions of Fig. III.5 contain equatorward velocities, generally less than 5 cm sec^{-1}, in regions of anticyclonic wind stress curl. Thus, such current speeds are not inconsistent with Sverdrup balance over layers several times deeper than 50 m; transfer of vorticity input from the wind to layers below the upper pycnocline limit might occur through vortex stretching in response to flow divergence in the layer above, or perhaps through direct vertical diffusion of vorticity, to allow Sverdrup balance over the larger depth intervals.

There also is a general tendency for greatly reduced equatorward surface flow, or for poleward flow, corresponding to regions where cyclonic wind stress curl is indicated. For example, note the region off West Africa south of Cap Vert where the sign of the curl of the characteristic wind stress changes at about 8° N lat; a change in flow tendency from poleward to equatorward corresponds. The changes to generally poleward flow tendencies where cyclonic wind stress curl tends to become dominant at about 45°N in the California Current region and at about 40°S in the Peru-Chile region, are in directional correspondence with Sverdrup balance. The situation (west

of Cape Agulhas) in the Benguela region appears likewise to be in general directional accordance.

However, the Peru Current region, equatorward of about 25° S lat, presents a notable exception. Here, in spite of a general predominance of cyclonic wind stress curl, the large scale characteristic surface flow is invariably equatorward. Moreover, the notion that a requirement for local Sverdrup balance may control the surface flow pattern would imply some pattern of correspondence of maxima in meridinal flow with local maxima in wind stress curl. Such a pattern is not evident in these long term annual mean distributions (Figs. III.1 and III.5). For example, off California, the region of strongest equatorward flow is situated consistently shoreward of the region of anticyclonic wind stress curl maximum, in the region of strong curl gradient. Likewise, a local anticyclonic wind stress curl maximum indicated by the pair of closed contours off Cap Sim, in the Canary Current region, seems to be associated with a predominently eastward (i.e., normal to the curl gradient) flow maximum immediately to the north.

Other similarities in the shapes of wind stress curl contours and dynamic topography contours, suggestive of the mechanism for differential vortex stretching related to horizontal gradient in wind stress curl (and associated Ekman pumping) discussed in Section III.6, can be found. By

definition, surface geostrophic flow is along contours of surface dynamic topography. Where dynamic height contours have the same shape as wind stress curl contours, flow is therefore perpendicular to the horizontal gradient of wind stress curl, and therefore suggestive of this particular mechanism. Note, for example, the intersection with the coast of South America between Arica and Coquimbo, of a wind stress curl contour (Fig. III.1) and a dynamic height contour (Fig.III.5). Likewise, note a similar coastward curving of the respective contours, just to the north of Cape Frio in the Benguela region. Note also the indication of particularly strong eastward flow at about 8° N off West Africa, corresponding to a change in sign of wind stress curl; near the equator the Coriolis parameter becomes small leading to an amplified effect of gradient of the wind stress curl on the production of surface layer baroclinicity (Eq. 3.16).

Another feature of Fig. III.5 is a tendency for curvature in streamlines of surface geostrophic current to be anticyclonic where the overlying wind stress curl is anticyclonic and to be cyclonic where the wind stress curl is cyclonic. Examples include the direction of curvature of the broad "westerly" currents (which flow from the ocean interiors toward the continents, poleward of about 30° lat, in all four of the regions) to flow parallel to the coasts near the continental boundaries; of course in these

instances it is difficult to know how much of the correspondence may be due to separate similar effects of the continental barrier occurring in the respective atmospheric and oceanic fluid flows, rather than to mechanistic linkages between the flows. However, a tendency for cyclonic curvature of the large scale geostrophic ocean surface flows toward the coastal bondaries, in regions equatorward of about 15° lat which are characterized by cyclonic wind stress curl, does not at all "mirror" the overlying wind stress pattern in which the cyclonic curl is related largely to an offshore shear in the predominently alongshore stress fields (Figs. II.4 to II.7).

The dynamic significance, of this tendency for curvature in the ocean flow pattern to be in the same sense as the overlying wind stress curl pattern, may be to diffuse vorticity, added at the ocean surface, downward to deeper layers via viscous drag and associated vortex stretching. The result is downward transfer of upper layer vorticity to the larger depth intervals over which depth-integrated Sverdrup balance could conceivably hold.

III.8 Seasonal Cycle: Central California to Southern Baja California

In this section, the focus shifts from the long term mean situation to the most basic and regular of time-dependent variations, the annually-repeating seasonal

cycle. Characteristic surface dynamic topographies are not available on a seasonal basis for the southern hemisphere systems of interest. Therefore, we concentrate at this stage on the seasonal flow patterns available for portions of the California Current and Canary Current systems. These particular patterns are based on summaries of designed hydrographic surveys of the respective regions, rather than on data which has been analyzed on a global-scale regularly-spaced grid system (as is the case for Fig. III.5); thus in this section the discussion also shifts toward improved spatial resolution.

A standard pattern of hydrographic stations has been regularly occupied in the California Current region for a number of years as part of the CalCOFI program. Unfortunately the portion of the region covered, from central California to southern Baja California, is the one for which seasonal variation in wind stress curl is the less dramatic. The most complete seasonal surface dynamic topographies have been produced by Lynn, Bliss, and Eber (1982). (These are reproduced in Fig. III.6, with the addition of shading to delineate major features of wind stress curl defined in Fig. II.4.)

The winter flow pattern (Fig. III.6a) includes a substantial poleward surface flow along the coast north of Point Conception, extending southward through much of the Southern California Bight, resulting in an elongate cyclo-

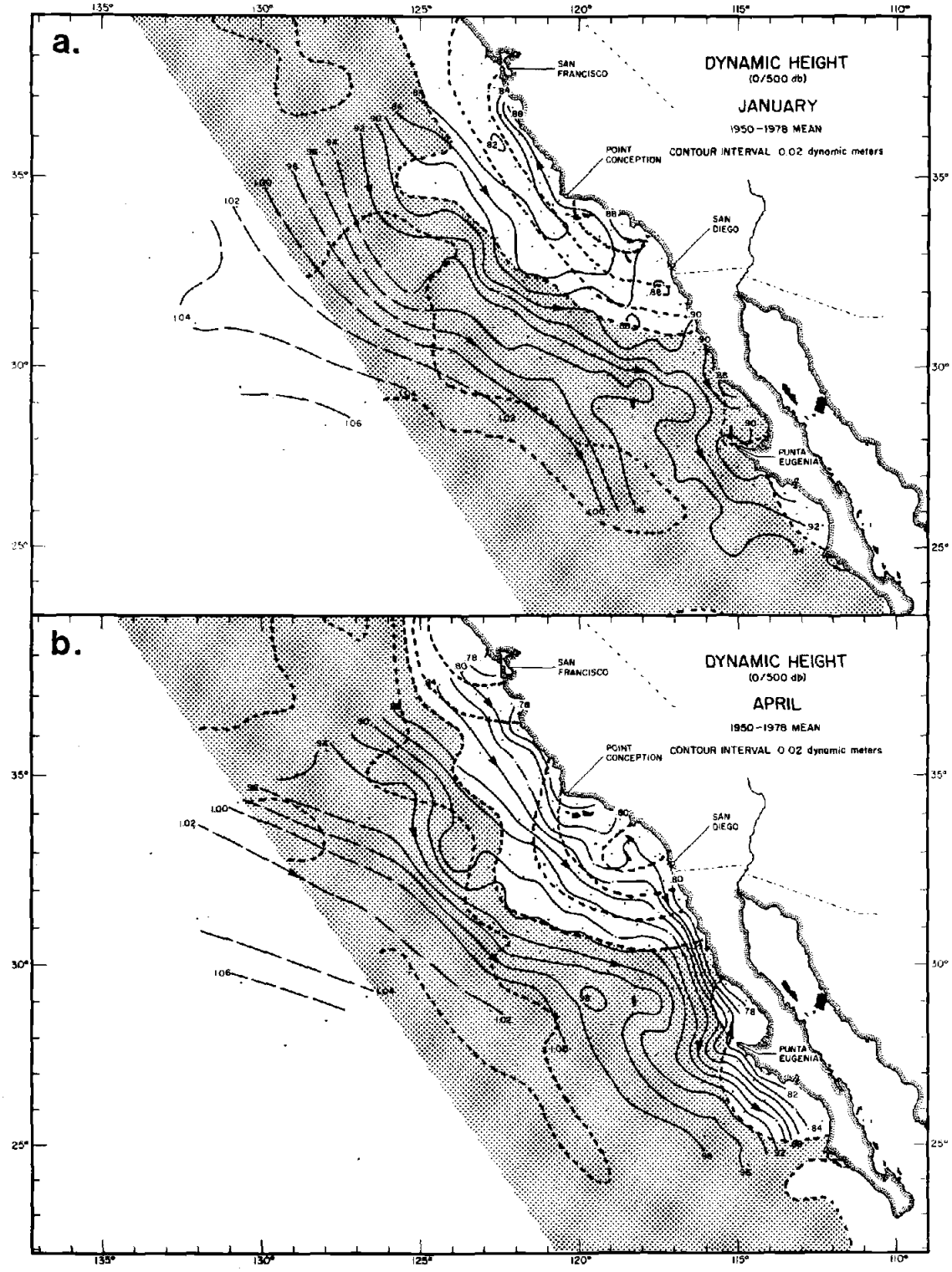

Figure III.6. Seasonal mean surface dynamic topography (after Lynn, et al., 1982). **(a)** January; 'Dec-Jan' wind stress curl distribution (Fig. II.4b) is superimposed via dashed contours and stippled shading. **(b)** April; 'Apr-May' wind stress curl pattern (Fig. II.4d) is superimposed.

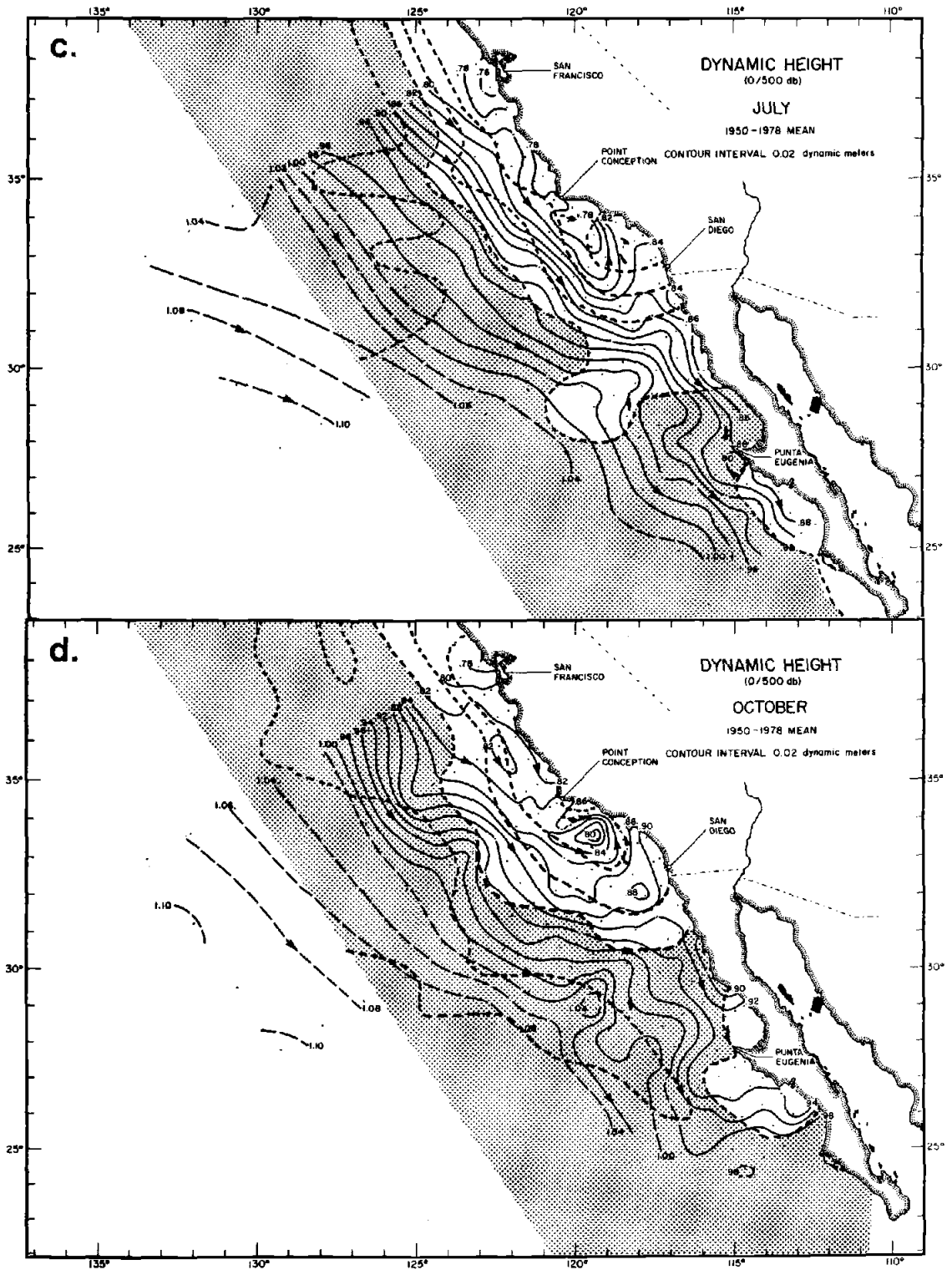

(Figure III.6, cont'd) **(c)** July; 'Jun-Jul' wind stress curl distribution (Fig II.4e) is superimposed via dashed contours and stippled shading. **(d)** October; 'Oct-Nov' wind stress curl pattern (Fig. II.4a) is superimposed.

nic gyral circulation pattern that corresponds strikingly in shape to the region of substantial cyclonic wind stress curl extending northward from the Bight during the fall and early winter season (Figs. II.4a and II.4b). The large scale equatorward flow bends sharply toward the coast off northern Baja California, following the general shape of the lobe of anticyclonic wind stress curl that extends coastward from the offshore region in the vicinity of Punta Baja (30° N). The flow in the region off Punta Baja is relatively diffuse during winter.

During spring (Fig. III.6b) poleward surface flow vanishes along the coast over the entire area. The equatorward flow off Baja California intensifies dramatically, and is concentrated adjacent to the boundary; this intensification corresponds to a local seasonal maximum of alongshore wind stress off Punta Baja (Fig. II.4d). As discussed in Section III.4, a narrow subgrid-scale band of cyclonic wind stress curl undoubtedly exists directly adjacent to the coast at this location resulting in a particularly intense horizontal curl gradient at this season. The differential vortex stretching mechanism, related to wind stress curl gradient (presented in Section III.6) which may act on larger offshore scales, would tend here to be reinforced by the "coastal jet" (Allen, 1973) associated with coastal boundary-scale processes.

There is no evidence of a local cause for the seasonal disappearance of the characteristic closed cyclonic gyral circulation (sometimes referred to as the Southern California Eddy) within the Southern California Bight, which continues to be under the influence of strong cyclonic wind stress curl at this season (Figs. II.4c and II.4d). Rather, it seems most likely that the explanation lies in poleward propagation, as coastal trapped waves (Gill and Clarke, 1974; Allen, 1975), of the effects of the seasonal intensification of equatorward coastal flow off Baja California, which would exert an equatorward "pull" on the coastwise flow within the bight, which at other seasons flows poleward to complete the gyral circulation pattern.

During summer (Fig. III.6c) the gyral circulation within the Southern California Bight reappears. The large scale equatorward flow in the region north of Point Conception intensifies somewhat, corresponding to intensification of the offshore gradient of the wind stress curl which occurs off central and northern California during late spring and early summer (Figs. II.4e and II.4f). There is evidence of a "looping" of the flow toward the coast south of San Francisco, following the similar shape of the wind stress curl gradient (which is particularly evident in Figs. II.4d and II.4f). The flow near the coast of Baja California relaxes from its spring situation, corresponding to the relaxation of the alongshore stress (Fig. II.4f) and

the associated offshore-directed wind stress curl gradient.

By fall (Fig. II.6d), a region of relatively relaxed flow has developed within several hundred km of the coast, with the region of more intense equatorward flow having moved offshore, i.e., in the westwardly direction that would suggest Rossby wave propagation of the intensified equatorward flow that had developed during the earlier portion of the seasonal cycle. Cyclonic eddy development is indicated in the relaxed flow near the coast north of Point Conception, which continues to be under the influence of substantial cyclonic wind stress curl at this season (Fig. II.4a). The gyral circulation within the Southern California Bight, which also continues to be under the influence of cyclonic wind stress curl, is near its seasonal maximum intensity; again the relaxation of intense equatorward flow off Baja California would tend to propagate poleward along the coastal wave guide, to arrive in the Southern California Bight as a relaxation of remotely-forced equatorward flow tendency.

In summary, examination of the seasonal cycles in this area have implicated the differential vortex stretching mechanism, related to horizontal gradient of wind stress curl and associated gradient of Ekman pumping (described in Section III.6), as an important factor controlling the seasonal variation in the ocean surface flow field. There are also some indications that cyclonic wind stress curl

may favor cyclonic eddy development.

III.9 Direction of Rotation of California Current Eddies

Owen (1980) summarized the incidence of eddies of various sizes, from 20 km to over 200 km in diameter, indicated in a 16-year record of CalCOFI surveys. He divided the region covered by the surveys into four segments, arranged in north to south sequence along the coast. He found cyclonic eddies to be substantially more frequent than anticyclonic eddies, by a ratio of about three to two, in three of the regional segments, the two northernmost and the southernmost.

However, in the intervening segment the situation was essentially reversed, with anticyclonic eddies dominating by a very similar ratio. Having defined the characteristic wind stress curl patterns, we now see that this segment, extending from 28° N lat to 31° N lat, corresponds to the location of the lobe of anticyclonic wind stress curl, where anticyclonic wind stress curl dominates both the offshore and near coastal regions.

Thus, we have an indication that cyclonic eddies may form more readily in areas of cyclonic wind stress curl, and vice versa. This constitutes a potential mechanism by which local excesses or deficits in vorticity input by the wind might be stored until the local unbalances could be redistributed to larger scales by advection, lateral

diffusion, transfer to deeper ocean layers via vertical eddy diffusion or vortex stretching, etc.

III.10 Seasonal Cycle: Northwest Africa

Fedoseev (1970) has presented seasonal charts of surface dynamic topography for the region of the Canary Current south of 30°N lat. These are based on on about 2000 hydrographic stations collected in Russian surveys of the region during the period 1957-66. These stations are composited by area (1 by 1 degree, or 1 by 1/2 degree, latitude-longitude quadrangles). Thus there is substantial likelihood of spurious flow features caused by interyear biases in station distributions.

The surface flow pattern during fall (Fig. III.7a) features a strong isolated cyclonic eddy within, and adjacent to, the coastal bight between Cap Blanc and Cap Vert; this corresponds to a rather isolated cyclonic wind stress curl maximum at the same site during this season (Fig. II.5a). A veering of the flow toward the coast inshore of the Canary Islands corresponds to a coastward extension of anticyclonic wind stress curl, suggesting the "gradient of the curl / differential vortex stretching" mechanism. In the offshore region off Cap Blanc, an anti-cyclonic eddy roughly follows the wind curl gradient around a local anticyclonic maximum (Fig. II.5a).

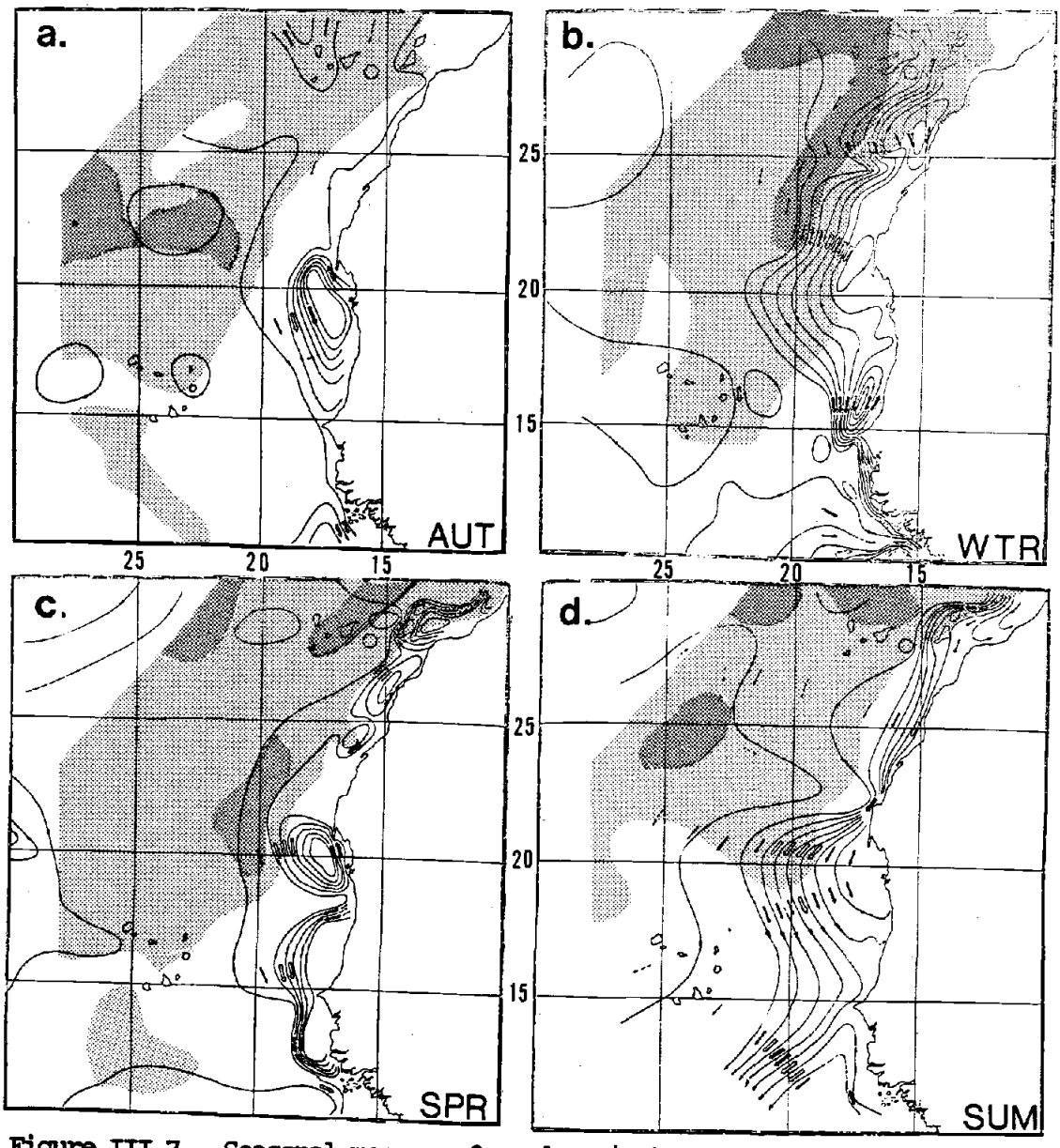

Figure III.7. Seasonal mean surface dynamic topography (after Fedoseev, 1970). To facilitate comparison to the long term mean wind stress curl pattern, areas of anticyclonic curl defined in Fig. II.5 are superimposed via stipled shading; reference to Fig. II.5 is necessary for consideration of important details in regions of cyclonic wind stress curl. **(a)** Autumn; 'Oct-Nov' wind stress curl pattern is superimposed. **(b)** Winter; 'Dec-Jan' wind stress curl pattern is superimposed. **(c)** Spring; 'Apr-May' wind stress curl pattern is superimposed. **(d)** Summer; 'Jun-Jul' wind stress curl pattern is superimposed.

There is a general tendency for dynamic topography contours to have anticyclonic curvature in the regions where the wind stress curl is anticyclonic. Two cyclonic eddies appear in the region of the Cape Verde Islands, within a zone of transition to cyclonic wind stress curl pattern. An anticyclonic current loop in a region of cyclonic wind stress curl, next to the coast at the bottom of Fig. III.7a, does not fit the pattern; however, this feature may be the result, in a situation of seasonally weak wind stress (Fig. II.5a), of coastal trapped wave propagation of equatorward "pull" of the seasonally intensified flow in the Guinea Current (Bakun, 1978), which is situated along this same coast to the southwest.

During winter, the gradient of wind stress curl strengthens normal to the coast (Figs. II.5b and II.5c), and the alongshore flow intensifies dramatically over much of the region (Fig. III.7b). Several cyclonic eddies appear within the region of cyclonic wind stress curl adjacent to the coast. South of Cap Vert a narrow intense coastal current is probably a coastal boundary zone flow (i.e., internal Rossby radius scale baroclinic jet) which is related to the seasonal equatorward alongshore wind stress and amplified by the low value of Coriolis at this low latitude.

During spring (Fig. III.7c), there is a strange feature in the coastal bight between Cap Blanc and Cap

Vert, where an intense geostrophic current appears to flow directly from the coastal boundary, south of the closed cyclonic eddy, and then to flow directly toward the boundary south of Cap Vert. The feature is of a form suggesting flow around a lens of fresh water. In fact, the mouths of the Senegal and Gambia Rivers are located within the area circumscribed by the feature; however, spring is the dry season in this region. It may simply be an artifact of interyear bias in station pattern. In any case there is no corresponding feature in the wind pattern. Eddy-like features near the coast are cyclonic, except for one anticyclonic eddy to the north of Cap Blanc which lies in a location where a lobe of anticyclonic curl appears to approach the coast (contours are not extended to the coast at this location in Fig. II.5d because of paucity of near-coastal data).

During summer strong equatorward alongshore stress characterizes the region from Cap Blanc northward (Fig. II.5e); strong equatorward flow (Fig. III.7d) may represent combined effects of a coastal boundary scale baroclinic jet and a substantial offshore gradient in wind stress curl. South of Cap Vert, the seasonal alongshore stress is poleward, and a northward castal flow corresponds. Off Cap Vert a major current appears to flow southwestward toward the ocean interior; there is nothing in the wind pattern to correspond.

In summary, the indications of possible linkage of flow to wind stress curl pattern are somewhat less than clearcut in these seasonal patterns off West Africa; the possible limitations of these particular composite flow patterns have been mentioned. However, there is definitely no correspondence of equatorward flow maxima to anticyclonic wind stress curl maxima as would be the case if local Sverdrup balance were exerting major control on the surface flow pattern. Rather, flow maxima, which are seaward of the internal Rossby radius scale, tend to correspond to regions of strong horizontal gradient of wind stress curl and to be directed in the correct sense for the differential vortex stretching mechanism discussed in Section III.6. Also, the tendency for flow curvatures and eddies to be characterized by curl having the same sense as the overlying wind stress pattern has been noted in this region as in the California Current region.

III.11 The Benguela Current Region

Shannon (1985) has presented a composite diagram of surface flow pattern in the Benguela Current (Fig. III.8). Here again we find no correspondence of meridional flow maxima to wind stress curl maxima to suggest any requirement for local Sverdrup balance in the surface flow field. Rather, the core of the current generally corresponds to the region of substantial horizontal gradient of wind

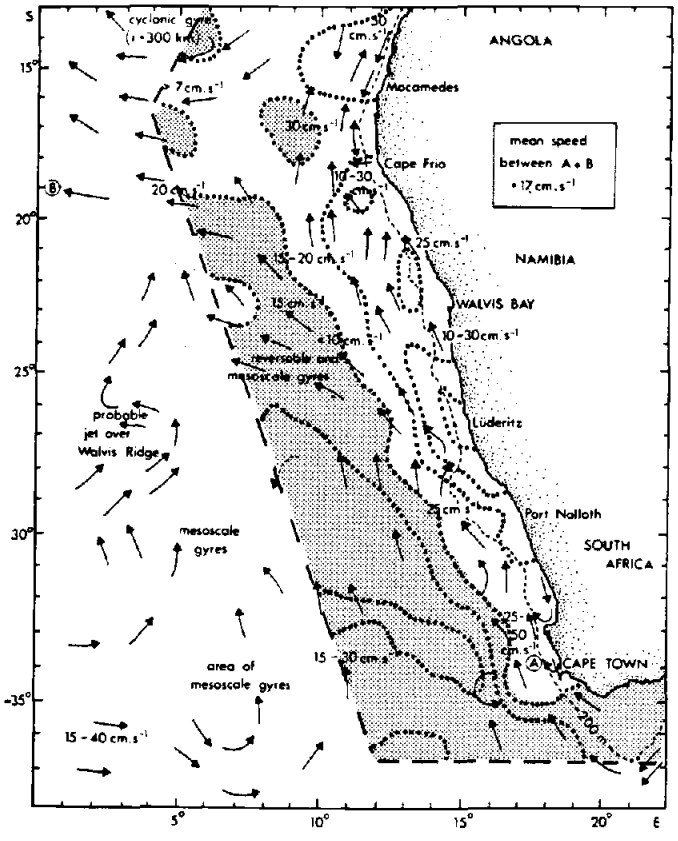

Figure III.8. Composite diagram of Benguela Current surface flow pattern (after Shannon, 1985). Much of the detail comes from data taken during austral summer, and so the 'Dec-Jan' wind stress curl distribution (Fig. II.6e) is superimposed (via dotted contours and stippled shading) for comparison.

stress curl. Note, for example, the suggestion of flow curvature around the small area of persistent anti-cyclonic wind stress curl situated offshore of Cape Frio.

Nelson and Hutchings (1983) report the existence of a relatively permanent cyclonic circulation over the continental shelf and slope regions between Cape Frio and a point just to the south of Luderitz; the distributions of Fig. II.6 show the overlying wind stress pattern to be particularly strongly cyclonic over the same area. Stander (1964) showed many instances of cyclonic eddies in the region between 20° S and 25° S lat.

III.12 The Peru-Humboldt Current Region

Example distributions of surface dynamic topography for the region off western South America have been presented by Wyrtki (1963) and by Sandoval (1971). Sandoval's data are from several cruises during the period 1960-69; he considers his distributions to represent summer (i.e., January, February, March) conditions (Fig. III.9a). Wyrtki's data are from a single cruise undertaken from September through December, 1960 (Fig. III.9b). In both cases the dynamic height contours are drawn through rather sparse and sporadic station distributions, and so the details of the inferred flow patterns are highly dependent on station patterns. As in the other regions, one sees no pattern of correspondence of meridional flow maxima to curl maxima

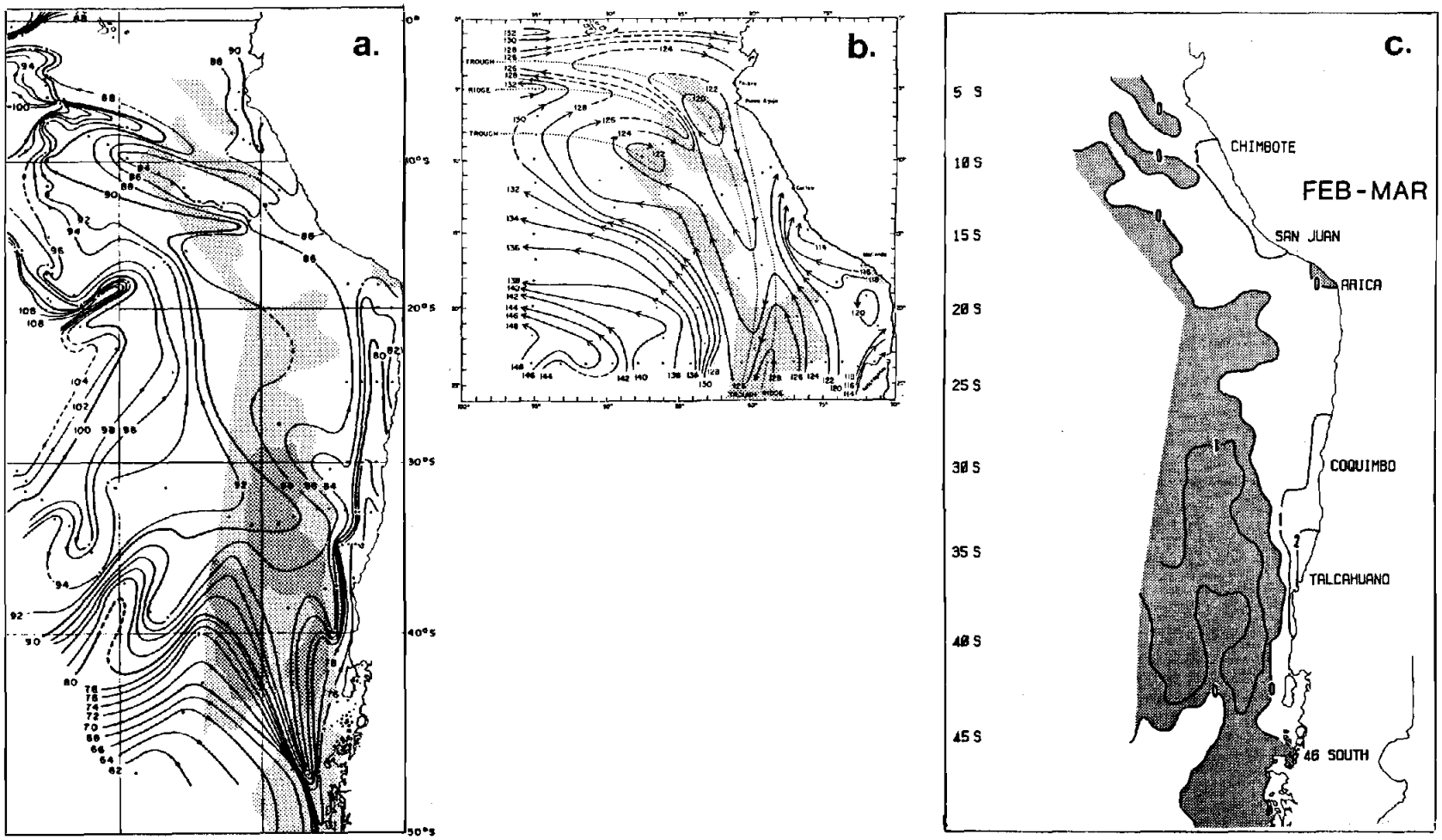

Figure III.9. Surface dynamic topographies (dyn. cm). **(a)** Figure presented by Sandoval (1971); contoured values are relative to 500 db. **(b)** Figure presented by Wyrtki (1965); values are relative to 1000db. **(c)** 'Feb-Mar' wind stress curl distribution (from Fig. II.7f). To facilitate comparison, patterns from panel (c) are superimposed on panels (a) and (b) via stippled shading.

that would implicate Sverdrup balance as exerting a major control on the surface flow pattern. Rather, the pattern is suggestive of the "gradient of the curl / differential vortex stretching" mechanism. For example, in Sandoval's figure (Fig. III.9a), the shape of the flow pattern near the Chilean coast corresponds well to the shape of the contours of the overlying wind stress curl pattern (Figs. II.7, III.1, III.9c), particularly with respect to features that are consistent among consecutive bimonthly seasonal segments.

Within the coastal bight near Arica, Sandoval's distribution (Fig. III.9a) exhibits a cyclonic curvature to the flow pattern, as if the flow were following the "zero" wind stress curl contour around the small anticyclonic area, situated against the coast immediately north of Arica, indicated in the February-March distribution (Fig. III.9c). Wyrtki's distribution, on the other hand, shows a closed anticyclonic eddy. This feature apparently could equally well have been drawn as a coastward loop of the 120 dynamic cm contour, which is drawn as a separate contour offshore with no indication of a station which could define a local dynamic height minimum between. Such a loop would correspond quite well to the local wind stress curl contours indicated in the August-September distribution (Fig. II.7c).

Similarly, Wyrtki has drawn the rather complex flow pattern near 10° S lat as featuring two separate closed cyclonic eddies. Apparently, he could equally well have drawn the 122 dyn. cm contour as being continuous between the two. In that case, the elongate cyclonic feature indicated by Sandoval would also be shown in Wyrtki's figure. Likewise, there are no stations indicated near 7° S lat, 82° W long in Sandoval's figure that could define the local dynamic height minima indicated by Wyrtki. The point here is that it is difficult to be precise about the flow details, but the alternation of elongate wind stress curl features overlying similarly oriented elongate flow features is suggestive of a linkage through differential vortex stretching.

As another example, the curved flow pattern along the coast from about 17° S lat to 11° S, which appears in Wyrtki's figure but not in Sandoval's due to lack of stations in the area, has a similar shape to the contours around the coastal cyclonic wind stress curl region existing near the southern coast of Peru during austral spring and summer (Figs. II.7d and II.7a). A tendency for the flow contours to swing somewhat offshore from the location of the wind stress curl contours might be interpreted variously as (1) inadequate definition by the available station pattern, (2) lateral diffusion of the wind-induced ocean surface vorticity input by the wind, or (3) evidence of

westward Rossby wave propagation.

III.13 Tropical Thermal Domes

Mazeika (1967) described sharp seasonal doming of near-surface isotherms, during the summer seasons in the respective hemispheres, at two locations in the tropical eastern Atlantic. He referred to the feature near 10°N lat as the Guinea Dome (Fig.3.10a) and to the feature near 10°S lat as the Angola Dome (Fig. 3.10b), and cited their similarity to the corresponding feature in the eastern tropical North Pacific known as the Costa Rica Dome (Wyrtki, 1964).

Hofmann, Busalacchi, and O'Brien (1981) suggested that the Costa Rica Dome is a result of Ekman pumping by cyclonic wind stress curl associated with the Intertropical Convergence Zone (ITCZ), and presented a numerical model simulation showing release of the feature as a propagating Rossby wave following seasonal relaxation of the local curl of the wind stress. Hofmann et al. also suggested the Guinea Dome feature in the Atlantic as having a similar origin and cited the wind stress curl maps of Hastenrath and Lamb (1977) discussed above in Section II.1.

The wind stress curl distributions reported herein encompass the Guinea and Angola Dome areas. To investigate the mechanisms, the original unfiltered two-monthly wind stress curl values at the individual one-degree grid

intersections were summed and averaged over the shaded quadrangles 'G' and 'A', indicated in Figs. III.10a and III.10b. The resulting seasonal cycles are graphed in Fig. III.11.

The seasonal cycle of wind stress curl in area 'G', overlying the Guinea Dome, does match the hypothesis that upward Ekman pumping in response to cylonic wind stress curl may control the seasonal appearance of the dome structure. However, in the case of area 'A', which overlies the Angola Dome, this does not appear to be the case. Rather than relaxing during the winter, when the Angola Dome structure disappears, the cyclonic wind stress curl in fact reaches its seasonal peak. Thus the seasonal variation in the Angola Dome structure appears to be directly out of phase with the seasonal variation in Ekman pumping. Admittedly, the observational base in the area is very sparse. However, examination of corresponding calculations from separate August and September samples show independent similar indications of seasonal peaking of cyclonic wind stress curl during those months.

Thus we have a discrepancy to the pattern reported by Hoffman et al. (1981). Accordingly, the comparative method leads us to question the validity of the hypothesis, until reasons for the discrepancy can be advanced which can allow conformity of the various examples to a consistent generalization (Bakun, 1985).

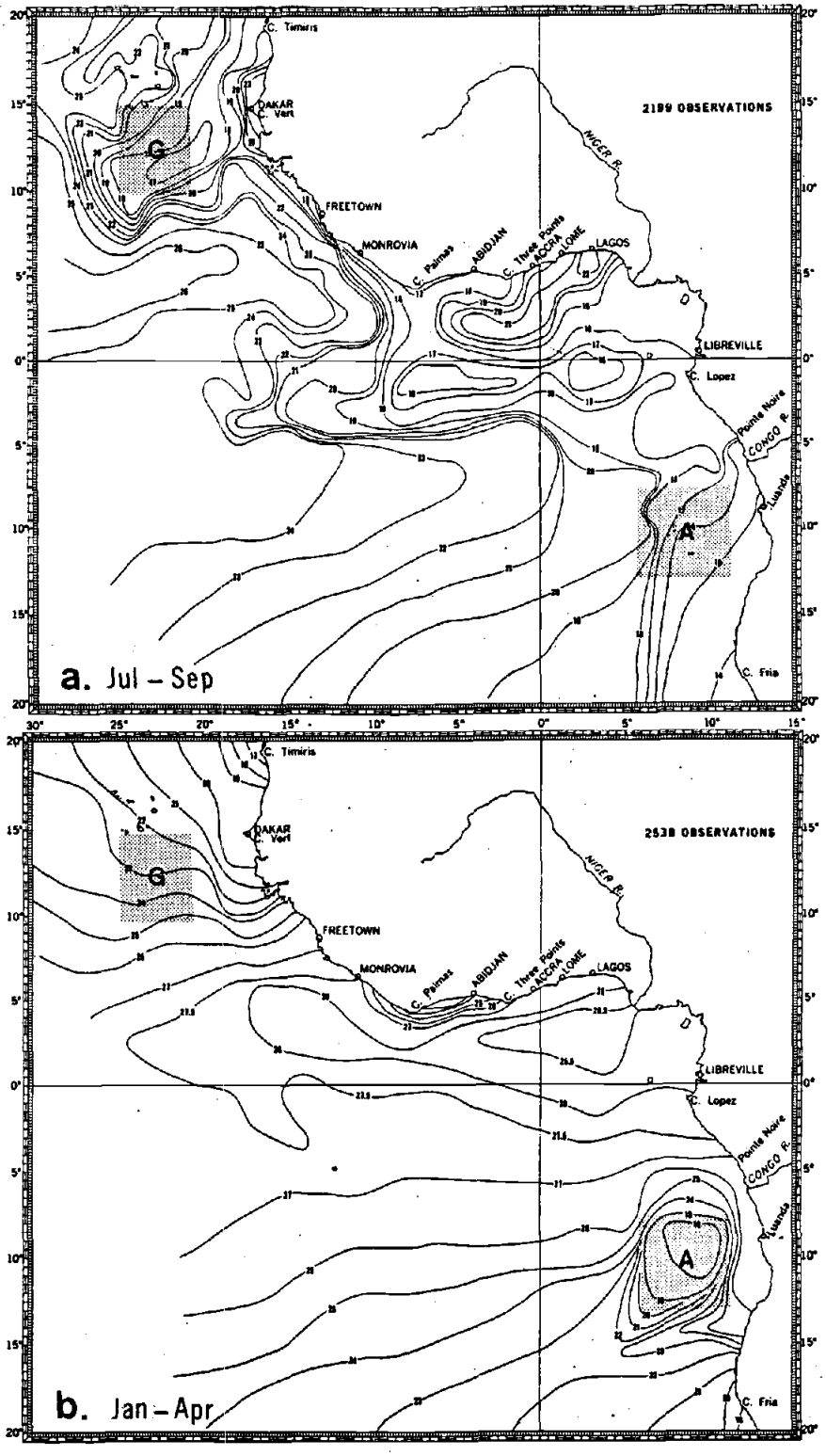

Figure III.10. Temperature distributions presented by Mazeika (1967), **(a)** at 20 m during Jul-Sep; **(b)** at 50 m during Jan-Apr. (Stippled areas 'G' and 'A' indicate areas used to characterize seasonal variation of wind stress curl over the respective Guinea and Angola Dome areas.)

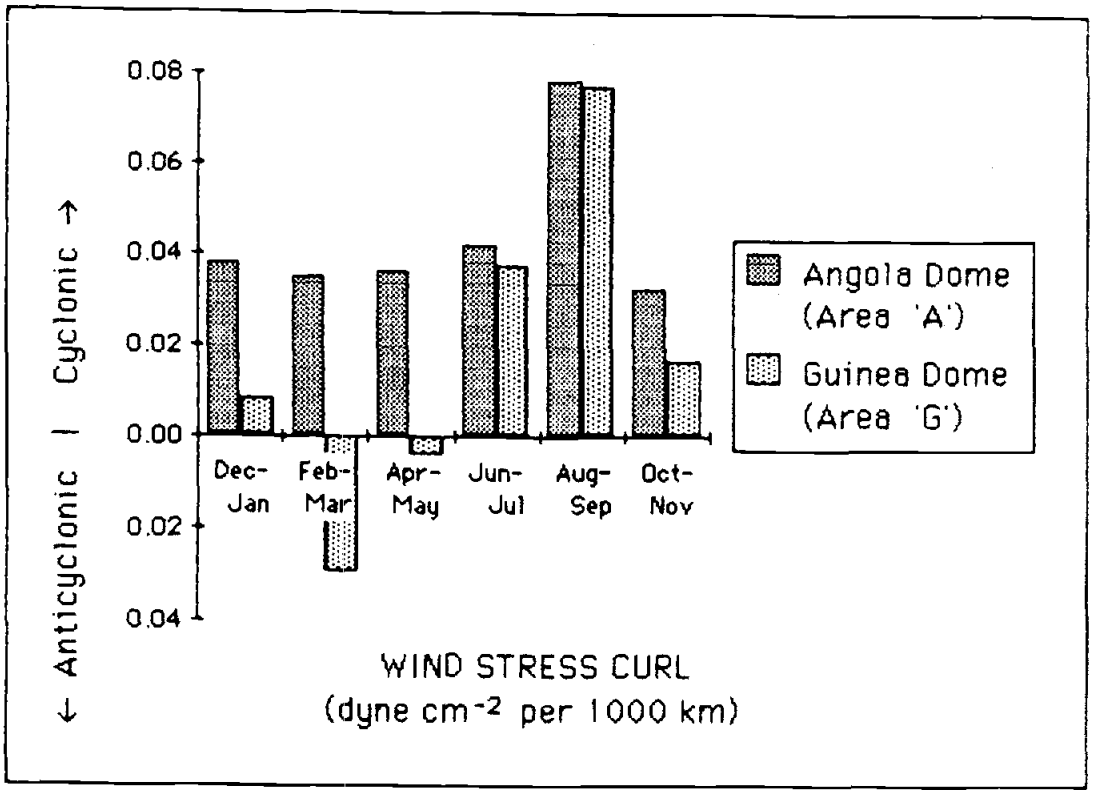

Figure III.11. Characteristic seasonal variation of wind stress curl over the Guinea Dome and Angola Dome areas (areas 'G' and 'A', respectively, shown in Fig. III.10).

Indeed, there are additional reasons to question the hypothesis. Note that the value of the Coriolis parameter at 10° lat is about one third that at 30° lat. Thus equal rates of Ekman pumping would occur at 10° and 30° lat if the wind stress curl at the higher latitude were three times larger. However, characteristic wind stress curl values at higher latitudes (Figs. II.4, II.5, II.6, II.7, etc.) are generally an order of magnitude greater than those indicated (in Fig. III.11) in the tropical dome areas. Thus one would need to explain the lack of even more striking doming features in other regions of much stronger apparent Ekman pumping.

Finally, one might question the lack of correspondence of the shapes of the dome structures to the shapes of the wind stress curl features, if simple Ekman pumping is to be considered the dominant formative mechanism. In the case of the Guinea Dome, the strongest cyclonic wind stress curl in the offshore region lies well to the west of the Cape Verde Islands (Figs. II.5e and II.5f) rather than near the dome feature.

In conclusion, this application of the comparative method leads to doubts concerning the suggestion of Hofmann et al. (1981) that the dynamics of tropical eastern ocean thermal dome features are controlled primarily by the local wind stress curl through the mechanism of direct local Ekman pumping. It appears necessary to ascribe major

effects to other mechanisms, i.e., the earlier suggested confluence of equatorial and eastern boundary current systems (Wyrtki, 1964), etc.

III.14 Summary

The comparison of seasonal and long term mean aspects of vorticity input by the wind, in four major eastern boundary current regions, to available information on ocean flow characteristics has yielded certain interesting patterns of correspondence that may provide useful insights into the mechanistic linkages involved.

We find that cyclonic wind stress curl consistently tends to overlie the locations of eastern boundary poleward undercurrents. In addition, the width of the undercurrent appears to vary with the width of the coastal band of cyclonic wind stress curl. The patterns observed are such as to be not inconsistent with an assumption of depth-integrated Sverdrup balance in the localities of the undercurrents, although possible effects of flow interactions with slopes of the ocean floor raise serious questions with respect to such an assumption.

We find no pattern of correspondence of surface maxima in meridional ocean flow to wind stress curl maxima that would indicate a control on the surface flow pattern by a requirement for some substantial degree of local Sverdrup balance within the upper layer of the ocean. Rather, a

pattern of correspondence of ocean surface flow (seaward of the internal Rossby radius-scale coastal boundary zone) to the horizontal gradient of wind stress curl, has implicated a mechanism of differential vortex stretching as constituting a major determinant of the surface geostrophic flow pattern.

We find a tendency for curvatures in the large scale ocean surface flow field, and for baroclinic eddies of a range of sizes, to have the same rotational sense as the overlying wind stress curl pattern. The significance of this tendency may be to accommodate local excesses and deficits of vorticity input by the wind, as a step in the process of redistribution to larger scales (by processes of eddy diffusion, advection, etc.) where they may be brought into larger scale balance with planetary vorticity advection (i.e., Sverdrup balance), frictional dissipation, or oppositely-directed vorticity inputs due to wind stress curl at other locations or seasons.

A discrepancy to the pattern of correspondence of seasonal variations in the major eastern ocean boundary tropical thermal domes to the local seasonal cycles of wind stress curl leads to doubt concerning the hypothesis that the appearance of these dome features is primarily regulated by local Ekman pumping. This skepticism is bolstered by (1) rather low characteristic values of wind stress curl in the dome areas, even when the effect of

latitudinally-varying Coriolis on the rate of Ekman pumping is take into account, compared to other areas where such sharp displacements of the subsurface thermal structure are not found, and by (2) a lack of similarity in general shape of the dome features and the overlying wind stress curl pattern.

III.15 Concluding Remarks

The unique situation off north-central Baja California

The area off north-central Baja California has herein offered a particularly illuminating example, being under the influence of a persistent lobe of anticyclonic wind stress curl extending coastward to the coastal boundary zone. This differs markedly from the common subtropical eastern ocean boundary situation which is characterized by (often intense) cyclonic wind stress curl within several hundred km of the coast. The area immediately to the north, the Southern California Bight region, offers a prime example of this more common situation. The proximity of these contrasting situations has offered revealing contrasts.

For example, the striking conformity of the surface flow pattern to the general shape of the the wind stress curl feature (see Section III.8) offers perhaps the most convincing example discussed herein of the apparent action of the "gradient of the curl / differential vortex stretch-

ing" mechanism (discussed in Section III.6). The area has also been particularly revealing in the discussion of poleward undercurrents (Section III.4) and in motivating an hypothesis that there is a tendency for the direction of rotation of eastern boundary current baroclinic eddies to be in the same sense as the overlying wind stress curl pattern (see Section III.10).

The geophysical explanation for this unique wind stress curl feature is not clear at this time. Perhaps the existence of the Gulf of California, directly to the east and several times wider than the Baja California Penninsula (which at this location has substantially lower topographic relief than occurs in the coastal range immediately to the north), results in certain aspects of the atmospheric continental boundary being offset somewhat to the east of the oceanic continental boundary. In other eastern boundary regions the effective atmospheric and oceanic continental boundaries might tend to coincide. In such a case, the situation perhaps offers a unique opportunity to distingush between real mechanistic linkages of wind to ocean boundary current flow dynamics and mere correspondence of effects occurring similarly and independently in the oceanic and atmospheric fluid flows due to similar proximity to the lateral continental boundary. In view of this, there might be particular scientific value in locating process-oriented oceanographic studies, such as have been undertaken in

various other eastern boundary current regions, in the area off north-central Baja California.

The question of depth-integrated Sverdrup balance

The comparisons presented herein have yielded no evidence for a tendency of the surface flow field toward Sverdrup balance with the overlying wind stress curl field, except perhaps on the largest spatial scales (i.e., the scale of the Subtropical Gyres). However, the results of the examination of available information on eastern boundary poleward undercurrents have not been inconsistent with the possibility of depth-integrated Sverdrup balance.

We have noted that characteristic meridional flow velocities, even in these relatively sluggish eastern boundary currents, are sufficient to yield planetary vorticity advection, within a relatively thin layer within 100 to 300 m of the sea surface, which would have a similar magnitude to the characteristic wind stress curl input. Thus, since no pattern of direction of the surface current is found to indicate a direct linkage, except on the very large (Subtropical Gyral) scale, the flow at deeper layers must essentially cancel the pattern at the surface for depth-integrated Sverdrup balance to occur on smaller local scales. Thus, it would be interesting to look for examples of "mirror images" of surface flow patterns, in deep subsurface flow patterns. The spatial scales on which such mirror immages are evident may indicate the scales on which

depth-integrated local Sverdrup balance is actually acting in the real ocean.

IV. TIME SERIES BASED ON AREAL COMPOSITES OF MARITIME DATA OFF THE IBERIAN PENINSULA

IV.1 Introduction

In this chapter we switch our focus from interregional comparative analysis to time series analysis. In the previous chapters we have attempted to derive insights by resolving and recognizing patterns of correspondence among seasonal and geographical features. In turning our attention to time series, our concentration shifts from the normal to the anomalous: i.e., from cyclic, predictable, intra-year features to presently unpredictable interyear features. Our comparative methodology switches from spatial to temporal reference, from comparison between different regions to comparison between different years.

We examine the capacity of maritime data to provide indications of interyear variability in wind stress curl. We then use wind stress curl time series, along with maritime data-based estimates of nonseasonal variability in sea surface temperature, wind stress, wind-induced turbulent mixing, and atmosphere-ocean heat exchange, to model the nonseasonal variability of coastal sea level and of the evolution of sea surface temperature in 5-degree latitude/longitude quadrangles off the Iberian Peninsula (Fig. IV.1). The time series examined consist of monthly

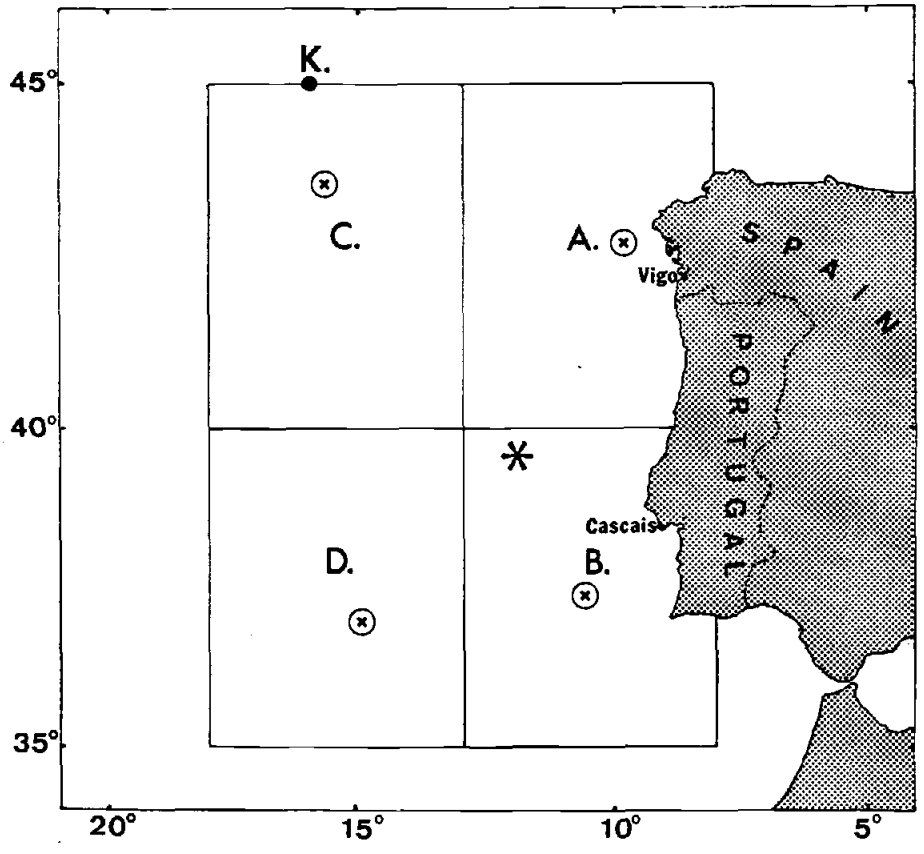

Figure IV.1. Locations of 5-degree latitude/longitude quadrangles (areas labelled 'A', 'B', 'C', and 'D') used to summarized maritime reports to produce monthly time series. The mean latitude and longitude of reports available within each of these areas, over the period 1948 to 1979, is marked by the "x" symbols surrounded by small circles. The mean latitude and longitude of the reports from all four areas together (i.e., from the entire 10-degree quadrangle) is marked by the large asterisk. The location of Ocean Weather Station K is indicated by the large dot on the northern boundary of area 'C', below the label 'K'. The locations of the coastal sea level stations at Vigo and Cascais are indicated by the small dots to the right of the names.

estimates over a 32-year period, 1948-79.

IV.2 The 12th-difference Transform

The dominance of the seasonal cycle, among the various components of temporal variability, was useful to the analyses presented in the previous two chapters in providing a rationale for compositing data from a large number of years to yield finer spatial resolution than ever available from synoptic sampling of maritime reports. In the present case the dominance of the seasonal variation presents problems; the large-amplitude seasonal variability introduces large autocorrelation in "raw" data series (e.g., Fig. IV.2, upper panel), which reduces the real degrees of freedom available for statistical analysis. Also, since a strong seasonal cycle is a feature of nearly all oceanic and atmospheric data, causally-interrelated or not, it must be filtered to avoid either presenting a misleading indication of causal relationship where none may exist, or obscuring evidence of a real causal relationship where a fortuitous correlation in seasonal features is out of phase with that representing the causal linkage.

In graphical presentations of long time series of monthly data, it is helpful to suppress large-amplitude shorter-scale variability to make it easier to visually follow a much less numerous set of longer period variations. Thus most of the graphical time series plots

presented herein have been subjected to a simple 12-month running mean filter which suppresses the short scale variability and removes the seasonal cycle (e.g., Fig. IV.2, middle panel).

However, the severe suppression of shorter-scale nonseasonal variability imposed by the 12-month running mean filter is undesirable in most of the statistical tests performed. This is because shorter scale variations provide many more independent degrees of freedom for empirically investigating causal linkages than do the longer scale variations. One way to suppress seasonal variability is by transforming a monthly time series to a series of monthly "anomalies" by subtracting a long term mean value for the given calendar month from each value in the time series. An alternate way to remove seasonal variation and also to remove certain other sources of serial correlation in a time series, is by transforming the series to "12th-differences" by subtracting from each monthly value the value for the same calendar month of the previous year (e.g., Fig. IV.2, bottom panel). The 12th-difference transform is commonly used to remove seasonal nonstationarities from time series inputs to statistical forecast models (e.g., see the discussion of the "seasonal operator" by Bowerman and O'Connell, 1977, page 400). To provide an illustration of the effect of these transformations, consider the following hypothetical example involving two time series

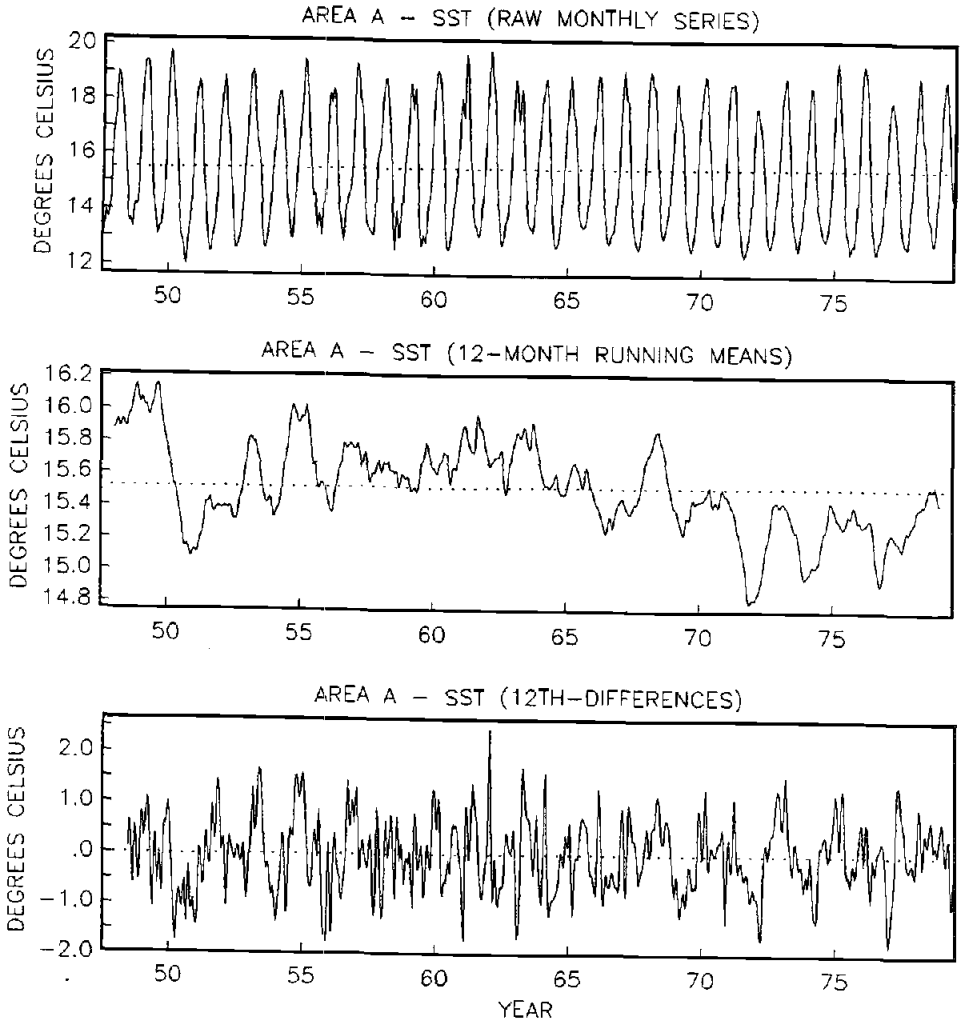

Figure IV.2. Sea surface temperature in area 'A'. Units are degrees Celsius. *Upper panel:* Raw monthly time series. *Middle panel:* 12-month running means. *Bottom panel:* 12th-differenced monthly time series.

of monthly values over the 10-year period, 1971-80. One series consists of monthly landings of a fish species caught only during three months of the year. Let us suppose that all the monthly landings during those three calendar months were identical up to 1975, after which the landings were zero (i.e., the square symbols connected by a solid line in the upper panel of Fig. IV.3). The second time series consists of monthly mean sea levels at a local tide gauge; assume that the sea level undergoes a regular seasonal cycle which is superimposed on a linear downward trend due to very long period coastal uplift associated with interglacial rebound (triangle symbols in Fig. IV.3).

Now assume that we wish to empirically test whether the fish population collapse was related to natural environmental variation (as opposed to overfishing, for example). Sea level is a commonly-used environmental variable for such studies, being a sensitive indicator of various processes in the coastal marine environment (Bakun and Parrish, 1980). In our hypothetical example, there is of course no real relationship because the sea level trend is due to upward movement of the tide gauge which is attached to the rising coastline, rather than to fall of sea level height due to ocean processes.

The raw series (upper panel of Fig. IV.3) are highly correlated (r=.57). If we assume independent degrees of freedom for each of the 120 data points, the indicated

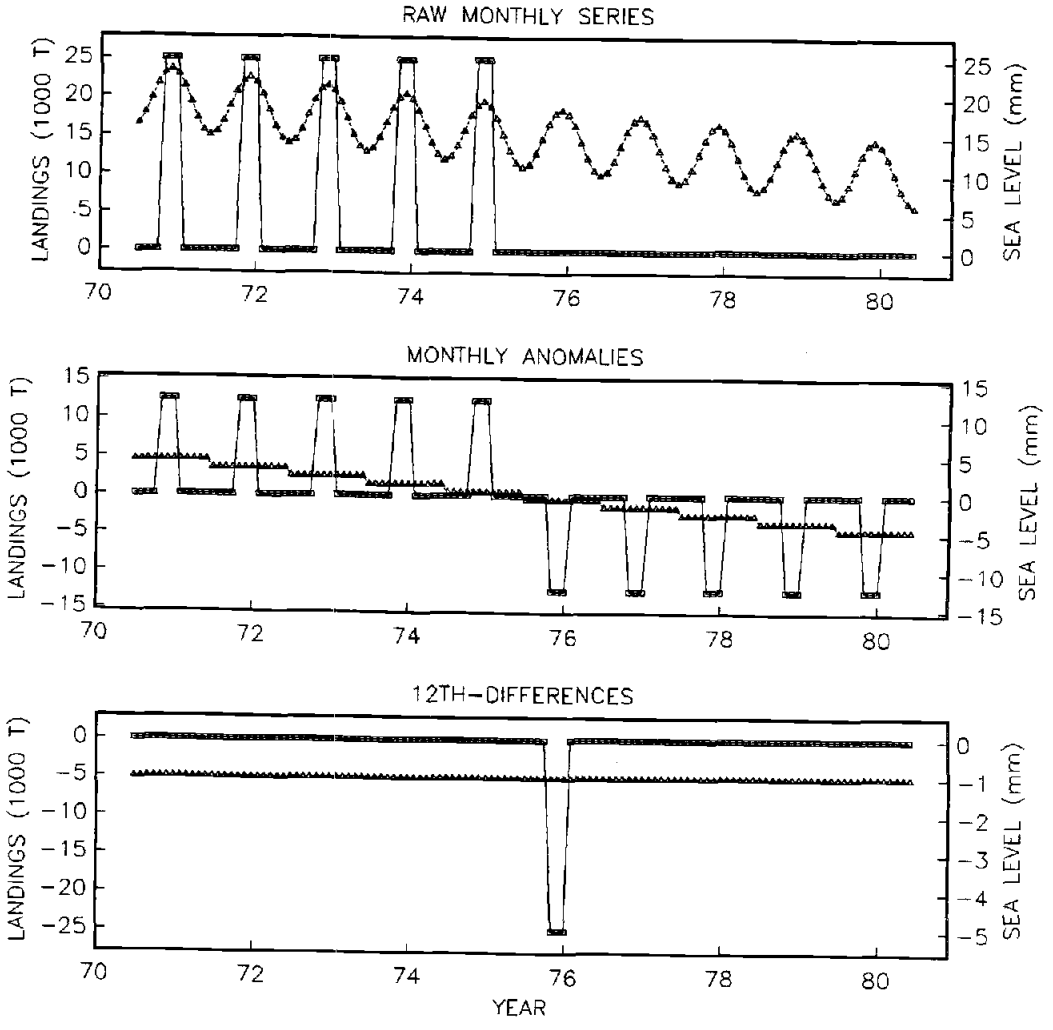

Figure IV.3. Hypothetical monthly series of landings of a fish stock (square symbols) and of coastal sea level (triangle symbols) . *Upper panel:* Raw monthly time series. *Middle panel:* monthly anomaly time series. *Bottom panel:* 12th-differenced monthly time series.

significance of this relationship is very high ($p << .001$). This illustrates the artificial amplification of significance that can occur when the series tested contain substantial autocorrelation associated with seasonal cycles and long term trends.

If both series are transformed to monthly anomalies (middle panel of Fig. IV.3) the correlation between them drops ($r=.42$) due to suppression of the seasonality in sea level. However, the correlation still is highly significant ($p << .001$) due to the fact that this transformation does not remove autocorrelation at interannual frequencies. Note also the seasonal oscillations introduced into the latter half the anomaly series of fish landings, where there were none in the raw series. The anomaly transformation represents a "non-local" filter, i.e., each value in the transformed series depends on values in distant parts of the time series; when the period for determining long term monthly means changes, the anomaly values change throughout the series. And as illustrated in our hypothetical example, long term variations in the seasonal cycle may introduce artificial features at the seasonal frequency.

If both raw series are subjected to the 12th-difference transform the correlation disappears altogether ($r=0.00$). The result (Fig. IV.3, lower panel) reflects the "true" situation in our example. The sea level series is

featureless and the fish landing series shows only one "event", the collapse of the population. And of course that is all the "real" information contained in the example.

The 12th-difference transform removes seasonalities by expressing year to year change at a particular segment of the seasonal cycle. The procedure also removes long term linear trends, and constitutes a "local" filter, where values of the transformed series depend only on time series values within the immediately adjacent year. Thus the seasonal cycle may be effectively filtered even when the seasonal cycle itself is undergoing longer period variation within the time series. The result is a series relatively free of the serial correlation which otherwise tends to severely diminish the power of empirical tests. The 12th-difference transform has the property that a 12th-differenced series of monthly anomalies is identical to the corresponding 12th-differenced series of raw monthly values.

Because of these properties, 12th-differencing offers an intuitively clear and procedurally simple method to remove much of the autocorrelation that would interfere with empirical tests for causal linkages between monthly geophysical time series. Prior application of the 12th-difference transform to all data series has been adopted as standard procedure in the various regression models and correlation tests discussed in this and the

following chapter; unless specifically stated otherwise, any time a correlation coefficient or significance level is cited in Chapters IV and V, it may be assumed they refer to 12th-differenced series.

IV.3 Time Series of Wind Stress Curl

In the previous two chapters, the data coverage required for the fine spatial resolution achieved was amassed by incorporating data from a large number of years to define a composite seasonal cycle. A next step is to attempt to produce time series of wind stress curl in which the data base is divided up into a much larger set of monthly values for individual years. This results in incorporation of far fewer data in each temporal increment, and so spatial resolution is degraded.

One way this has been accomplished in the past has been to use analyzed fields of wind or barometric pressure, routinely produced by meteorological agencies as part of their weather forcasting procedures, as a basis for the computation. The fields are customarily arranged on a spatially-continuous grid system, and so once the field has been converted to a field of estimated stress exerted by the wind on the sea surface, computation of the curl is straightforward. This methodology was initially developed and employed by Fofonoff (e.g., Fofonoff and Froese, 1960; Fofonoff, 1962) for routine computation of quite large

scale (alternate 5-degree data grid) monthly wind stress curl estimates; annual updates of these computations have been published by Fofonoff, Wickett, and others in the Fish. Res. Bd. of Canada Manuscript Report Series. Time series of monthly wind stress curl estimates, computed on a finer 3-degree grid basis, have been reported by Bakun and Nelson (1977).

A problem arises in estimating precision of the indicated variations in time series computed in this manner because independent replicates are not available and the analysis procedures impose large scale spatial continuity on the data fields which prevents use of spatially-adjacent estimates as related independent samples of temporal variability.

In this chapter, we examine wind stress curl time series produced from simple areal samples of reports. Restricting the data samples to specifically bounded areal regions provides independence of adjacent samples allowing a degree of independent replication (of temporal variability occurring on larger spatial scales) so as to fairly judge our capacity to discern real interyear variability in the curl of the wind stress acting on the sea surface.

The 10-degree latitude/longitude quadrangular ocean area adjacent to the west coast of the Iberian Peninsula (Fig. IV.1), chosen for the study, is an eastern boundary

current region having particularly dense maritime data coverage (see Fig. II.3). It is typical of such regions in the oceanographic sense, featuring a coastal upwelling system (Wooster et al., 1976), etc. The area was divided into four 5-degree areal segments, indicated by the letter designations 'A', 'B', 'C', and 'D'. In addition, Ocean Weather Station 'K' is situated directly on the northern boundary of area 'C'. Strict independence of the reports sampled within area 'C', from the reports from OWS-K, was ensured by rejecting any report which reported a position which was within a tenth of a degree of the nominal position of OWS-K, from the 'C' sample. Five independent time series of monthly samples of maritime reports are thereby obtained; the 32-year period, 1948 through 1979 was chosen as having relatively abundant data in the version of the surface marine data file (National Climatic Center File TDF-11) to which I had access. The series for areas 'A', 'B', 'C', and 'D' are continuous over the period. The series for OWS-K runs from July, 1949 to December, 1968, with a short data gap from April through December, 1958. Numbers of observations in the monthly samples within the various series are quite variable (Tables IV.1 to IV.5). It was not possible to restrict the various series to periods containing large numbers of reports without losing major portions of the available time series. Thus the time series constructed are quite variable with respect to underlying

data base and associated significance of the derived monthly estimates.

From each wind report an estimate of the sea surface stress was produced according to Eq. 2.3. The constant drag coefficient formulation employed in Chapter II has been employed in a number of previous climatological studies of upwelling regions (e.g., Bakun, McLain and Mayo, 1974; Nelson, 1977; Parrish et al., 1983). Estimates based on this formulation are the primary basis for the results reported below. However it is recognized that the value of the drag coefficient is actually a variable which depends on the nature of the atmospheric turbulence near the sea surface. Thus a dependence on both atmospheric stability and wind magnitude near the sea surface is indicated. No clear consensus as to a best formulation of these dependencies is presently available.

However, in order to provide a gauge of the effect on our conclusions of uncertainties about the most appropriate drag coefficient, a reasonable drag coefficient formulation has been chosen and applied to produce a companion set of stress estimates, to be displayed along with the constant coefficient series in the various graphical presentations For this purpose we follow the method of Nelson (1977), which is based on a bulk Richardson number formulation (Deardorff, 1968), for incorporating the atmospheric stability effect. We differ from Nelson in the manner of

Table IV.1. Numbers of reports in each monthly sample within area "A".

YEAR	Jan	Feb	Mar	Apr	May	Jun	Jul	Aug	Sep	Oct	Nov	Dec
1948	233	272	258	265	262	251	266	242	241	268	205	215
1949	258	229	250	254	263	230	229	222	194	234	255	240
1950	231	196	252	242	273	193	244	232	181	219	187	203
1951	167	174	149	139	121	168	158	173	161	170	174	187
1952	169	186	159	162	139	107	173	209	179	215	203	251
1953	221	225	215	231	253	206	195	186	206	246	222	289
1954	239	219	213	252	236	229	184	210	233	264	204	245
1955	220	200	251	195	227	151	180	88	118	97	90	28
1956	27	34	40	43	26	29	25	23	26	21	28	18
1957	23	36	37	25	27	23	13	16	26	29	20	29
1958	33	22	17	14	12	39	35	27	17	30	15	34
1959	29	25	34	18	14	7	19	7	11	24	21	35
1960	31	41	17	32	24	19	41	24	22	19	21	26
1961	50	36	16	22	20	28	25	11	36	47	44	44
1962	55	44	33	29	28	17	31	43	33	34	8	40
1963	29	36	8	19	21	23	27	11	27	30	33	17
1964	1087	1001	1134	1010	1052	1014	934	968	990	1066	1016	913
1965	1246	1027	1204	1098	1280	1020	1181	1230	1202	1292	1151	1093
1966	995	908	1027	1066	1103	722	967	867	811	870	806	845
1967	960	857	1051	1071	1004	809	872	866	802	860	851	876
1968	1019	1024	1049	1013	977	815	969	826	884	1079	953	1013
1969	1085	1024	1191	1082	1082	931	912	907	857	876	983	972
1970	787	857	1032	1037	935	872	855	871	855	920	798	831
1971	114	193	387	312	294	249	730	1084	906	986	1003	920
1972	975	887	1075	966	1003	977	910	827	978	892	785	881
1973	984	876	987	1088	887	868	859	804	837	722	644	697
1974	592	625	646	565	639	265	335	639	439	703	791	627
1975	716	790	1017	786	917	932	940	881	1000	1056	1034	985
1976	871	924	1030	1035	1095	964	850	829	818	981	1022	879
1977	892	787	883	840	866	702	853	770	669	909	755	744
1978	802	801	832	880	746	699	690	650	632	618	601	861
1979	812	869	913	744	931	885	708	740	782	828	779	719

Table IV.2. Numbers of reports in each monthly sample within area "B".

YEAR	Jan	Feb	Mar	Apr	May	Jun	Jul	Aug	Sep	Oct	Nov	Dec
1948	206	280	226	251	261	266	261	253	243	256	209	200
1949	266	257	311	274	339	315	263	284	237	242	253	254
1950	270	229	273	265	368	245	302	260	221	263	237	261
1951	272	240	229	183	219	218	223	230	193	230	239	229
1952	239	229	246	269	238	235	261	217	271	295	269	297
1953	302	268	304	271	301	272	248	246	228	291	322	331
1954	300	275	246	273	310	321	293	243	371	284	258	280
1955	250	258	298	264	431	261	245	184	194	227	164	114
1956	113	110	135	128	164	149	168	114	137	117	102	75
1957	91	82	115	112	156	165	163	116	131	173	151	124
1958	109	120	118	127	141	187	138	119	114	112	97	100
1959	112	131	129	98	111	133	137	151	85	111	145	133
1960	138	167	85	122	158	143	163	174	127	188	158	148
1961	133	175	156	171	178	166	142	161	159	137	120	124
1962	164	125	131	174	160	145	137	172	121	141	138	130
1963	161	135	149	147	148	141	146	126	148	134	145	126
1964	1011	921	1123	1015	1057	1014	1119	946	988	1109	1078	940
1965	1136	938	1162	1135	1236	1090	1178	1135	1147	1206	1080	981
1966	1026	846	1067	1040	1032	776	1064	910	793	942	789	823
1967	949	1008	987	1070	1009	818	909	893	851	937	886	881
1968	1006	1084	1071	1061	1002	879	1044	968	997	1185	1039	1081
1969	1052	1158	1170	1250	1165	1091	1044	1040	935	1019	1104	1090
1970	784	888	1209	1104	1071	1100	989	974	955	1068	981	890
1971	122	232	453	336	375	241	209	1201	999	1059	1042	981
1972	1030	888	1061	1146	1010	1007	936	885	1001	962	857	950
1973	995	978	973	1039	948	1029	1011	927	978	798	705	715
1974	598	580	672	594	702	344	375	688	441	706	748	731
1975	733	792	1010	864	924	1040	1029	980	982	1138	1069	1032
1976	947	1127	997	1052	1096	985	912	901	811	971	889	937
1977	823	849	878	949	920	710	930	810	741	978	734	715
1978	777	747	827	824	935	698	719	698	648	648	626	802
1979	823	802	905	806	983	920	841	871	856	857	839	714

Table IV.3. Numbers of reports in each monthly sample within area "C".

YEAR	Jan	Feb	Mar	Apr	May	Jun	Jul	Aug	Sep	Oct	Nov	Dec
1948	52	54	56	48	31	24	29	34	47	51	64	64
1949	53	36	86	44	16	42	23	26	39	44	63	61
1950	60	72	49	38	27	24	29	30	33	54	66	50
1951	56	48	55	57	39	19	33	36	39	57	82	64
1952	97	76	65	58	35	38	43	33	48	60	53	74
1953	71	58	42	38	33	18	29	33	40	38	57	58
1954	36	40	58	50	56	31	26	24	59	57	60	91
1955	70	60	74	53	93	27	33	26	39	52	53	51
1956	49	33	40	35	24	30	35	40	39	36	37	45
1957	67	64	44	34	28	18	23	46	51	62	43	87
1958	52	24	35	34	18	23	15	32	25	33	35	42
1959	48	51	71	51	26	22	20	17	24	39	60	77
1960	74	38	63	54	30	29	37	35	28	42	78	65
1961	110	79	48	45	34	24	25	12	52	86	75	73
1962	110	78	81	48	47	32	23	75	41	59	43	66
1963	42	56	70	25	38	33	12	23	29	40	56	57
1964	454	421	421	215	243	255	334	261	313	319	363	383
1965	403	332	361	265	248	210	296	209	212	249	265	299
1966	319	338	220	334	226	147	148	175	161	195	165	219
1967	312	314	288	211	182	155	137	182	182	215	214	226
1968	298	264	278	277	199	172	146	170	278	312	274	299
1969	326	256	292	243	209	231	116	230	164	222	270	271
1970	331	270	294	283	208	203	196	171	275	256	291	319
1971	430	378	669	576	679	597	506	390	665	548	589	530
1972	776	525	563	529	630	656	488	422	433	447	677	613
1973	756	674	794	650	580	563	452	354	276	325	222	303
1974	663	595	566	551	289	159	189	214	353	609	323	284
1975	326	361	423	428	326	477	169	219	229	318	330	194
1976	282	288	305	234	227	256	175	163	247	340	316	237
1977	316	277	252	160	135	126	127	93	132	198	170	233
1978	205	223	248	165	175	149	91	117	127	141	124	244
1979	204	255	231	136	145	210	133	122	145	192	170	165

Table IV.4. Numbers of reports in each monthly sample within area "D".

YEAR	Jan	Feb	Mar	Apr	May	Jun	Jul	Aug	Sep	Oct	Nov	Dec
1948	35	53	65	45	47	69	68	41	60	33	26	54
1949	90	75	90	82	111	93	94	83	91	69	71	78
1950	68	62	80	90	79	64	129	61	85	65	68	74
1951	66	87	86	78	96	81	96	105	112	83	107	100
1952	95	82	104	139	114	118	129	131	135	96	96	89
1953	115	97	71	149	142	111	123	136	124	120	123	133
1954	110	115	106	113	176	170	140	116	143	127	125	137
1955	128	140	148	142	126	153	140	153	152	157	136	125
1956	114	133	139	158	189	201	195	170	168	129	103	116
1957	106	79	127	139	191	208	196	159	157	166	164	153
1958	131	121	145	178	166	196	172	167	157	162	123	133
1959	140	135	140	121	137	169	159	184	125	154	156	160
1960	155	212	126	140	190	176	189	192	159	180	162	177
1961	133	170	191	194	217	183	150	221	170	175	138	148
1962	160	125	152	192	190	172	167	185	172	162	173	163
1963	147	161	167	178	171	156	174	157	173	173	152	129
1964	251	245	292	265	340	266	291	264	324	367	254	263
1965	280	165	337	370	335	350	332	303	315	316	282	263
1966	281	260	309	318	309	328	348	321	268	301	270	236
1967	263	226	298	327	378	323	277	245	239	308	276	247
1968	299	320	271	275	285	216	268	270	238	332	283	302
1969	301	237	309	357	341	277	240	290	241	248	257	266
1970	210	213	280	296	276	311	270	257	292	290	276	255
1971	83	98	150	153	136	107	117	328	317	292	287	286
1972	262	261	340	329	265	278	292	282	263	249	267	267
1973	258	238	264	305	281	364	325	287	350	224	249	238
1974	224	231	202	208	233	138	170	234	179	256	265	251
1975	214	228	316	265	317	339	356	427	355	353	412	327
1976	333	330	293	369	394	361	337	292	324	374	342	357
1977	322	278	380	362	350	268	343	307	254	359	246	231
1978	235	250	265	298	267	219	297	287	245	225	230	275
1979	275	293	339	345	404	420	357	381	346	348	331	302

Table IV.5. Numbers of reports in each monthly sample from Ocean Weather Station K.

YEAR	Jan	Feb	Mar	Apr	May	Jun	Jul	Aug	Sep	Oct	Nov	Dec
1948	0	0	0	0	0	0	0	0	0	0	0	0
1949	0	0	0	0	0	0	160	6	238	244	239	240
1950	230	220	226	233	242	233	248	184	128	244	236	239
1951	231	216	246	237	244	235	244	239	238	241	238	245
1952	226	227	244	238	223	96	242	243	205	246	235	246
1953	233	223	245	237	246	236	247	244	240	247	237	246
1954	225	192	228	224	55	182	229	226	92	13	231	199
1955	245	215	248	238	245	185	246	246	64	244	221	246
1956	246	231	246	237	247	238	246	248	239	223	239	240
1957	186	219	239	236	238	225	232	246	232	241	236	175
1958	237	220	184	0	0	0	0	0	0	0	0	0
1959	154	145	195	179	204	158	201	187	180	185	183	151
1960	232	188	176	213	230	222	222	232	213	216	194	225
1961	185	207	214	217	177	223	202	230	215	228	218	215
1962	174	169	236	203	227	217	207	225	216	213	201	213
1963	217	158	205	215	222	214	222	191	190	225	198	216
1964	223	180	185	187	210	181	201	220	209	200	203	194
1965	193	172	164	192	228	207	225	216	212	228	200	169
1966	227	196	214	198	179	199	145	211	220	173	223	223
1967	220	128	207	216	228	173	170	203	203	200	197	210
1968	199	201	217	199	213	23	146	138	168	207	210	116
1969	0	0	0	0	0	0	0	0	0	0	0	0
1970	0	0	0	0	0	0	0	0	0	0	0	0
1971	0	0	0	0	0	0	0	0	0	0	0	0
1972	0	0	0	0	0	0	0	0	0	0	0	0
1973	0	0	0	0	0	0	0	0	0	0	0	0
1974	0	0	0	0	0	0	0	0	0	0	0	0
1975	0	0	0	0	0	0	0	0	0	0	0	0
1976	0	0	0	0	0	0	0	0	0	0	0	0
1977	0	0	0	0	0	0	0	0	0	0	0	0
1978	0	0	0	0	0	0	0	0	0	0	0	0
1979	0	0	0	0	0	0	0	0	0	0	0	0

incorporating the wind speed dependence, following the more recent recommendations of Large and Pond (1981) who find a linear increase in drag coefficient with wind speeds greater than 11 m/sec.

Low frequency variations in the meridional and zonal stress component series are displayed in Figs. IV.4 and IV.5. Because the raw data series contain so much detail that they are difficult to compare visually, a 12-month running mean filter was used to suppress seasonalities and smooth the higher frequencies in order to bring out the longer period signal in these figures. Important non-seasonal variations of longer than annual period are apparent. In general, the choice of drag coefficient formulation does not appear to be crucial in determining the general nature of the indicated long period variability, although the variable coefficient formulation does tend to amplify large anomalies compared to the constant coefficient formulation. Major long period features in the time series appear to be rather consistent among adjacent areas, for which the data sets are entirely independent, thus suggesting that these indications truly reflect actual low frequency variability.

Correlations among the various series, after application of the 12th-difference transformation to each, (with no 12-month running mean filter applied) are summarized in Tables IV.6 and IV.7.

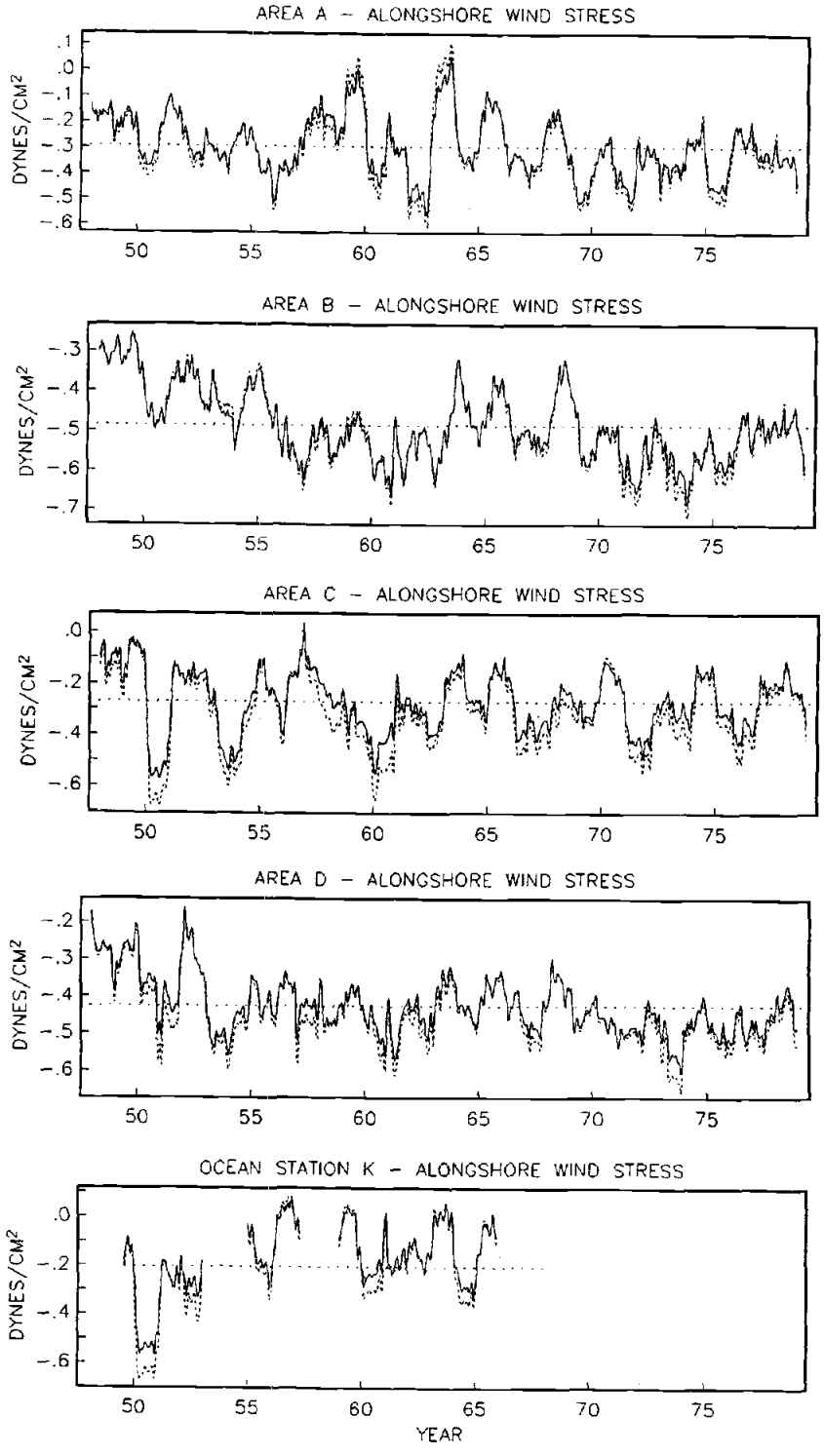

Figure IV.4. 12-month running mean values of monthly series of meridional (alongshore) wind stress; positive values denote northward stress. Units are dynes cm^{-2}. The solid line denotes the constant drag coefficient formulation; the dashed line denotes the variable drag coefficient formulation which is dependent on wind speed and atmospheric stability.

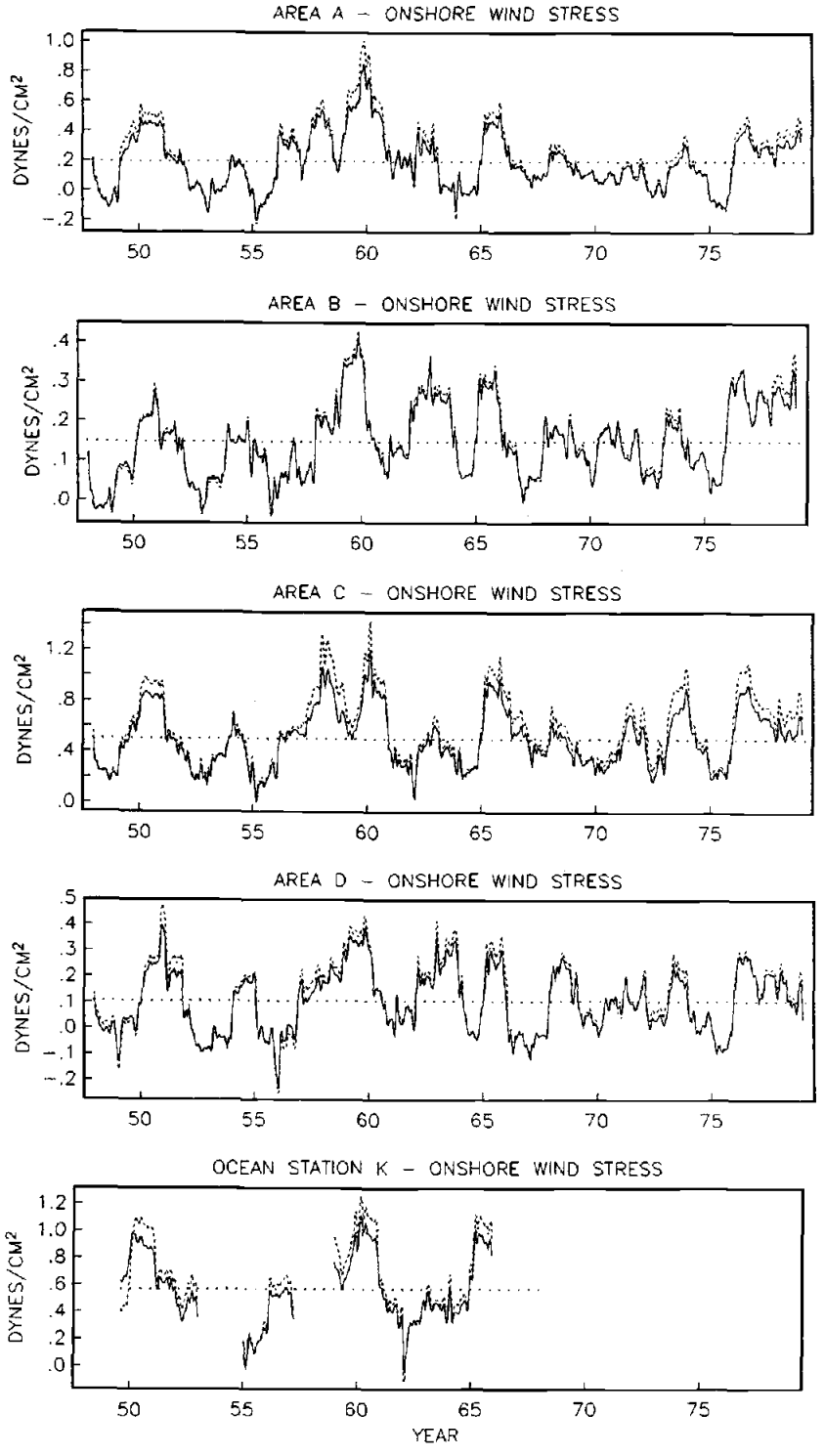

Figure IV.5. 12-month running mean values of monthly series of zonal wind stress; positive values denote eastward (onshore) stress. Units are dynes cm^{-2}. The solid line denotes the constant drag coefficient formulation; the dashed line denotes the variable drag coefficient formulation which is dependent on wind speed and atmospheric stability.

All the correlation coefficients in Tables IV.6 and IV.7 are highly significant ($p << .01$). Among pairs of series of zonal component of stress, correlation tends to be strongest in zonal adjacent areas. Similarly, among series of meridional component, correlation tends to be strongest among meridionally adjacent pairs. Thus we have the intuitively satisfying result that, among areas where the given wind component blows directly from one to the other, the corresponding stress component series are most highly correlated, even on interyear time scales (i.e., even after the energetic seasonal and synoptic 'event' scales of variation are suppressed). On the whole, the zonal components seem to be more highly correlated than the meridional components.

When the relationships among the stress component series were examined seasonally, the correlations tended to drop sharply in the summer season, except in the case of the meridional stress series for areas 'A' and 'B'. Thus the correlations among series tend to be highest where the system is energetic, i.e., (1) in seasons other than the summer in all the areas, and (2) in the summer in the alongshore component in the pair of areas adjacent to the coastal boundary, where energetic alongshore winds are associated with the summer upwelling system.

We can form monthly estimates of wind stress shear by taking differences of appropriate pairs of the stress

Table IV.6. Linear correlation among 12th-differenced monthly time series of meridional component of wind stress, by areas shown in Fig. IV.1. (Correlations involving OWS-K represent 204 data pairs; the others involve 372 data pairs.)

	K	C	A	D
C	.80			
A	.56	.55		
D	.58	.59	.53	
B	.56	.54	.76	.67

Table IV.7. Linear correlation among 12th-differenced monthly time series of zonal component of wind stress by areas shown in Fig. IV.1.

	K	C	A	D
C	.82			
A	.72	.74		
D	.38	.51	.48	
B	.42	.53	.49	.87

component time series, and dividing each by the respective differences in the mean monthly positions of the available reports. Thus, the differences in the meridional stress component series for areas 'A' and 'C', and for areas 'B' and 'D', provide two independent monthly time series of large scale zonal shear in the meridional stress. Similarly differences in monthly estimates of zonal stress between areas 'A' and 'B', and between areas 'C' and 'D', provide corresponding series of meridional shear in the zonal stress.

Low frequency aspects of the resulting monthly wind stress shear time series are illustrated by 12-month running means in Fig. IV.6. Certain of the major low frequency nonseasonal features are clearly shared between paired independent wind stress shear series. A stronger visual correspondence is evident among the series of shear in the zonal (onshore) stress component than in the series of shear in the meridional (alongshore) stress. Of course, exact correspondence is not expected since the nominal locations defining respective shear components are offset from one another by some 5 degrees With this in mind, the degree of visual correspondence in these low frequency variations (where higher amplitude fluctuations of shorter scale, which might have been expected to be more highly correlated, have been filtered and smoothed) is satisfying. The inference is that we are indeed able to discern, in

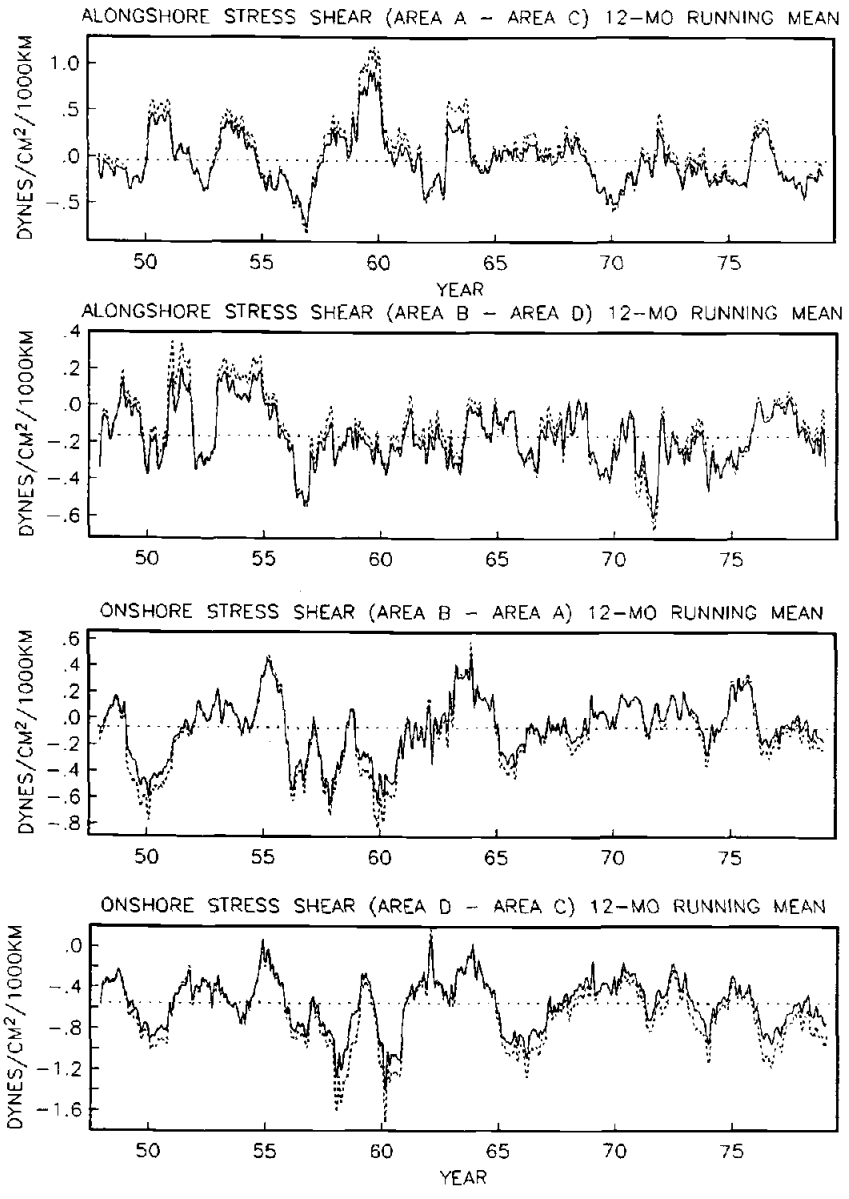

Figure IV.6. 12-month running mean values of wind stress shear. Positive values denote cyclonic shear; units are dynes cm^{-2} per 1000 km. The solid line denotes the constant drag coefficient formulation; the dashed line denotes the variable drag coefficient formulation which is dependent on wind speed and atmospheric stability. *Top panel:* Shear in the alongshore wind stress field, produced by subtracting the monthly values of alongshore stress (positive northward) for area 'C' from the corresponding values for area 'A'. *Second panel:* Shear in the alongshore wind stress field, produced by subtracting the monthly values for area 'D' from the values for area 'B'. *Third panel:* Shear in the onshore wind stress field, produced by subtracting the monthly values zonal stress (positive eastward) for area 'A' from the corresponding values for area 'B'. *Bottom panel:* Shear in the onshore wind stress field, produced by subtracting the values for area 'C' from the values for area 'D'.

this case, significant interyear variability in wind stress shear components derived from maritime data.

The paired series (i.e., 'A'-'C' and 'B'-'D') of zonal shear in the meridional stress component, $\frac{\partial \tau_y}{\partial x}$, exhibit linear correlation coefficients of: r=.42 for the raw series, r=.36 for the 12th-differenced series (i.e., with seasonal periodicities and linear trends removed), and r=.26 for the 12-month running mean filtered series. (The one percent significance level for the 372 to 384 data points involved in these various series is about r=.13.) Correlation among the paired series (i.e., 'B'-'A' and 'D'-'C') of meridional shear in the zonal stress is substantially higher. For the raw series, r=.65; for 12th-differences, r=.62; for 12-month runing means r=.75. No seasonal pattern in degree of correlation is apparent.

No clear explanation for the higher degree of spatial correlation in the shear in the zonal stress, compared to the shear in the meridional stress, is available. One might speculate that since the zonal stress component has the nature of being a continuation of the large scale zonal flow that crosses the Atlantic at this latitude band, that it might have larger spatial scales than the meridional component.

We thus have time series of shear components which seem to carry a tangible signal of real interyear variability. Combining shear components into an estimate of

the curl of the sea surface wind stress is possible. Here we use the Cartesian coordinate form of the curl operator

$$\vec{k} \cdot \nabla \times \vec{\tau} = \frac{\partial \tau_y}{\partial x} - \frac{\partial \tau_x}{\partial y} \qquad (4.1)$$

rather than the polar coordinate formulation defined in Eq. 2.1.

However, each estimate of shear in the meridional stress involves data from an area extending 10 degrees of longitude by 5 degrees of latitude, and each estimate of shear in the zonal stress involves an area extending 5 degrees of longitude by 10 degrees of latitude. Any two such areas combined to yield a curl computation overlap in a 5-degree quadrangle. Four such combinations are possible from the stress shear series described, overlapping in each of the areas 'A', 'B', 'C', and 'D' (Fig. IV.1). For the purpose of indicating wind stress curl time series, we designate each of the possible combinations by the letter designation of the area of overlap (shown in Fig. IV.1). Thus the letter would indicate the best available curl estimate for the particular associated area, even though the estimate is necessarily of somewhat larger scale. Also, we must keep in mind that each of the four wind stress curl time series so constructed shares some amount of data with the other three; none of the series of curl estimates is independent of any of the others.

Low frequency nonseasonal features of the four time series of wind stress curl are displayed in Fig. IV.7. In the sections to follow, each of these time series will be considered to be an estimate of the wind stress curl acting upon the five degree area corresponding to the associated letter designation.

IV.4 Covariation with Other Maritime Data-based Time Series.

In this section we compare wind stress curl estimates and the components of the vector wind stress to monthly series of sea surface temperature, surface atmospheric pressure, total cloud amount, and to the "W^3" index of rate of work done on by the wind, providing energy for turbulent mixing of the water column. A gross error check was initially applied to remove impossible values of the various measurements and a monthly mean of the observations was taken to characterize the monthly value. In the case of the "w^3" wind mixing index the procedure of Bakun (1987) is followed; that is, the scalar wind speed indicated in each report was raised to the third power (i.e., 'cubed') and then averaged.

Tables IV.8 to IV.11 present correlations among 12th-differenced monthly values of the various series. (In the 12th-differenced series, 372 monthly data points are available for the period 1948-79; the one percent

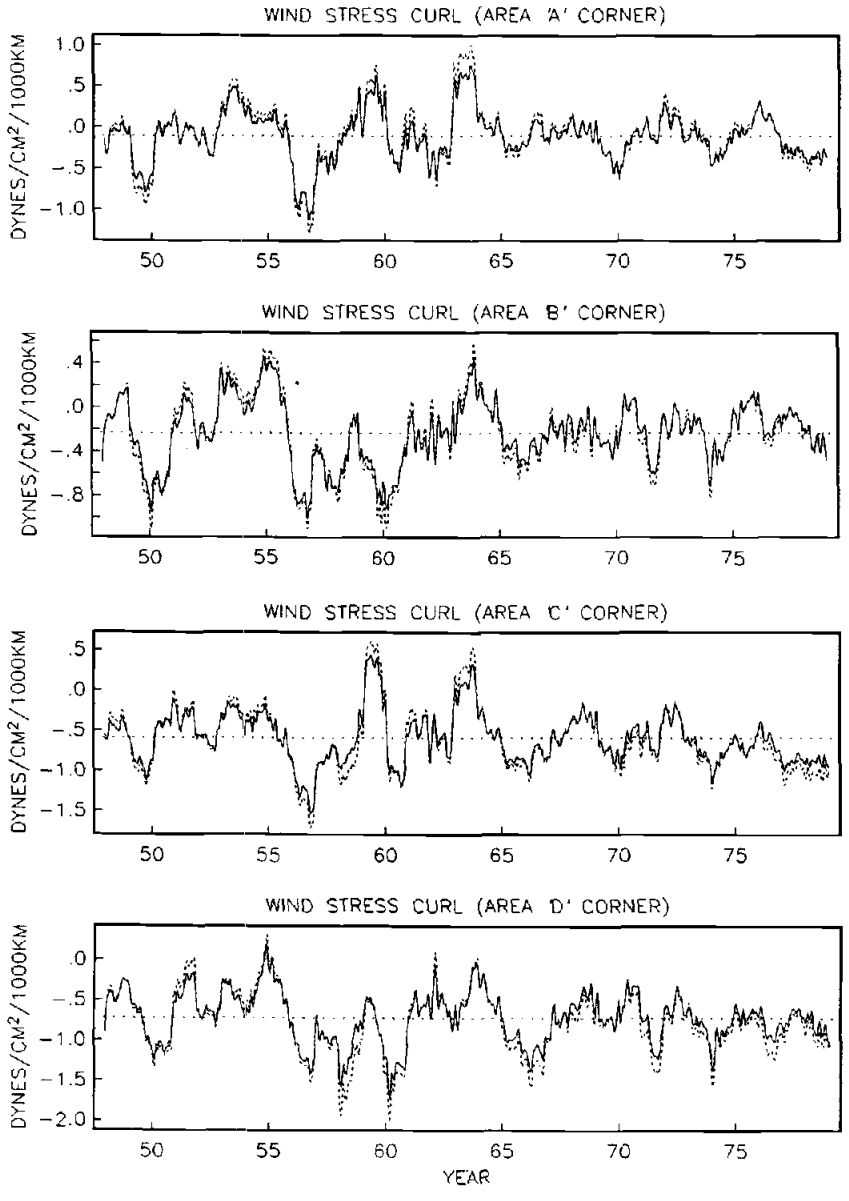

Figure IV.7. 12-month running mean values of wind stress curl. Positive values denote cyclonic curl; units are dynes cm^{-2} per 1000 km. The solid line denotes the constant drag coefficient formulation; the dashed line denotes the variable drag coefficient formulation which is dependent on wind speed and atmospheric stability. *Top panel:* Wind stress curl series assigned to area 'A', produced by summing shears in the alongshore stress field (area 'A' - area 'C') and in the onshore stress field (area 'B' - area 'A'). *Second panel:* Wind stress curl series assigned to area 'B', produced by summing shears in the alongshore stress field (area 'B' - area 'D') and in the onshore stress field (area 'B' - area 'A'). *Third panel:* Wind stress curl series assigned to area 'C', produced by summing shears in the alongshore stress field (area 'A' - area 'C') and in the onshore stress field (area 'D' - area 'C'). *Bottom panel:* Wind stress curl series assigned to area 'D', produced by summing shears in the alongshore stress field (area 'B' - area 'D') and in the onshore stress field (area 'D' -area 'C').

significance level for the correlation coefficients is about r=.13; the five percent level is about r=.10.)

It is important to note that the stress components in each given area have been used in the curl computation applied to that area. The result is that the stress components and the stress curl would tend to be correlated in any case and the correlation coefficients would tend to be either positive or negative depending upon whether the given stress component were added or subtracted in the curl computation for the particular area. Thus they are entered in Tables IV.8 to IV.11 not to demonstrate a linkage between stress components and stress curl, but to provide a ready reference to the sign of the linkage imposed by the computation.

Nonseasonal variation in wind stress curl is highly correlated, negatively, to barometric pressure in all areas; this is not unexpected due to the association of low pressure systems with cyclonic wind patterns. The other wind series, W^3, τ_y, and τ_x, are likewise consistently negatively correlated with pressure. (Here we note that although the signs of the correlation coefficients of stress components with stress curl alternate according to the computation procedure assigned for a given "corner" of the ten-degree quadrangle, the signs of the correlation coefficients of these series with the independently derived pressure series are consistent in all four five-degree

Table IV.8. Linear correlation coefficients for pairs of 12th-differenced monthly time series constructed for area 'A' (Fig. IV.1).

	Curl	Pressure	Cloud	SST	W^3	τ_y
Pressure	-.33					
Cloud	.07	-.45				
SST	.10	-.03	.05			
W^3	-.03	-.44	.25	-.04		
τ_y	.36	-.41	.21	.33	-.02	
τ_x	-.35	-.45	.44	-.01	.42	.17

Table IV.9. Linear correlation coefficients for pairs of 12th-differenced monthly time series constructed for area 'B' (Fig. IV.1).

	Curl	Pressure	Cloud	SST	W^3	τ_y
Pressure	-.51					
Cloud	.18	-.54				
SST	.13	-.08	-.07			
W^3	.09	-.36	.26	-.14		
τ_y	.23	-.29	.06	.35	-.44	
τ_x	.18	-.54	.50	.01	.35	.11

Table IV.10. Linear correlation coefficients for pairs of 12th-differenced monthly time series constructed for area 'C' (Fig. IV.1).

	Curl	Pressure	Cloud	SST	W^3	τ_y
Pressure	-.33					
Cloud	.01	.00				
SST	.00	.09	-.27			
W^3	-.07	-.60	-.02	-.16		
τ_y	-.23	-.13	-.12	.21	-.19	
τ_x	-.30	-.53	-.03	-.18	.63	-.14

Table IV.10. Linear correlation coefficients for pairs of 12th-differenced monthly time series constructed for area 'C' (Fig. IV.1).

	Curl	Pressure	Cloud	SST	W^3	τ_y
Pressure	-.51					
Cloud	.06	-.16				
SST	.02	-.07	-.33			
W^3	.39	-.44	.32	-.20		
τ_y	-.26	-.13	-.25	.27	-.53	
τ_x	.29	-.56	.00	.03	.34	-.02

subareas.) Thus on the interyear time scale, anomalous low pressure (typical of stormy conditions) is shown to be generally associated with anomalously northward and eastward tendency in the wind stress pattern, and with anomalously large addition of turbulent mixing energy to the ocean by the wind. This is not an unexpected result, but will be important to note when trying to empirically separate the relationships of any of the different wind effects to other properties.

For example, nonseasonal variation in sea surface temperature (SST) tends to be positively correlated with wind stress curl, although significantly so only in the time series for area 'B'. One might be tempted to interpret this as a demonstration of an effect of lessened upward Ekman pumping of cooler water. However, we note a strong positive correlation of SST with meridional wind stress in all the areas, which may be a combined effect of a relaxation of coastal upwelling and air-sea heat flux effects of anomalous southerly wind. In this case, the relationship between stress curl and meridional stress, through the linkage to the storm patterns makes it impossible to confidently separate the effects. The relationships to SST are more thoroughly investigated in section IV.6. However, this non-independence of indicators of various different physical mechanisms is a continual problem in the empirical analysis of cause and effect in

interyear ocean variability.

Cloud cover is also bound up in the relationship to surface pressure, wind curl, etc., probably mainly through a relationship of vertical atmospheric motion to wind divergence. Cloud cover is, of course, an important regulator of air-sea heat flux, and thus may interact in the interyear variability in sea level and SST, which is investigated in the following two sections.

IV.5 Modelling Interyear Variation in Coastal Sea Level

One useful signal of interyear variability in ocean processes is provided by routine measurements of coastal sea level. For this study, monthly average tidal height was obtained, through the Permanent Service for Mean Sea Level, for two tidal stations on the west coast of the Iberian Penninsula: Vigo, Spain, and Cascais, Portugal (see Fig. IV.1 for locations). The data for Vigo run from 1948, which is the beginning of our various maritime data-based time series, through 1963. The data for Cascais run over the entire period, 1948-79, except for a fifteen-month data gap from February, 1959, through April, 1960. Data exist for extended periods prior to 1948 at both stations.

Sea level variations reflect contributions from a number of processes including sea surface slopes due to currents, effects of local winds, precipitation or runoff, atmospheric pressure variation, and thermal effects

(Montgomery, 1938), and also contributions of non-locally forced sea height variations which may propagate into the area as coastal trapped waves (e.g., Enfield and Allen, 1980). The use of monthly averages effectively filters out major periodic tidal effects (Pattullo et al., 1955). This section describes the results of explorations, via stepwise linear regression, of the linkage of interyear variability in the Vigo and Cascais sea level signals to various ocean processes indicated by the maritime data series described in the previous two sections.

The monthly sea level data were corrected to remove the "inverted barometer effect" of atmospheric pressure by adding, to each monthly average sea level value, one cm for each one millibar difference in monthly mean atmospheric pressure as extracted for the station position from the appropriate monthly mean of synoptic surface atmospheric pressure analyses produced by Fleet Numerical Oceanography Center.

All data series were transformed to 12th-differences in order to remove annual periodicities and long term linear trends. Stepwise regression models were constructed for sea level at Vigo versus maritime data series from area 'A' (see Tables IV.12 to IV.14), and at Cascais versus series from area 'B' (see Tables IV.15 to IV.17). In addition, the relative sea level difference between Vigo and Cascais (Vigo minus Cascais; i.e., positive difference

Table IV.12. Summary of stepwise regression analysis of sea level time series at Vigo versus various time series from area 'A'.

Step	Entering Variable	Mult. r2	Sig. of Model	Beta Wt. in Full Model
1	τ_y (P<.00001)	.165	P<.00001	.29 (P<.001)
2	SST (P=.006)	.201	.00001	.21 (P=.003)
3	τ_x (P=.106)	.213	.00001	.15 (P=.049)
4	CURL (P=.250)	.219	.00001	.09 (P=.250)

Table IV.13. Summary of stepwise regression analysis of sea level time series at Vigo versus various time series from area 'A' (winter season, Dec-Feb, only).

Step	Entering Variable	Mult. r2	Sig. of Model	Beta Wt. in Full Model
1	τ_y (P=.00001)	.386	P<.00002	.43 (P=.002)
2	SST (P=.126)	.419	.00002	.39 (P=.008)
3	τ_x (P=.056)	.469	.00002	.30 (P=.019)
4	CURL (P=.057)	.516	.00002	.27 (P=.057)

Table IV.14. Summary of stepwise regression analysis of sea level time series at Vigo versus various time series from area 'A' (summer season, Jun-Aug, only).

Step	Entering Variable	Mult. r2	Sig. of Model	Beta Wt. in Full Model
1	SST (P=.035)	.100	P<.035	.24 (P=.15)
2	CURL (P=.313)	.121	.067	.19 (P=.27)
3	τ_x (P=.560)	.129	.126	.09 (P=.56)

Table IV.15. Summary of stepwise regression analysis of sea level time series at Cascais versus various time series from area 'B'.

Step	Entering Variable	Mult. r2	Sig. of Model	Beta Wt. in Full Model
1	τ_y (P<.00001)	.185	P<.00001	.29 (P<.0001)
2	SST (P<.00001)	.250	.00001	.27 (P<.0001)
3	CURL (P=.0001)	.283	.00001	.16 (P=.0007)
4	τ_x (P=.0027)	.302	.00001	.14 (P=.003)

Table IV.16. Summary of stepwise regression analysis of sea level time series at Cascais versus various time series from area 'B'(winter season, Dec-Feb, only).

Step	Entering Variable	Mult. r2	Sig. of Model	Beta Wt. in Full Model
1	SST (P<.00001)	.242	P<.00001	.29 (P=.002)
2	τ_y (P=.0004)	.348	.00001	.35 (P=.0002)
3	τ_x (P=.0007)	.434	.00001	.29 (P=.002)
4	CURL (P=.14)	.448	.00001	.12 (P=.14)

Table IV.17. Summary of stepwise regression analysis of sea level time series at Cascais versus various time series from area 'B'(summer season, Jun-Aug, only).

Step	Entering Variable	Mult. r2	Sig. of Model	Beta Wt. in Full Model
1	SST (P=.00004)	.181	P<.00005	.32 (P=.002)
2	CURL (P=.003)	.266	.00001	.31 (P=.003)
3	τ_x (P=.79)	.266	.00001	-.03 (P=.79)

indicates upward slope toward the north) was tested against data from both areas (see Tables IV.18 to IV.20); the process of taking 12th-differences effectively removes any constant or linearly varying datum differences between the two stations, yielding an estimate of nonseasonal variation in large scale alongshore sea level slope.

Explanatory variable series tested included northward and eastward components of sea surface wind stress (denoted by symbols: τ_y and τ_x), sea surface temperature (symbol: SST) and wind stress curl (symbol: CURL). Where series form both areas may be involved in the same model, they are differentiated by a subscript "A" or "B" added to the symbol. Lagged variables were not investigated as response of sea level to wind variations tends to occur within small fractions of a month (e.g., Smith, 1974), and steric effects (i.e., effects of sea temperature) are intrinsically contemporaneous; for example, Marthaler (1976) found the relationship between monthly average sea level and alongshore current to be at zero lag. (Note that Tables IV.12 to IV.20 list certain steps beyond the point at which one would ordinarily halt a stepwise regression; in this case we are comparing model formulations among locations and seasons, and so consistently repeated tendencies, even if non-significant in the sense of rejecting a null hypothesis in an individual model analysis, might be of interest.) Regression coefficients

Table IV.18. Summary of stepwise regression analysis of "Vigo - Cascais" sea level difference time series versus various time series from areas 'A' and 'B'.

Step	Entering Variable	Mult. r2	Sig. of Model	Beta Wt. in Full Model
1	τ_{yA} (P=.011)	.042	P=.011	.14 (P=.09)
2	τ_{xA} (P=.022)	.075	.003	.29 (P=.007)
3	$CURL_B$ (P=.143)	.088	.003	.15 (P=.18)
4	SST_A (P=.200)	.099	.004	.11 (P=.20)

Table IV.19. Summary of stepwise regression analysis of "Vigo - Cascais" sea level difference time series versus various time series from areas 'A' and 'B' (winter, Dec-Feb, only).

Step	Entering Variable	Mult. r2	Sig. of Model	Beta Wt. in Full Model
1	τ_{yA} (P=.17)	.052	P=.17	.84 (P=.024)
2	SST_B (P=.36)	.074	.26	-.29 (P=.21)
3	$CURL_A$ (P=.42)	.092	.34	-.40 (P=.064)
4	τ_{yB} (P=.17)	.143	.26	.72 (P=.072)
5	SST_A (P=.17)	.194	.21	.35 (P=.17)

Table IV.20. Summary of stepwise regression analysis of "Vigo - Cascais" sea level difference time series versus various time series from areas 'A' and 'B' (summer, Jun-Aug, only).

Step	Entering Variable	Mult. r2	Sig. of Model	Beta Wt. in Full Model
1	τ_{yA} (P=.26)	.035	P=.26	-.45 (P=.08)
2	τ_{yB} (P=.23)	.073	.26	.18 (P=.43)
3	$CURL_A$ (P=.69)	.077	.42	.17 (P=.46)
4	τ_{xA} (P=.46)	.091	.50	.24 (P=.44)

are expressed in the Tables as "Beta weights", i.e., standardized regression coefficients (Neter and Wasserman, 1974, page 268), in order to facilitate comparison.

Alongshore component of sea surface wind stress was the most "important" of the variables tested in explaining interyear nonseasonal variation in corrected sea level at these locations. Regression coefficients are generally highly significant and invariably positive, such that northward stress tendency is associated with increased sea level. The seasonal tests tend to yield less conclusive results due to reduction in data points by a factor of four. However, the winter seasonal tests do indicate a highly significant effect of alongshore stress. The summer tests at both locations (Tables IV.14 and IV.17) indicate a predominant effect of sea surface temperature among the variables tested and no major effect of alongshore stress. However, we noted (Tables IV.8 and IV.9) that alongshore stress and SST tended to be strongly correlated in the coastal areas (i.e., in area A, r=.33; in area 'B', r=.35); the correlations for July (only) increase to .60 and .53, respectively. Thus it appears that SST is acting somewhat as a proxy variable for summer nonseasonal variation in alongshore stress through the coastal upwelling linkage.

The models of the sea level differences between the two stations were not highly significant. Perhaps the double subtractions involved in forming differences of

12th-differences, in a situation where the slope must certainly be very slight, may have caused major degradation of signal-to-noise ratio. However, in the models for all months (Table IV.18) and for winter (Table IV.19) increased northward stress tendency in area 'A' was significantly related to an upward tendency toward the north in the slope of sea level along the coast (i.e., sea level change at Vigo minus sea level change at Cascais being greater than zero).

Sea surface temperature tended to be the second most important explanatory variable (except for the summer models just discussed, where it appeared as the most important) in the models of nonseasonal sea level variation. In all cases the relationship was positive (i.e., positive Beta weight indicating positive slope) as would be the correct sense for the corresponding steric effect. Although the indications do not meet significance criteria, in the summer model of alongshore sea level slope (Table IV.19) where both SST variables appeared within the first five variables entering, the relationship with SST_A was in the positive sense and with SST_B was in the negative sense, i.e., such as would correspond to a tendency for northward upward steric slope of the sea surface. Onshore (eastward) wind stress tended to be a less important, but generally significant, explanatory variable. The relationship to sea level height was invariably positive;

i.e., increased onshore stress tendency corresponded to increased sea level. In the model of alongshore sea level slope (Table IV.18) onshore stress in the northward area tended to correspond to increased sea level height at Vigo relative to that at Cascais.

Wind stress curl appeared as a significant contributing variable at Cascais (Table IV.15). We have noted the tendency for CURL to be correlated with both stress components (Tables IV.8 and IV.9), which may have tended to mask its effect in the regression analysis. We do note that, whether meeting significance criteria or not, the fitted slope is invariably positive; i.e., increased northward flow tendency, according to the Sverdrup transport assumption, corresponding to a tendency for increased sea level at the coast.

The foregoing presents an example of the difficulty faced in attempting to sort out various causal mechanisms empirically, when so many of the forcing functions are mechanistically linked. Table IV.21 presents coefficients of univariate correlation among the various combinations of one dependent and one independent variable (i.e., without allowing any additional variables to interact). Note again that throughout this discussion we are referring to 12th-differenced series; thus in discussing apparent relationships among variables, the intended implication is that these involve monthly data points from which cyclic

Table IV.21. Correlation coefficients between 12th-differenced monthly time series of corrected sea level at Vigo and Cascais, and the difference between them, with various explanatory variable series. Correlation coefficients significant at the .05 level are followed by an asterisk; those significant at the .01 level are followed by two asterisks. The symbol SST_{A-B} denotes the 12th-differenced monthly series of sea surface temperature difference between areas 'A' and 'B' (SST_A-SST_B).

	Vigo	Cascais	Vigo-Cascais
γ_{yA}	.41**	.34**	.21**
γ_{yB}	.50**	.43**	.20**
γ_{xA}	.12	-.04	.19*
γ_{xB}	.23**	.20**	.11
SST_A	.30**	.27**	.16*
SST_B	.44**	.39**	.12
$CURL_A$	.17*	.26**	-.03
$CURL_B$	.14	.29**	-.02
SST_{A-B}	-.15*	-.19**	.04

seasonal effects and long term linear trends have been removed.

Corrected sea level at Cascais is significantly correlated with all of the variables tested except zonal (onshore/offshore) wind stress in the area to the north (area 'A'). Corrected sea level at Vigo is significantly correlated with all variables except zonal stress in area 'A' and the wind stress curl estimate for area 'B'. In each case of significant correlation the sign of the coefficient is "correct" relative to the mechanisms discussed above: (1) increased northward wind stress, implying increased onshore Ekman transport, correlates positively with higher sea level; (2) increased SST, implying increased steric height, is likewise associated with higher sea level; (3) cyclonic wind stress curl, i.e., northward transport according to the Sverdrup balance assumption, is correlated with coastal sea level in the sense that the associated onshore-offshore sea surface slope would contribute to geostrophic balance of the implied flow variation.

In addition, zonal stress in area 'B' is also significantly correlated with corrected sea level height at both stations. It seems noteworthy that zonal stress in area 'B' is very highly inversely correlated with barometric pressure (Table IV.9). Since barometric pressure has been added to the raw sea level time series in the correction procedure, in the case of no relationship

between zonal stress and raw sea level the tendency would have been for negative correlation with corrected sea level. However the observed correlation is positive, and because it overcomes this "built in" tendency for negative correlation, may represent a higher degree of relationship than indicated by the magnitude of the correlation coefficient. The correlation of zonal stress in area 'B' with corrected sea level is also higher than its intercorrelation with the other explanatory variables, τ_y, SST, and CURL (see Table IV.9), for which mechanistic explanations for relationship to corrected sea level can be fairly readily advanced. The sense of the indicated relationship would correspond to a "set up" of sea surface slope toward the coast by coastward wind stress, although such an implied lack of strong Coriolis effect is not consistent with the rather large time and space scales addressed in this analysis.

Correlation of the various explanatory variable series with variation in alongshore sea surface slope implied by the variation in the Vigo - Cascais corrected sea level difference (Table IV.21) is lower than with the corrected sea level values themselves. The highest correlation is with alongshore wind stress; the sense of the correlation is consistent with the requirement for continuity in the onshore-offshore flow components provided by geostrophic flow opposing the Ekman transport implied by the alongshore

stress.

Table IV.21 also lists the correlations of corrected sea level at the two stations, and the sea level difference, with the sea surface temperature difference between areas 'A' and 'B'. The negative correlations with corrected sea level imply increased north-south temperature contrast with higher coastal sea level; i.e., increased northward alongshore advection in winter or decreased southward alongshore advection in summer tends to be reflected in increased alongshore temperature gradient. The relationship of alongshore temperature difference to sea level difference is nonsignificant, but the sign of the correlation coefficient is positive which is the correct sense for the implied contrast in steric height to affect the sea level contrast.

IV.6 Modelling Interyear Variation in the Evolution of Sea Surface Temperature

The evolution of the sea surface temperature field will reflect a number of the processes we have been discussing. For example, Ekman pumping by wind stress curl would tend to cool the surface layer, as would turbulent mixing that erodes stable thermal structure in the upper water column. Near the coast, equatorward alongshore wind stress drives coastal upwelling and associated cool advection from the north, which would likewise cool the

ocean surface layer. Eastward (westward) stress would imply southward (northward) Ekman transport, i.e., cool (warm) advection in the ocean surface layers.

Thus it is the rate of change in SST, rather than the actual SST value, that we wish to test for empirical associations with processes that can be inferred from the maritime data series described above. For this analysis, a special series of estimates was assembled for each area (shown in Fig. IV.1) to characterize sea surface temperature at the beginning and end of each given month, in order to yield an estimate of monthly temperature change. Each series was defined as the average of the observations available with a given area within the period from the twenty-sixth day of a particular month through the fifth day of the following month. Subtraction of successive values yields monthly series of the estimated increase or decrease of sea surface temperature occurring within the monthly time increment.

A major component of sea surface temperature change is expected to occur though air-sea heat exhanges. The various heat exchange components can be estimated from maritime observations through various "bulk" formulations. Here the procedures of Bakun (1987), which adhere basically to the procedures of Nelson and Husby (1983), with certain modifications indicated below, are followed.

The net atmosphere ocean heat exhange, Q_N, is a sum of various heat exchange components, i.e.,

$$Q_N = Q_S - Q_B - Q_E - Q_C \qquad (4.2)$$

where Q_S is the net incoming solar radiation absorbed by the ocean, Q_B is the effective long wave back radiation, Q_E is the evaporative heat loss from the sea surface,and Q_C is the conductive heat loss from the sea surface.

Q_S was estimated according to

$$Q_S = (1 - a)\ Q_0\ (1 - 0.62C + 0.0019h) \qquad (4.3)$$

where a is the fraction of incoming radiation reflected from the sea surface, Q_0 is the sum of the direct and diffuse radiation reaching the ground under a cloudless sky, C is the observed total cloud amount in tenths of sky covered, and h is the noon solar altitude.

Estimation of Q_0 is as follows. For each maritime report, the total daily direct solar radiation reaching the ground under cloudless conditions was extracted from the Smithsonian Meteorological Tables (List, 1949) as a function of the date and latitude of the report, using a 4 x 4 element curvilinear interpolation via Bessel's central difference formula and assuming an atmospheric transmission coefficient of 0.7 (as recommended by Seckel and Beaudry,

1973). The diffuse solar radiation was estimated according to List's recommendations as follows. The solar radiation reaching the top of the atmosphere was extracted from the appropriate tables via a similar interpolation procedure. This value was reduced by nine percent to allow for water vapor absorption and by two percent to allow for ozone absorption. The result was then subtracted from the value previously determined for the direct radiation reaching the ground to yield the energy scattered out of the solar beam. This in turn was reduced by fifty percent (to reflect the fact that half is diffused upward and therefore only half is diffused downward) to yield the total diffuse radiation reaching the ground. The total daily direct and diffuse radiation values corresponding to each report are then summed to yield Q_S.

The remainder of the computation follows the procedures adopted by Nelson and Husby (1983). The linear cloud correction in Eq. 4.3 is as suggested by Reed (1977), and Reed's recommendation that no correction be made for cloud amounts less than twenty five percent of total sky was followed. Sea surface albedo, a, was extracted from Payne's (1972) tables, following Nelson and Husby's (1983) algorithm which involves entering the tables with the 0.7 atmospheric transmission coefficient reduced by a factor equal to the linear cloud correction applied in Eq. 4.3 and the mean solar altitude. The error in the net radition

estimate introduced by entering entering Payne's albedo tables with the mean daily solar altitude to indicate albedo, rather than performing an integration over the entire day of entries at short time intervals with instantaneous solar altitudes, is estimated to be less than one percent at these latitudes.

Effective back radiation, Q_B, is the difference between the outgoing long-wave radiation from the sea surface which depends on the fourth power of the absolute temperature of the sea surface, and the incoming longwave radiation from the sky, which depends on the water vapor content of the atmosphere and the nature of the cloud cover. Here the computational scheme of Nelson and Husby (1983) was followed exactly; the modified Brunt equation (Brunt, 1932) was used with the empirical constants of Budyko (1956) and the linear cloud correction formula of Reed (1976) to compute the effective back radiation, i.e.,

$$Q_B = 5.50x10^{-8}(T_S + 273.16)^4(0.39-.05e_a^{1/2})(1-0.9C) \quad (4.4)$$

The vapor pressure of the air, e_a, was computed according to the formula provided by List (1949) using the observed barometric pressure, and "dry bulb" and "wet bulb" air temperatures. For reports that were without an acceptable wet bulb temperature, the vapor pressure was computed as the saturation vapor presure at the dew point temperature

using an integrated from of the Clausius - Clapeyron equation (Murray, 1967).

In estimating evaporative heat loss (latent heat transfer), Q_E, and conductive heat loss (sensible heat transfer), Q_C, the procedures of Nelson and Husby were again closely followed, except for a modification of the wind speed dependence in their variable transfer coefficient formulations as described below. The bulk aerodynamic formulae for turbulent fluxes of latent heat, Q_E, and sensible heat Q_C across the air-sea interface in a neutrally stable atmospheric boundary layer can be expressed (Kraus, 1972) as

$$Q_E = \rho_a L C_E (q_0 - q_{10}) w \tag{4.5}$$

$$Q_C = \rho_a c_p C_H (T_s - T_a) w \tag{4.6}$$

where ρ_a is the density of air, considered constant at 1.22 kg m^{-2}. w is the wind speed at 10 m height. L is the latent heat of vaporization, assigned a constant value of 1000 J kg^{-1}. c_p is the specific heat of air, assigned a constant value of 1000 J kg^{-1} C^{-1}. The empirical exchange coefficients, C_E and C_H, were assigned constant values of 0.0013 in producing the basic set of time series used in this study. In addition, time series based on variable transfer coefficient formulations incorporating

dependencies on atmospheric stability and wind speed were also assembled for comparison. These formulations are again similar to those chosen by Nelson and Husby (1983), incorporating the atmospheric stability effect according to a bulk Richardson number parameterization (Deardorf, 1968); however, in this case Nelson and Husby's wind speed dependencies were modified according to the recommendations of Large and Pond (1982) who suggest an increase in C_E and C_H which is proportional to the square root of the wind speed. The specific humidities of the air in contact with the sea surface, q_0, and at 10 m or bridge level, q_{10}, were computed according to

$$q \approx \varepsilon e/P \qquad (4.7)$$

where ε is the known ratio (a constant equal to 0.622) of the molecular weight of water vapor to the molecular weight of dry air, e is the vapor pressure, and P is the barometric pressure. For this calculation the variation in P is negligible and so a constant value of 101325 pascals (1013.25 mb) was assigned. The calculation of e at 10 m is as indicated for the radiative heat loss calculation (Eq. 4.4). To calculate e at the sea surface, the saturation vapor pressure over pure water was computed from a formula given by Murray (1967) and reduced by two percent to account for the effect of salinity (Miyake, 1952).

Seasonal cycles of the heat exchange components within the four areas indicated in Fig. IV.1 and at Ocean Weather Station K, produced from the time series constructed according to the constant exchange coefficient versions of Eqs. 4.3 to 4.7 are illustrated in Fig. IV.8. Low frequency nonseasonal aspects of the various time series of net atmosphere-ocean heat exchange are illustrated in Fig. IV.9, where the net results of employing the constant exchange coefficient formulations are shown as a solid line and those of employing the variable coefficient formulations are shown as fine dashes. A strong similarity between the results of the constant and variable coefficient formulations is apparent, even in these highly smoothed (12-month running mean) representations where the degree of correlation is substantially lower than in the relatively more variable raw and 12th-differenced series. Because of the strong similarity in the two series and corresponding similarity in the modelling results, only the results of tests using the series computed according to the constant exchange coefficient formulations are analyzed in the discussions to follow.

As in the previous section, the dependent variable series (in this case the change of SST within a given month) and the various explanatory series were all transformed to 12th-differences in order to remove long term linear trends and the annual periodicities, which

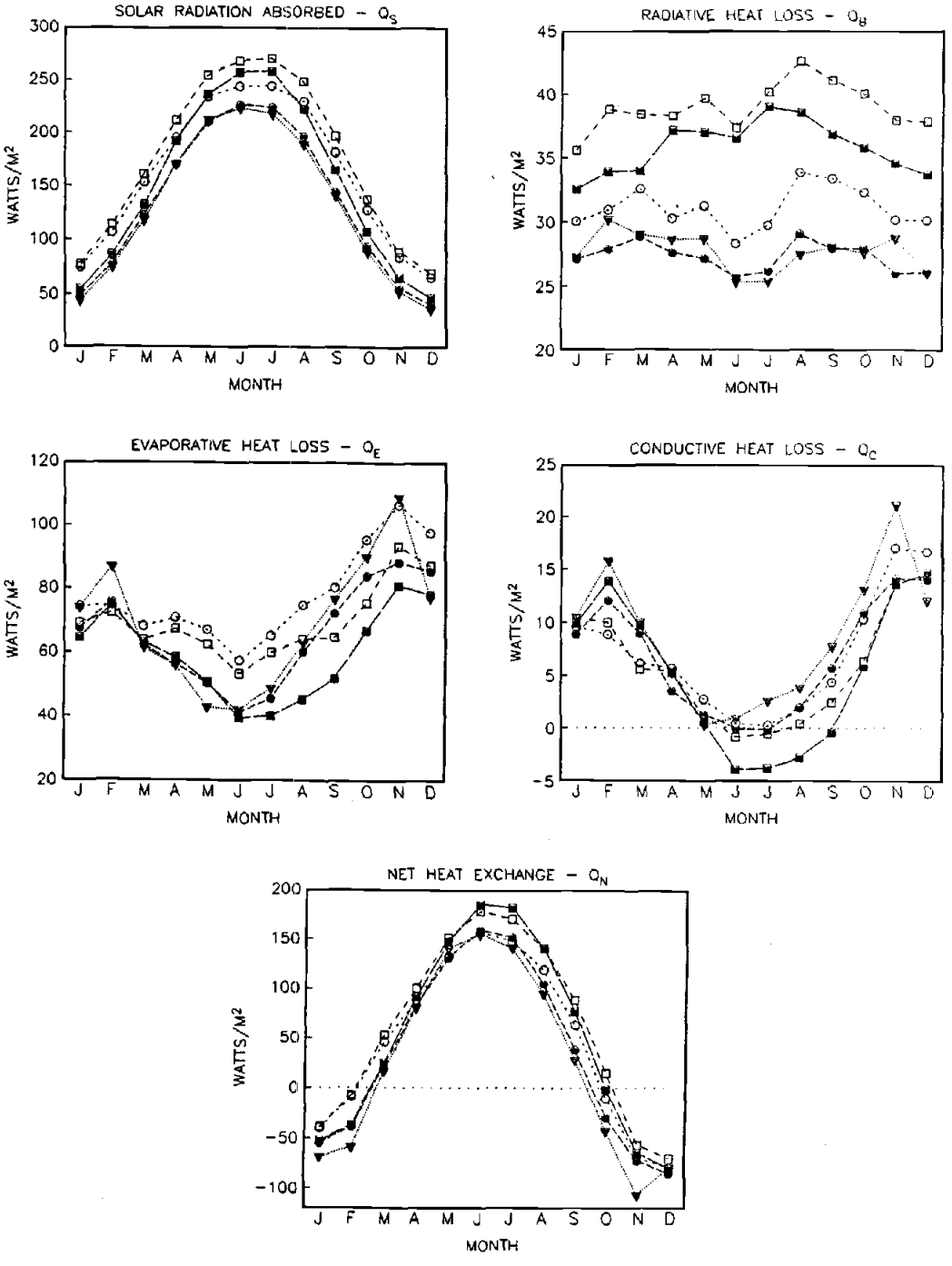

Figure IV.8. Seasonal cycles (long term mean monthly values) of components of atmosphere-ocean heat exchange at the sea surface. Units are watts m^{-2}. Square symbols indicate values for the coastal areas, the filled squares for the northerly one (area 'A') and the open squares for the southerly one (area 'B'). Circular symbols indicate values for the offshore areas, the filled circles for the northerly one (area 'C') and the open circles for the southerly one (area 'D'). The triangles indicate values at Ocean Weather Station K.

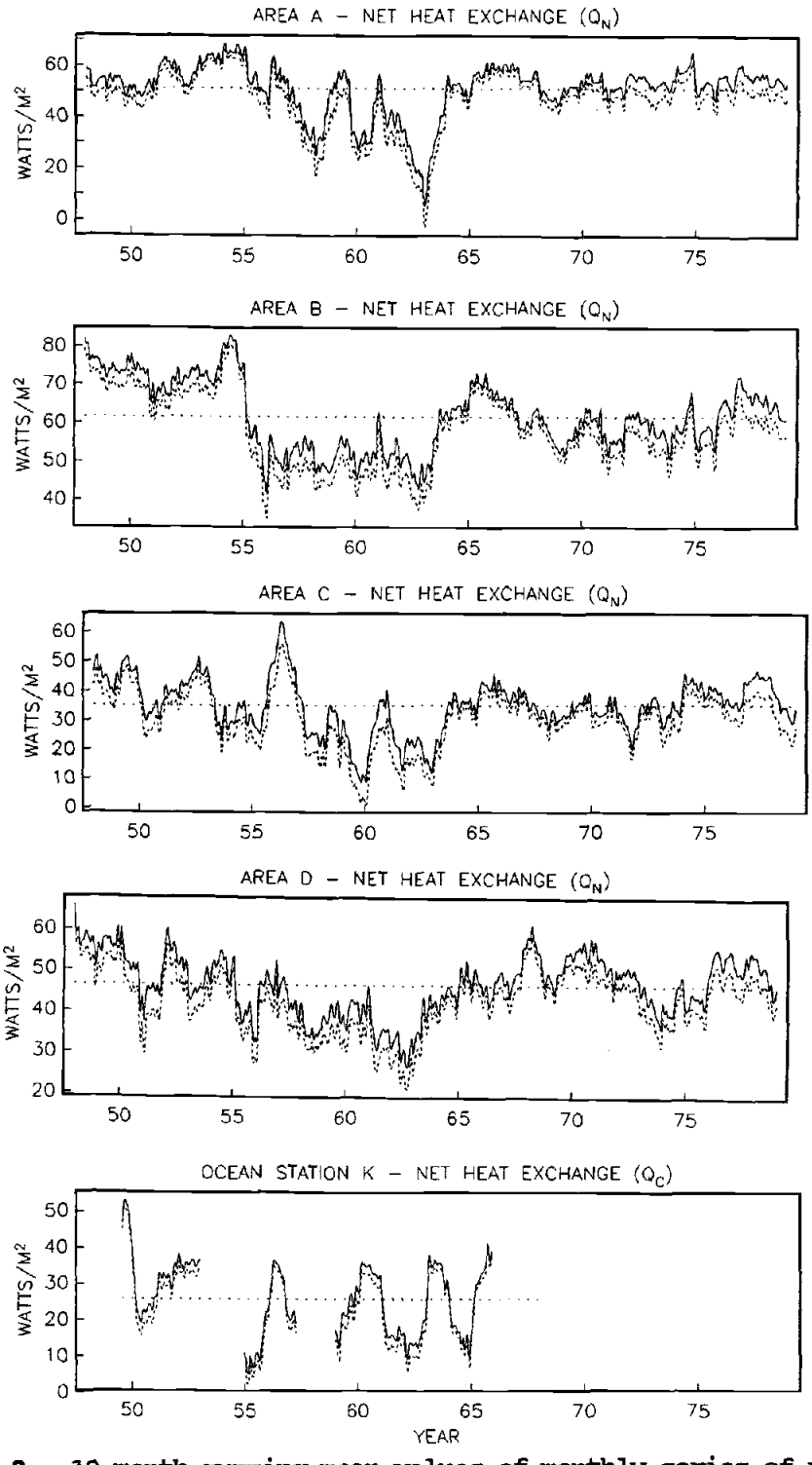

Figure IV.9. 12-month running mean values of monthly series of net atmosphere-ocean heat exchange (Q_N). Units are watts m^{-2}. The solid line denotes the results of the constant exchange coefficient formulations for Q_E and Q_C; the dashed line denotes the results of the variable exchange coefficient formulations which depend on wind speed and atmospheric stability.

might artificially amplify or even interfere with empirical indications of causal linkages. In this section, we are able to construct dependent variable series for the offshore areas as well as the coastal areas, and so stepwise regression models were constructed for each of the four areas shown in Fig. IV.1.

When the contemporaneous monthly SST change in one of the adjacent areas was included as an explanatory variable, it invariably entered first in the stepwise model-building process, explaining up to fifty percent of the variance in monthly SST change in the area of interest. The indication therefore is that a substantial portion of the process of sea surface temperature evolution occurs on spatial scales which are larger than the 5-degree quadrangles on which this analysis is focused.

This suggests events of the "El Nino" type, which are well known in the eastern Pacific and have also been reported in the eastern atlantic (e.g., McLain, Brainard, and Norton, 1985; Shelton et al., 1985), or coastal trapped wave phenomena (e.g., Allen, 1975; Smith, 1978; Picaut, 1985). Little relationship was found with monthly mean coastal sea level that would indicate a strong El Nino linkage. However since the propagating wave model would predict increasing seasonally-adjusted sea level during periods of nonseasonal temperature increase, the more proper way to investigate such a linkage would be to use

the within-month sea level change rather than sea level itself as the explanatory variable. Unfortunately, because of the direct physical linkage of sea temperature to steric height, any empirical relationship so demonstrated would merely serve to confirm this basic linkage of SST to coastal sea level, already demonstrated in the previous section, rather than yield independent information concerning coastal trapped wave propagation. In the models where the sea surface temperature change in one of the adjacent areas was retained as an explanatory variable, Q_N dropped from its usual position of most important of the explanatory variables to a much lower priority position; this indicates that the nonseasonal monthly variation in Q_N tends to be of rather large scale itself, thus accounting for some of the shared variation in nonseasonal temperature evolution among the adjacent 5-degree areas.

Therefore, the present discussion will focus on the very local aspects of nonseasonal SST evolution. The primary explanatory variables upon which the analysis is based are the local estimates of: (1) net atmosphere-ocean heat exchange, Q_N, which is the sum of the various radiative, conductive, and evaporative processes through which sea surface temperature is altered at the air-sea interface; (2) meridional (alongshore) wind stress, τ_y, as an index of coastal upwelling intensity or of onshore/offshore advection of sea surface temperature

pattern by the associated Ekman transport, etc.; (3) zonal wind stress, τ_x, as an index of advection of sea surface temperature via meridional Ekman transport; (4) turbulent mixing index, w^3, as an index of surface cooling by erosion of subsurface temperature structure; (5) wind stress curl, CURL, as a measure of vertical displacement of near surface temperature structure via Ekman pumping or (very tentatively) as an indication of tendency for meridional flow variations to be in "Sverdrup balance".

Results of stepwise regression analyses of the nonseasonal relationships of these variables to sea surface temperature evolution in the four 5-degree areas (shown in Fig. IV.1) are presented in Tables IV.22 to IV.25. Q_N is by far the most important explanatory variable in all four cases, for which all the data in a given case are strictly independent from any data used in any of the other three cases (except for the CURL variable, which shares some data among areas but which turns out consistently to be a very minor factor). The portion of the variance explained by Q_N is largest in the coastal areas, probably because the greater observational data base affords relatively reduced sampling error in the various component estimates. The other independent variables tend to increase the r^2 of the models only minimally, although τ_x meets significance criteria ($p<.05$) in both near-coastal areas, and τ_y is significant in area 'A'.

Table IV.22. Summary of stepwise regression analysis of monthly sea surface temperature change versus the variables Q_N, τ_y, τ_x, w^3, and curl, in area 'A'.

Step	Entering Variable	Mult. r2	Sig. of Model	Beta Wt. in Full Model
1	Q_N (P<.00001)	.318	P<.00001	.43 (P<.0001)
2	τ_y (P=.025)	.331	.00001	.22 (P=.0008)
3	τ_x (P=.027)	.343	.00001	-.12 (P=.06)
4	CURL (P=.057)	.352	.00001	-.10 (P=.07)
5	w^3 (P=.36)	.354	.00001	-.06 (P=.36)

Table IV.23. Summary of stepwise regression analysis of monthly sea surface temperature change versus the variables Q_N, τ_y, τ_x, w^3, and curl, in area 'B'.

Step	Entering Variable	Mult. r2	Sig. of Model	Beta Wt. in Full Model
1	Q_N (P<.00001)	.437	P<.00001	.63 (P<.0001)
2	τ_x (P=.010)	.447	.00001	-.10 (P=.03)
3	CURL (P=.11)	.451	.00001	.05 (P=.21)
4	τ_y (P=.43)	.452	.00001	.04 (P=.53)
5	w^3 (P=.54)	.453	.00001	-.03 (P=.54)

Table IV.24. Summary of stepwise regression analysis of monthly sea surface temperature change versus the variables Q_N, τ_y, τ_x, w^3, and curl, in area 'C'.

Step	Entering Variable	Mult. r2	Sig. of Model	Beta Wt. in Full Model
1	Q_N (P<.00001)	.169	P<.00001	.43 (P<.0001)
2	τ_x (P=.41)	.171	.00001	-.10 (P=.23)
3	CURL (P=.56)	.172	.00001	-.05 (P=.45)
4	w^3 (P=.50)	.174	.00001	.07 (P=.47)
5	τ_y (P=.81)	.174	.00001	-.02 (P=.81)

Table IV.25. Summary of stepwise regression analysis of monthly sea surface temperature change versus the variables Q_N, τ_y, τ_x, w^3, and curl, in area 'D'.

Step	Entering Variable	Mult. r2	Sig. of Model	Beta Wt. in Full Model
1	Q_N (P<.00001)	.240	P<.00001	.56 (P<.0001)
2	τ_x (P=.37)	.242	.00001	-.07 (P=.23)
3	w^3 (P=.38)	.244	.00001	-.06 (P=.45)
4	τ_y (P=.53)	.245	.00001	-.05 (P=.47)
5	CURL (P=.59)	.245	.00001	-.03 (P=.81)

The lack of capacity of the indicators of the processes other than Q_N to substantially reduce the unexplained variance in nonseasonal SST evolution is at least partially due to the fact that they tend to be substantially correlated with Q_N (Table IV.26). We might have expected τ_y to have been important in area 'B' where evidence of summer upwelling tends to be highly evident in the SST pattern (Wooster, et al., 1976). However, we note (in Table IV.26) that the coefficient of correlation between τ_y and Q_N is the square root of 0.65, i.e., r = .81. Obviously, most of the nonseasonal variability in τ_y is already represented in Q_n. In fact, the least correlated (with Q_N) of the other explanatory variable series is τ_x; this may explain the rather unexpected result that τ_x, which we assume represents temperature advection in the meridional Ekman transport field tends to enter the stepwise analysis procedure before indicators of such processes as wind induced vertical mixing (w^3), Ekman pumping (CURL), and coastal upwelling (τ_y).

In view of this intercorrelation, the coefficients of univariate correlation of 12th-differenced monthly SST change with the various explanatory variables in each area are presented in Table IV.27. Certainly, the roles of τ_y and w^3, relative to τ_x, are seen in a completely different light when they are not submerged by their covariation with Q_N, as in the stepwise regression analysis. Note that the

Table IV.26. Correlation coefficients between 12-differenced monthly values of net ocean -atmosphere heat exchange, Q_N, and 12-th differenced monthly values of various other maritime data-based variables, by area. Correlation coefficients significant at the .05 level are followed by an asterisk; those significant at the .01 level are followed by two asterisks.

	A	B	C	D
τ_y	.42**	.65**	.50**	.72**
τ_x	-.02	.06	-.13*	.13*
w^3	-.49**	-.52**	-.47**	-.62**
CURL	.01	-.05	-.29**	-.24**

Table IV.27. Correlation coefficients between 12th-differenced monthly values of sea surface temperature change and 12th-differenced monthly values of the various other maritime data-based variables, by area, and with sea level, corrected for atmospheric pressure variation, at Vigo and Cascais respectively. Correlation coefficients significant at the .05 level are followed by an asterisk; those significant at the .01 level are followed by two asterisks.

	A	B	C	D
τ_y	.37**	.46**	.22**	.34**
τ_x	-.10	-.06	-.07	.02
w^3	-.32**	-.41**	-.21**	-.29**
CURL	.02	.01	-.15*	-.15*
Q_N	.56**	.66**	.41**	.49**
Vigo	.16	.28**	.11	.03
Cascais	.06	.14*	-.05	-.01

signs of the correlation coefficients are correct for the processes envisioned (i.e., negative correlation of SST increase with turbulent mixing, and positive correlation with northward tendency in alongshore stress, implying decreased coastal upwelling). It is also interesting that CURL exhibits a significant univariate correlation with SST change in the two offshore areas, 'B' and 'C', where one might expect cooling related to Ekman pumping to be more important than in the near-coastal areas; again the sign is correct (negative) for these significant correlation coefficients: i.e., positive curl yields upward Ekman pumping leading to SST decrease. Sea level is significantly positively correlated with SST increase in area 'B'; this is the correct sense for high sea level at the coast, corresponding to an upward slope of sea level from offshore toward the coast and associated northward alongshore geostrophic flow, to contribute to warm temperature advection.

The highest univariate correlation shown in Table IV.27 is, of course, with Q_N. The correlation is broken down by month in Table IV.28. In the near-coastal areas, the correlation appears lowest during spring and summer, when coastal upwelling related processes may compete significantly with the sea surface heat exchange processes. In the offshore region the pattern is somewhat the opposite, although the reduced number of data points in the

Table IV.28. Inferred mixed layer depths based on slopes of regressions of monthly temperature change versus monthly index of net atmosphere-ocean heat exchange (series were transformed to 12th-differences before analysis). Corresponding correlation coefficients are shown in parentheses; those not significant at the .05 level are marked with a minus sign following the number.

	Area 'A'	Area 'B'	Area 'C'	Area 'D'
Jan	40m (.82)	43m (.71)	121m (.23-)	209m (.16-)
Feb	124m (.45)	64m (.69)	155m (.25-)	298m (.19-)
Mar	310m (.15-)	51m (.51)	105m (.28-)	63m (.44)
Apr	105m (.20-)	53m (.40)	40m (.51)	42m (.52)
May	44m (.41)	49m (.45)	128m (.16-)	53m (.42)
Jun	35m (.33-)	25m (.60)	18m (.54)	25m (.65)
Jul	23m (.35-)	13m (.78)	14m (.68)	25m (.57)
Aug	19m (.67)	18m (.63)	18m (.69)	25m (.67)
Sep	18m (.74)	17m (.74)	48m (.62)	24m (.73)
Oct	21m (.77)	17m (.88)	34m (.60)	42m (.61)
Nov	23m (.89)	27m (.79)	188m (.24-)	52m (.57)
Dec	54m (.71)	33m (.78)	74m (.46)	58m (.67)
Full Series	38m (.56)	30m (.66)	56m (.41)	51m (.49)

separate monthly samples makes the results rather noisy; a rather stable thin surface layer during summer may contribute to enhanced effects of sea surface exchange processes on SST change.

Also in Table IV.28 are listed the hypothetical mixed layer depths which would explain the slopes of the regressions (i.e., the depths to which the nonseasonal variation in heat input would have to be mixed to yield the observed relationship to nonseasonal variation in SST evolution). The values appear generally reasonable, being deepest offshore and to the north during the winter season, and shallowing greatly during the summer.

Levitus (1982) has analyzed subsurface temperature and sigma-t by 5-degree squares for the world ocean. He has suggested two mixed layer depth criteria to approximate the large scale mixed layer depth distribution from his horizontal fields: (1) a temperature criteria based on a linear interpolation to find a depth where the temperature is lower than the surface temperature by 0.5 degress Celsius, and (2) a similarly applied sigma-t criteria where the sigma-t difference from the surface value was 0.125. Values so extracted from Levitus' tables are presented in Table IV.29; his 5-degree squares are offset 2 degrees westward (offshore) from the areas used in our analysis. The seasonal and geographical aspects of the mixed layer depth values derived from our empirical analysis of the

nonseasonal SST change corresponding to nonseasonal variations in atmosphere-ocean heat exchange tend to lie within the general range of Levitus' analysis of actual subsurface structure.

Table IV.29. Mixed layer depth values produced from the subsurface stucture analyses of Levitus (1982). Areas marked 'A2', 'B2', 'C2', and 'D2' are 5-degree areas at the same latitudes but offset two degrees of longitude to the west (offshore) from the 5-degree areas used in our analysis (Fig. IV.1). First number indicates the value according to Levitus' "temperature criterion" and the following number in parenthesis indicates the value according to his "sigma-t criterion".

Season	Area 'A2'	Area 'B2'	Area 'C2'	Area 'D2'
Winter:	176m (269m)	110m (206m)	190m (238m)	120m (181m)
Spring:	17m (14m)	20m (13m)	19m (16m)	16m (7m)
Summer:	26m (10m)	27m (16m)	24m (22m)	26m (16m)
Fall:	65m (55m)	61m (61m)	72m (63m)	58m (74m)

V. WIND-RELATED TIME SERIES PRODUCED FROM TEMPORALLY-AVERAGED OR SPATIALLY-SMOOTHED METEOROLOGICAL ANALYSES

V.1. Introduction

As discussed briefly in Section IV.3 with respect to wind stress curl, time series indicators of wind-related processes have sometimes been produced from the analyzed products which are generated by national meteorological agencies as a basis for routine weather forecasting activities. This procedure offers advantages, at least conceptually, in that the meteorological analysis methodologies allow for spreading data temporally and spatially in a physically realistic manner, using dynamical or statistical models. Thus observations from previous or subsequent synoptic samplings and from neighboring locations may contribute to a better estimate of the actual value at a gap in data coverage than obtainable via simple interpolation. The analysis methodologies also customarily incorporate elaborate error-checking procedures based on iterative tests of conformity of observations to physical reality as defined by the models. In addition, large scale analysis of wind observations may be improved by incorporating barometric pressure data through the geostrophic coupling which is strong enough in extratropical regions to constitute additional information

on the wind field.

Thus we might expect significant improvement in estimates through these procedures, compared to simple areal averages of reports. Indeed, the analysis procedures have been demonstated to be quite skillful in defining variability on the energetic synoptic scales for which they have been designed. However, their degree of skill in defining variability on interyear time scales, where the variations of interest are lower level residuals of higher amplitude synoptic (i.e., storm events, etc.) and seasonal scale variability, remains unclear (Bakun, 1986).

Coastal upwelling indices (Bakun, 1973, 1975), representing an estimate of alongshore wind stress and associated offshore-directed Ekman transport, have been used in various oceanographic and biological studies of the near-coastal regions of the northeastern Pacific Ocean. These are computed from analyzed fields of surface atmospheric pressure, which also incorporate available wind speed and direction reports as geostrophically-equivalent pressure gradients (Holl and Mendenhall, 1972), obtained from the U. S. Navy's Fleet Numerical Oceanographic Center (FNOC). The computations are performed on a 3-degree latitude/longitude grid, utilizing central difference derivatives spanning three grid intersections. A simplified approximation to the effects of the earth's frictional boundary layer is applied, involving a rotation of the

geostrophic wind vector 15 degrees to the left and a reduction in magnitude of 30 percent.

Two versions of these upwelling index time series are presently in use. "Monthly mean upwelling indices" (Bakun, 1973), with time series beginning in 1946, are computed directly from monthly means of synoptic data fields. Use of monthly mean data was dictated by the varying frequencies of, and origins of, analyzed synoptic surface pressure/wind fields over the period previous to 1967 (when a consistent set of four-per-day machine-generated analyzed synoptic data fields was initiated as an operational product at FNOC). Because the computation of stress from wind is nonlinear (Eq. 2.3), it was felt that performing the calculations on synoptic data and averaging later might introduce more serious time series inhomogeneities than if the computations were made after the higher frequency variability had been smoothed by monthly averaging. The procedure was checked against corresponding series of monthly means of computations from synoptic data during the period since 1967; the results were highly correlated (Bakun, 1973). This series however remains basically a parameterization of the monthly mean wind field rather than of the monthly mean wind stress field, and thereby subject to distortion when there is substantial inter-month variability in the within-month variance of wind velocity.

A second set of upwelling index time series, "daily

and weekly upwelling indices" (Bakun, 1975) has been computed for the period since 1967 in the more strictly correct manner, as daily and weekly means of 6-hourly computations from synoptic data

In the late-1970's, FNOC developed a time series of 6-hourly synoptic marine wind analyses, computed according to a consistent analysis algorithm, for the entire period since 1946. The computation scheme was on a larger scale than in the "Bakun" upwelling indices, using derivative approximations covering five grid intersections in each direction and an apparently higher degree of smoothing in the information-blending algorithms. A more complex boundary layer approximation, featuring an adjustment for atmospheric stability based on the underlying SST field, was employed. Also a correction for streamline curvature was applied to the geostrophic wind. Under the direction of Pacific Fisheries Environmental Group, the nonlinear computations needed to produce stress estimates and the "w^3" wind-mixing index were performed synoptically on these fields and then averaged by 10-day periods (Caton et al., 1978). The resulting series are herein refered to as the 'MII' series.

Although the MII series is conceptually superior to the Bakun (1973) series, constituting proper averages of synoptic computations, several puzzling features have prevented its being advanced as a replacement for the

earlier (Bakun, 1973; Mason and Bakun, 1986) time series. In some cases the synoptic scale series values, on which the MII series is based, have not matched actual observations in near-coastal regions as well as do the smaller spatial-scale computations of Bakun (1975). Also, in producing the series on which the MII series was based, no actual observations located on the continents were incorporated; continental data was supplied by gridpoint values from older analysis fields, leading to the possibility that the pressure gradients crossing the continental boundary, which serve to define the alongshore stress in the coastal region, may be in some degree artificial. In addition, the (sometimes) significant differences in the indications of interyear variability presented by the Bakun (1973) series and the MII series have been larger than the differences between the Bakun (1973) calculations from mean data and the Bakun (1975) series of computations from synoptic data; this implies that the differences found are basic to the analysis methods rather than due to the compution from previously averaged data in one case and not in the other.

Wooster (in prep.) cites a dramatic increase, off the Iberian Peninsula, in April through September mean values of monthly upwelling index values produced according to the procedures of Bakun (1973). Dickson et al. (1986) cite Wooster's findings and note a correspondence to a long term

decline in both phytoplankton and zooplankton biomass in ocean areas around the British Isles. In investigating the climatic situation, they find a progressive intensification of a pressure anomaly ridge over the eastern Atlantic between the 1950's and 1970's, associated with increased northerly winds and increased frequency of storm conditions. They suggest that this increased storminess may have delayed and shortened the growing season for phytoplankton according to Sverdrup's (1953) mechanism, with effects propagating up the food web.

Dickson et al. also cite an increasing trend in upwelling index values off Morocco at 28° N lat, during the same period, reported by Belveze and Erzini (1983). Interestingly, Belveze and Erzini also show a measured wind signal from a coastal station (Essaouira), located at about 32° N lat, indicating a rather linear decrease in average wind speed by a factor of more than two, over the period 1950 to 1980. A decrease in wind speed by a factor of two would imply a decrease in wind stress and corresponding coastal upwelling intensity by a factor of four (Eq. 2.3). Such a large, sustained long term change in upwelling intensity could be expected to drastically alter oceanographic conditions and perhaps completely reorganize the biological structure of the ecosystem, and so questions as to how believable are these various signals, and which of them to choose when they disagree, are certainly crucial

to their appropriate employment in studies of effects of climate variation on the ocean and the associate biota.

In this chapter we attempt to build on some of the findings of the Chapter IV in order to develop improved insight as to how, and in what situations, to choose among series of this type. Because of the dramatic nature of the trend reported by Dickson et al., (1986), the April through September mean values are used extensively for visual illustrations of aspects of long-period interyear variability.

V.2 Alongshore Wind Stress

April through September mean values of the alongshore stress estimates discussed in Chapter IV are displayed, for the four independent areas 'A', 'B', 'C', and 'D', in Fig. V.1. The location of the upwelling index computation examined by Wooster (in prep.) and Dickson et al. (1986) was at 42 N lat, i.e, within area 'A'. In general, the long term increase in southward stress (increased negative value in the figure) noted by Wooster is apparent in all four independent series. However, major differences between areas are evident. For example, while 1963 appears as a particularly strong year for southward stress in all four areas , 1961 appears even stronger in area 'D' but as a particularly weak year in area 'C'. 1958, which stands

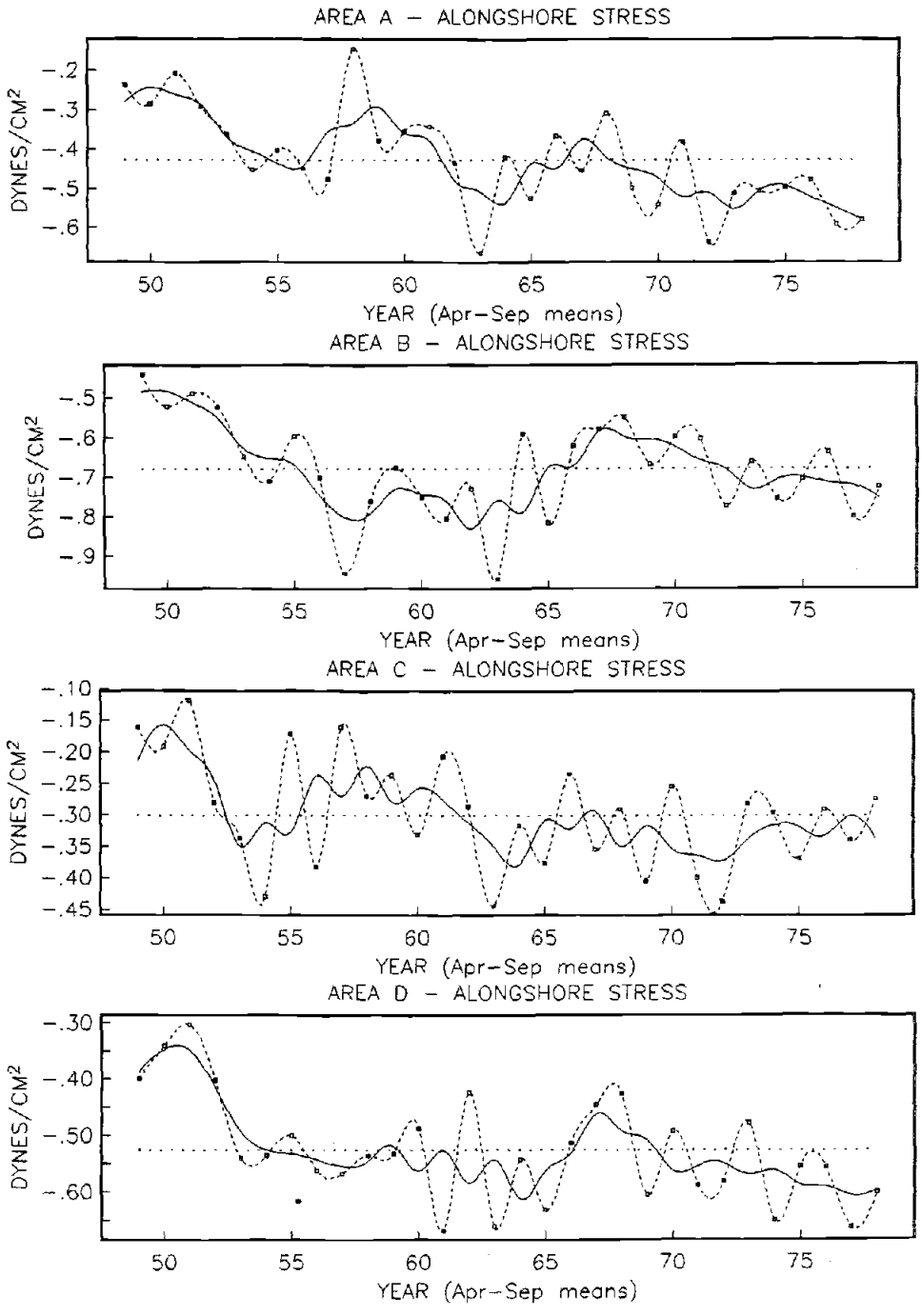

Figure V.1. April to September average values of alongshore stress (dynes cm^{-2}; positive northward) produced from monthly summaries of computations from individual maritime reports. The solid line indicates the 3-year running mean.

out as an extremely weak year for spring-summer southward stress in area 'A', is indicated as being rather normal in the other nearby areas. 1957, which appears as one of the strongest years in area 'B' appears as one of the weakest years in area 'C'. These differences in indications of extreme years tend to control the shape of some of the longer period variations defined in the smoothed 3-year running mean presentation. For example, the differences between the indications for the years 1957 and 1958 in areas 'A' and 'B' tend to control much of the difference between the smoothed low frequency presentations for the two areas.

Several sets of time series computed from analyzed wind/pressure fields were prepared, with the computation schemes being centered at the long term mean positions of reports in areas 'A', and 'B', respectively, in order to make them as directly comparable as possible to the stress series produced from maritime report summaries in those areas. One set, herein labled 'mm', is computed at each of the two locations from monthly mean data fields, following the "monthly coastal upwelling index" procedures of Bakun (1973). Another set, labeled '6hr', is compiled as monthly means of computations from 6-hourly synoptic data fields, according to the procedures of Bakun (1975); this set is available only for the period since 1967. A third set, herein labeled 'MII', is produced from the data series

described by Caton, et al. (1978), available up to 1977. In this chapter as in the previous chapter, whenever correlation is discussed prior application of the 12th-difference transform is implied.

In both areas 'A' and 'B', the series which is most highly correlated with the series produced from areal summaries of maritime reports is the '6-hr' series of means from 6-hourly computations (Table V.1). The 'MII' series is very nearly as highly correlated; in fact the correlation between the '6-hr' and 'MII' series is equally high (r=.96) in both areas. This high degree of correlation is perhaps not surprising since both represent monthly means of four-per-day computations from gridded synoptic data fields.

In the previous chapter, the alongshore stress was shown to be significantly related to nonseasonal variation in coastal sea level. Table V.1 shows that in area 'A', both the 'mm' and 'MII' series produce a higher correlation with coastal sea level than does the series of areal summaries of maritime reports tested in Chapter IV (there was no similar test of the '6-hr' series for area 'A' since there was no time-series overlap with the local 'Vigo' sea level series); the 'MII' series produced the highest correlation of the two. In area 'B', all the series computed from analysed data fields were more highly correlated with nonseasonal sea level variation than were the areal summaries of maritime reports; in this case the

Table V.1. Linear correlation coefficients among various 12th-differenced series of monthly estimates of alongshore stress and SST evolution in areas 'A' and 'B' (Fig.IV.1), and of sea level at Vigo and Cascais. τ_y: areal summary of maritime wind reports; τ_{ymm}: computed from monthly mean pressure/wind analysis; τ_{yMII}: from 'M.I.I.' marine wind summaries; τ_{y6hr}: monthly means of computations from 6-hourly synoptic pressure/wind analyses; "Vigo" and "Cascais": monthly mean sea level at these stations corrected for local atmospheric pressure; "dSST": change of areal averaged sea surface temperature from beginning to end of a month.

Area 'A'

	τ_y	τ_{ymm}	τ_{yMII}	τ_{y6hr}
τ_{ymm}	.68			
τ_{yMII}	.81	.89		
τ_{y6hr}	.87	.90	.96	
Vigo	.41	.45	.55	--
dSST	.37	.19	.33	.17

Area 'B'

	τ_y	τ_{ymm}	τ_{yMII}	τ_{y6hr}
τ_{ymm}	.78			
τ_{yMII}	.84	.88		
τ_{y6hr}	.86	.88	.96	
Cascais	.43	.48	.49	.55
dSST	.46	.36	.35	.24

relationships with the 'mm' and 'MII' series were essentially equivalent, and that with the '6-hr' series was highest of all.

In summary, the indication is that the signals computed from gridded data fields derived from meteorological analysis produce a higher degree of apparent relationship with local coastal sea level than do those based on areal summaries of maritime data. A conclusion might be that use of analyzed meteorological data fields as input data indeed produces a more accurate signal of the actual alongshore stress. However, the facts that the sea level values have been corrected for atmospheric pressure (i.e., for the inverted barometer effect) and also that atmospheric pressure gradients are incorporated in the basic data fields on which the sress estimates are based, leads one to wonder if there could be some associated non-independence in the two series interfering in some non-obvious manner with this analysis.

With this caution in mind, we nevertheless note that the '6-hr' series (i.e., Bakun, 1975) was the most effective of the series in "explaining" nonseasonal coastal sea level variation; unfortunately this series is not available previous to 1967. Between the two longer series which are available since 1946, the 'MII' series (Caton et al., 1978) appeared in one of the two cases to be more effective than the 'mm' series (Bakun, 1973).

In the case of the relation to SST change, all of the series produced from analyzed meteorological fields produced lower degrees of correlation (Table V.1) than did the series of areal summaries of reports. In area 'A', the 'MII' series did much better than the 'mm' series; in area 'B' they were roughly equally effective. In both areas, the short '6-hr' series produced the lowest degrees of correlation of all, possibly due to artifacts of the particularly small sample sizes. Thus we are led to the opposite conclusion to that reached with respect to coastal sea level; i.e., that analyzed meteorological fields are poorer representations of alongshore stress.

With respect to both coastal sea level and SST change the 'MII' series has appeared to be superior to the 'mm' series in area 'A'; the two series seem to have roughly equivalent "skill" in area 'B'. A possible explanation is that the more southerly location may be more more typical of a standard eastern boundary upwelling region, where the wind stress tends to be highly constrained to the alongshore direction by coastal topography and the temperature contrast between land and ocean. This situation apparently leads to the high degree of correlation between series computed from monthly mean input data and series of monthly means of synoptic computations found in the California Current coastal region by Bakun (1973); in the northeast Pacific, the correlation tends to fall off dramatically

with distance from the coast (Bakun, unpublished study). Area 'A', which lies directly adjacent to the interruption in the meridional coastal barrier at Cape Finisterre, may be more subject to large variations in the intra-month wind variance, related to passages of rotational storm systems.

April through September mean values of the various series of alongshore stress estimates for area 'A' are displayed in Fig. V.2. In general, the previously-discussed long term increase in southward stress is apparent in all of the displayed series. Certain details are also consistent; for example, the extreme minimum in southward stress in 1958 and the strong maximum in 1972 are apparent in all the series. However, the extreme maximum shown for 1963 in the series of areal summaries of maritime reports, is absent in the various series based on meteorological analyses. In general there nevertheless does seem to be a rather consistent correspondence in position among relative maxima and minima, if not among their magnitudes, in all the series of annual April-September values; the cases of non-correspondence in relative magnitude of the oscillations does tend to shift the peaks somewhat in the smoothed 3-year running mean series.

Very interestingly, in spite of the similarity in general long term trend and in certain shorter period features, the numerical values of the 'MII' series are widely different from those the other series. In fact,

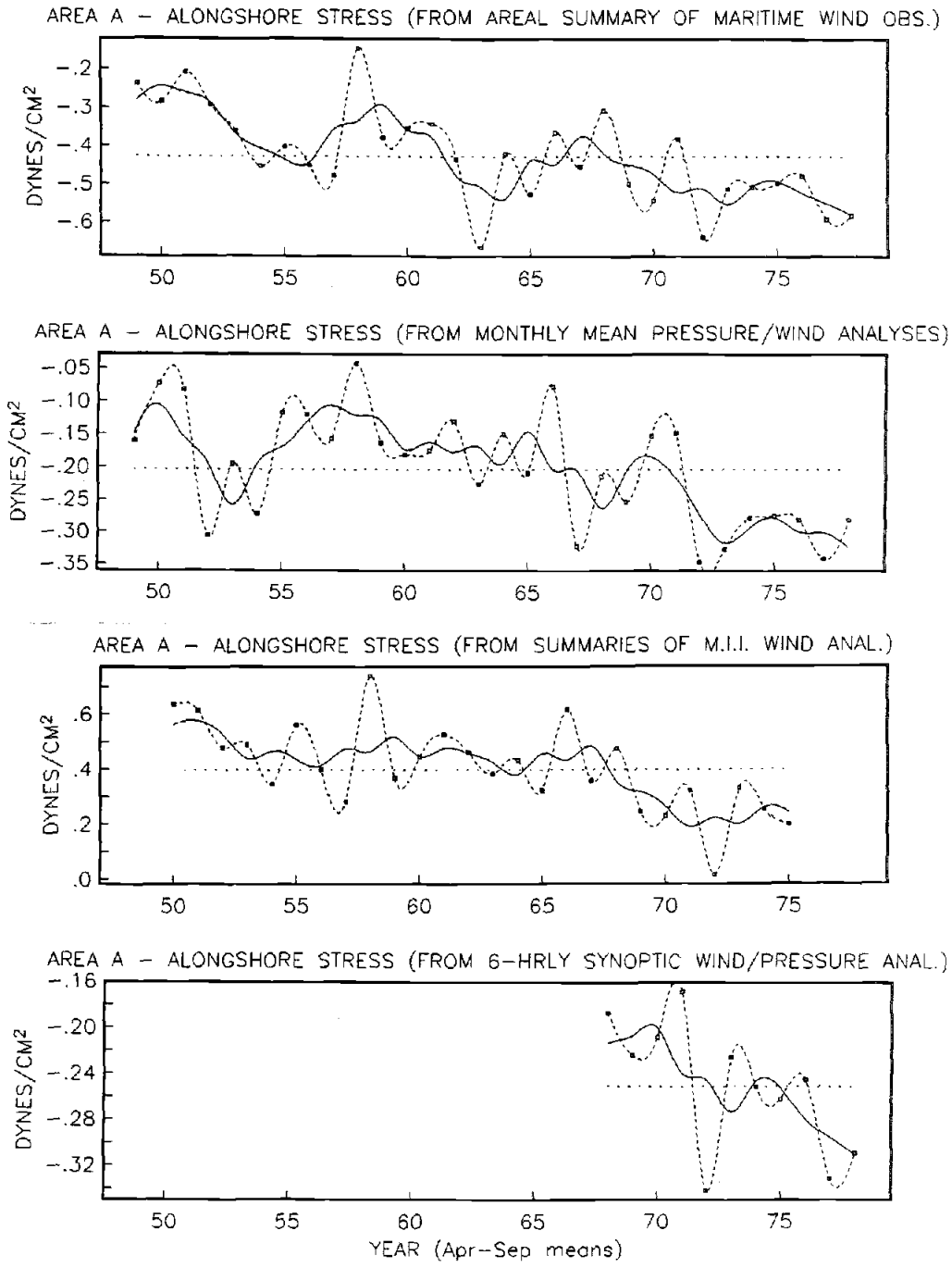

Figure V.2. April to September average values of alongshore stress (dynes cm^{-2}; positive northward) in area 'A'. *Top panel:* series of areal summaries of computations from individual maritime reports. *Second panel:* 'mm' series computed directly from monthly means of FNOC analyzed wind/pressure fields. *Third panel:* 'MII' series produced as monthly averages of computations form synoptic "M.I.I." analyzed marine wind fields. *Bottom panel:* '6hr' series produced as monthly averages of computations from synoptic FNOC analyzed wind/pressure fields. The solid line indicates the 3-year running mean.

every one of the April to September mean values in the 'MII' series is positive, indicating a northward alongshore component of wind stress, whereas all corresponding values in all of the other series are negative, indicating southward stress along the coast. Since the group of series consistently indicating average southward stress along the coast during the April to September period includes the series of averages by area of actual reports, the differing 'MII' indication is certainly an artifact.

The reason for the aberration may lie in the very large scale spatial smoothing inherent in the 'MII' series. Because the mean position of the Icelandic Low is west of that of the Azores High, the very large scale isobaric pattern in the North Atlantic (to the west and north of the study area) has a slight tilt to the north of east (Anon., 1955). The region exhibiting this tilt also contains the tightest isobaric gradients and thus the most intense geostrophic winds. The frictional boundary layer effects would deflect the surface wind to the left of the geostrophic wind, (i.e., even more toward the north). The large scale smoothing may be allowing encroachment of effects of the more energetic situation to the north and west, contaminating the local signal off the Iberian Penninsula. If this is the case, the fact that the trends and relative features match the other series as well as they do implies quite a large scale spatial continuity for

at least some major components of low frequency nonseasonal variability.

In area 'B' (Fig. V.3), there again is quite a good correspondence in the positions of the relative extrema in the unsmoothed series of annual April-September means. Very deep minima (maxima of southward stress) in 1957 and 1963 in the series of areal summaries of maritime reports are not well reflected in the series computed from meteorological analyses; the result is that in the smoothed 3-year running mean presentation the decade of 1955-65 appears as a broad trough in the maritime report series whereas it appears as a ridge in the series produced from analyzed fields. The value for 1963 stands out as a deep minima (southward maxima) in all four of the independent samples from areas "A', 'B', 'C', and 'D'; this indication is relatively lacking in the 'mm' series and totaly lacking in the 'MII' series in both areas 'A' and 'B'. The implication is that this feature, while almost certainly real (being consistent among all four areal samples), may have been quite local to the Iberian area and that its indication is progressively attenuated with the increasing spatial scales represented by the respective 'mm' and 'MII' series.

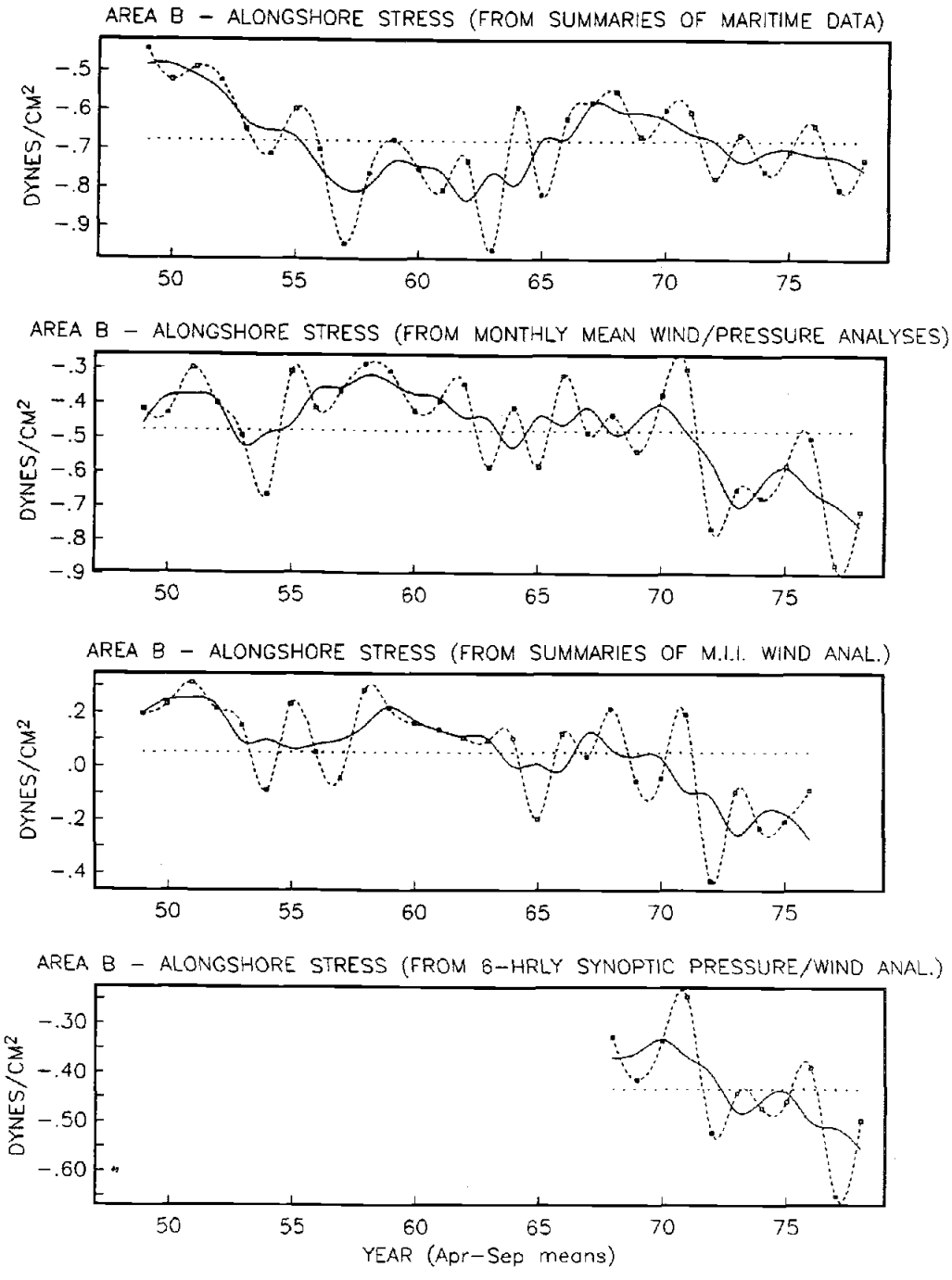

Figure V.3. April to September average values of alongshore stress (dynes cm^{-2}; positive northward) in area 'B'. *Top panel:* series of areal summaries of computations from individual maritime reports. *Second panel:* 'mm' series computed directly from monthly means of FNOC analyzed wind/pressure fields. *Third panel:* 'MII' series produced as monthly averages of computations form synoptic "M.I.I." analyzed marine wind fields. *Bottom panel:* '6hr' series produced as monthly averages of computations from synoptic FNOC analyzed wind/pressure fields. The solid line indicates the 3-year running mean.

V.3 Seasonal Patterns: Stress Versus Velocity

The inherent problem in the 'mm' series of alongshore stress estimates, which is equivalent in its manner of construction to the series of "monthly coastal upwelling indices" developed by Bakun (1973), is that they are computed from previously time-averaged data fields via a nonlinear stress law (Eq. 2.3). The proper procedure is to perform nonlinear computations prior to averaging. The 'mm' series represents a parameterization of the monthly-average resultant wind velocity rather than of the monthly-average resultant wind stress. The result is the possibility of distortion when the within-month variance may not co-vary in a consistent manner with the monthly resultant mean.

A simple illustration of such a distorted indication is provided by the long term mean seasonal cycles of wind velocity and wind stress in areas 'A' and 'B' (Fig. V.4). Note that in the southerly area,'B', the meridional components of both the average monthly resultant wind velocity and wind stress are directed southward throughout the year. However, in area 'A' the vector-averaged wind velocity turns northward during the month of January, whereas the vector-averaged stress of the wind on the sea surface does not (Fig. V.4).

The explanation would seem to be that the wind is directed northward most of the time during the month of

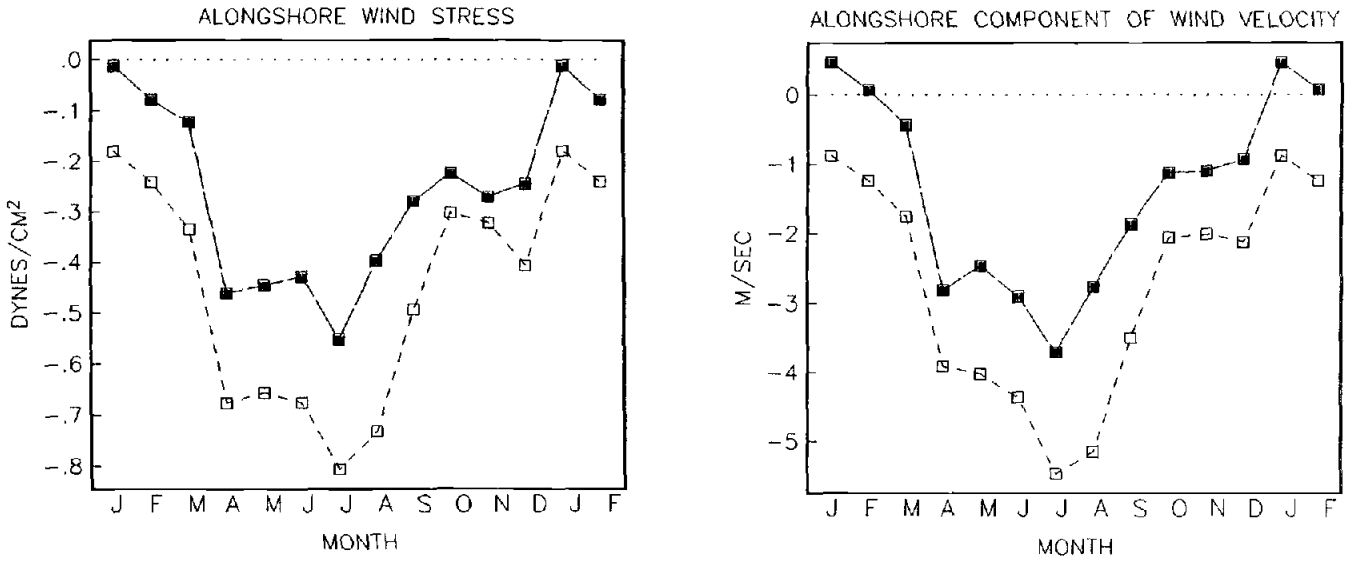

Figure V.4. Seasonal cycles (long term mean monthly values) of alongshore wind stress and wind velocity in the near-coastal areas, 'A' and 'B'. The filled symbols denote the northerly area (area 'A') and the open symbols denote the southerly area (area 'B'). *Left panel:* alongshore component of sea surface wind stress (dynes cm^{-2}, positive northward). *Right panel:* Alongshore component of wind velocity (m sec^{-1}, positive northward).

January, but the situation is broken by less frequent but more intense events of southward stress, i.e, northerly winds associated with intense storms. The effect of the intense events is amplified in the stress computation where the magnitude enters as the second power (Eq. 2.3) rather than the first power, overwhelming the more frequent lower magnitude southerly wind events.

Additional discussion of the time series relationship of wind velocity to wind stress is presented in Section V.6.

V.4 "W^3" Turbulent Mixing Index

In the "wind speed cubed" index of rate of addition of turbulent mixing energy to the ocean by the wind, the wind enters as the third power of the (scalar) wind speed. The directionality of the wind is irrelevent and high wind speed events are overwhelming in their effect on the mean.

Long period variation in this index in areas 'A', 'B', 'C' and 'D', and at Ocean Weather Station K are shown in Fig. V.5. A minor peak occurs in the early 1950's in all series, followed by a high broad irregular peak during the decade 1955-65. This peak rises to a single zenith near 1960 in area 'C' and at OWS-K, whereas it has more the character of a double peak in areas 'A', 'B' and 'D' with a minimum occurring in 1960-61. A general increase during the 1970's is broken by a strong drop near 1975 in all

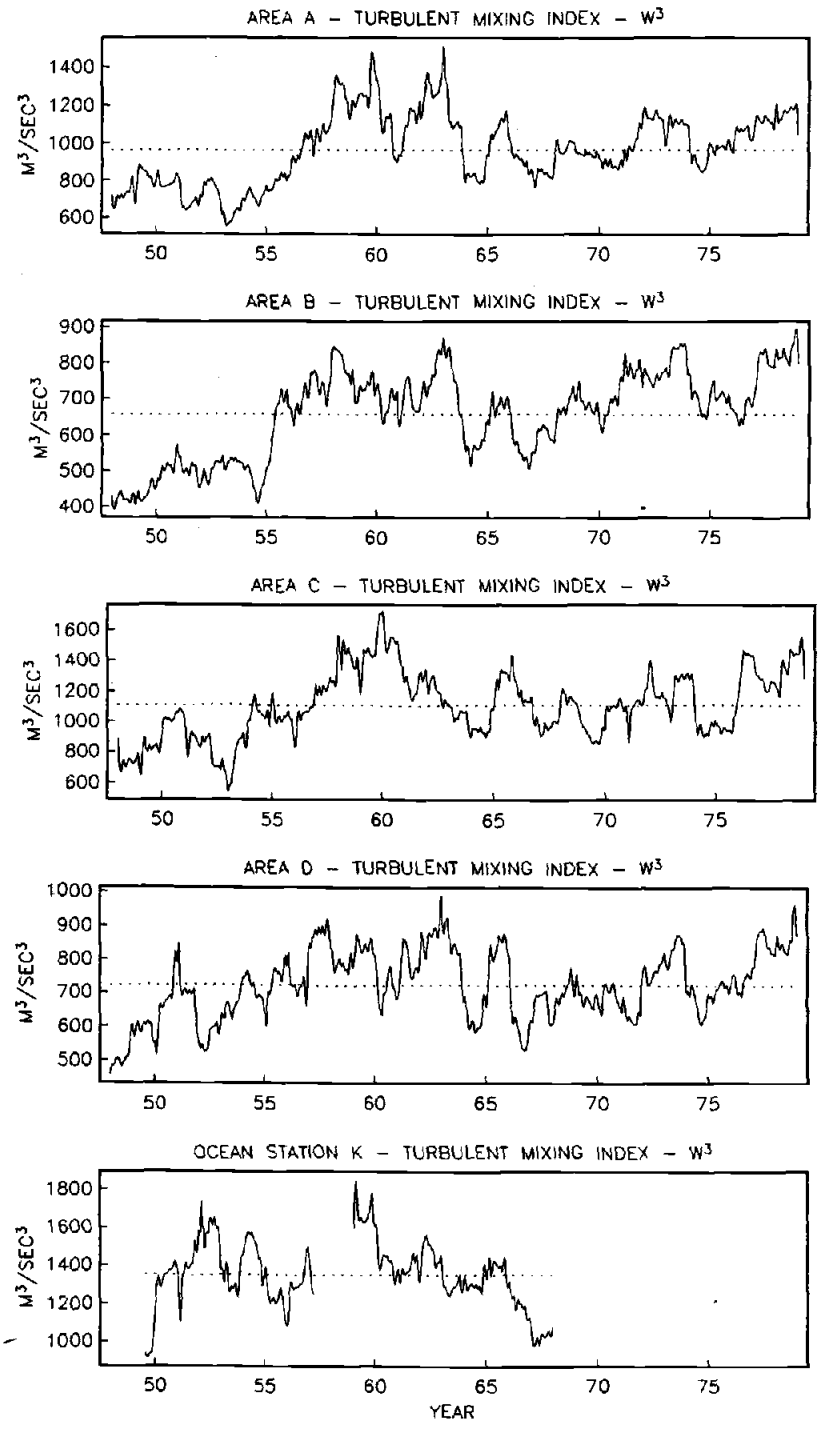

Figure V.5. 12-month running mean values of monthly series of "w^3" index of rate of addition of turbulent mixing energy to the ocean by the wind (formulated as the mean of the third power of the observed wind speeds in each monthly sample of maritime reports). Units are m^3 sec^{-3}.

series.

Series (for the area 'A' location) computed from analyzed meteorological data fields are compared to corresponding series of areal summaries of maritime reports in Fig. V.6. The differences are substantial. The broad major maxima during the decade 1955-65 is nearly lacking in the 'mm' and 'MII' series computed from analyzed data fields, although relative maxima in 1959 and 1963 are reflected. A single narrow peak in 1965-66 dominates the 'mm' series, which exhibits less resemblence to the maritime report series than does the 'MII' series. This is not surprising since the computation of the 'mm' series is from a monthly mean atmospheric pressure field representing a vector mean of the synoptic geostrophic wind velocity, i.e., where oppositely-directed events cancel each other rather than being additive as is proper for an index of rate of transfer of mechanical energy. The conclusion is the one that could have been predicted a priori, i.e., that the computation of a turbulent mixing index from a monthly mean streamline representation such as an atmospheric pressure map, is not a well-founded procedure.

Linear correlation coefficients among 12th-differenced values of the various series of indicators of this process for both areas 'A' and 'B' are presented in Table V.2. The pair of series exhibiting the highest degree of intercorrelation are the two series of averages of

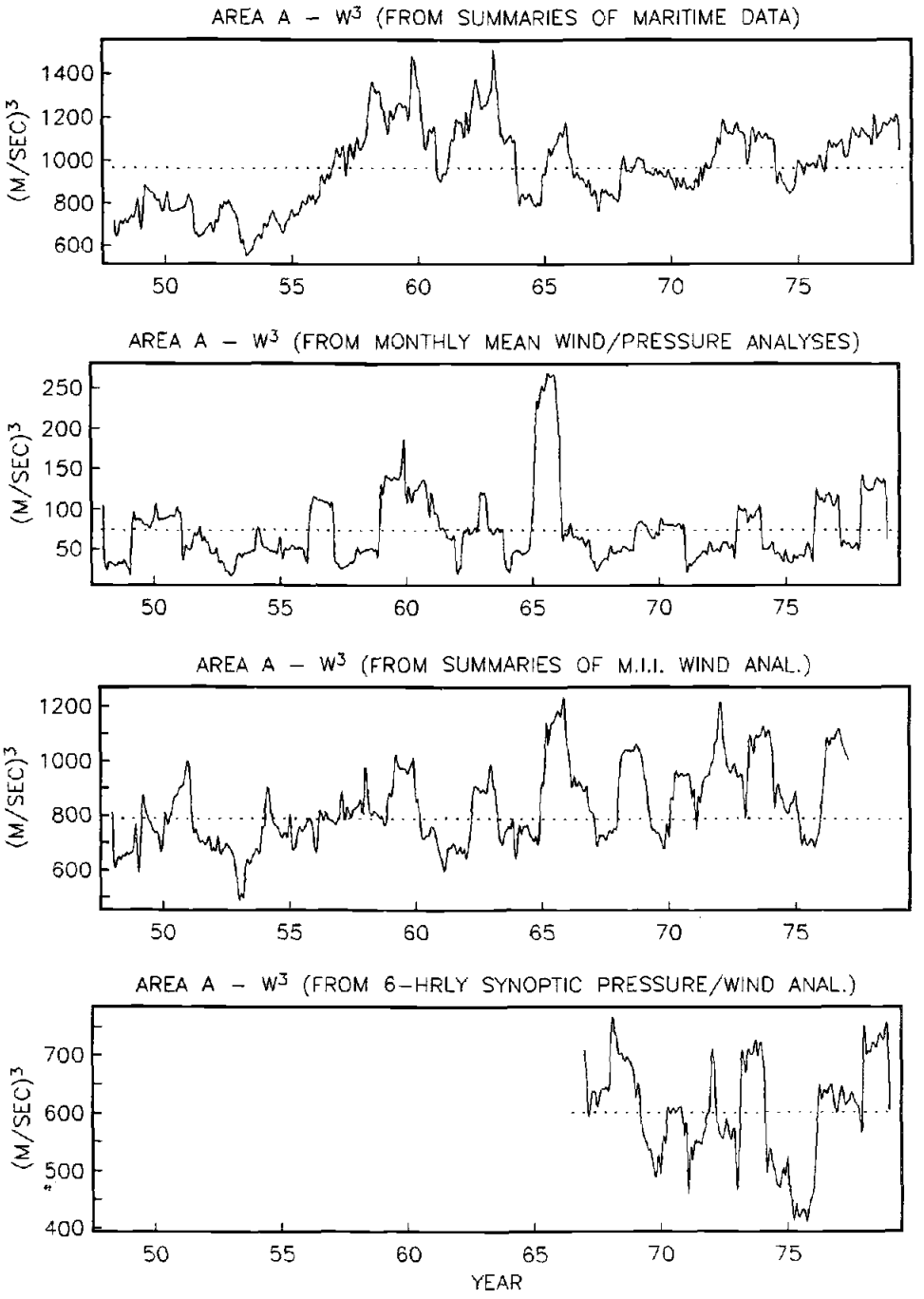

Figure V.6. 12-month running mean values of monthly series of "w^3" index of rate of addition of turbulent mixing energy to the ocean by the wind. Units are m^3 sec^{-3}. *Top panel:* series of areal summaries of computations from individual maritime reports. *Second panel:* 'mm' series computed directly from monthly means of FNOC analyzed wind/pressure fields. *Third panel:* 'MII' series produced as monthly averages of computations form synoptic "M.I.I." analyzed marine wind fields. *Bottom panel:* '6hr' series produced as monthly averages of computations from synoptic FNOC analyzed wind/pressure fields.

Table V.2. Linear correlation coefficients among various 12th-differenced series of monthly estimates of "w^3" index of rate of addition of turbulent mixing energy to the ocean by the wind, and of SST evolution in areas 'A' and 'B' (Fig.IV.1). w^3: areal summary of maritime wind reports; w^3mm: computed from monthly mean pressure/wind analysis; w^3MII: from 'M.I.I.' marine wind summaries; $w^3$6hr: monthly means of computations from 6-hourly synoptic pressure/wind analyses; dSST: areal averaged change of sea surface temperature from beginning to end of a month.

Area 'A'

	w^3	w^3mm	w^3MII	$w^3$6hr
w^3mm	.47			
w^3MII	.67	.62		
$w^3$6hr	.83	.68	.95	
dSST	-.32	-.04	-.16	-.18

Area 'B'

	w^3	w^3mm	w^3MII	$w^3$6hr
w^3mm	.47			
w^3MII	.69	.46		
$w^3$6hr	.70	.54	.91	
dSST	-.41	-.21	-.21	-.21

values computed synoptically from analyzed meteorological fields, the 'MII' and '6hr' series. The series best explaining sea surface temperature change is the series of areal summaries of maritime reports. The sign of the correlation coefficients between pairs of series of "w^3" index and SST change (Table V.2) is negative in every case; i.e., in the proper sense for cooling of the surface layer by the turbulent mixing effect.

In order to examine the trend in spring-summer turbulent mixing rate, suggested by Dickson et al. (1986), April to September mean values of the monthly "w^3" index based on areal summaries of maritme reports in area 'A' are presented in the lower panel of Fig. V.7. The trend of this index is somewhat less linear than that of the alongshore stress series (Fig. V.2). A major difference in the shapes of the series occurs in the increment from 1957 to 1962, which is characterized by a broad, highly irregular maximum in the "w^3" index, but by a relative minimum in the southward stress (or "upwelling index") in the series of alongshore stress estimates. However, the assertion of Dickson et al. (1986) that the decade of the 1950's may have been less turbulent, on the average, than the decade of the 1970's, is supported by the "w^3" index computations.

The series of April-September average scalar wind speeds, computed from the identical observational samples

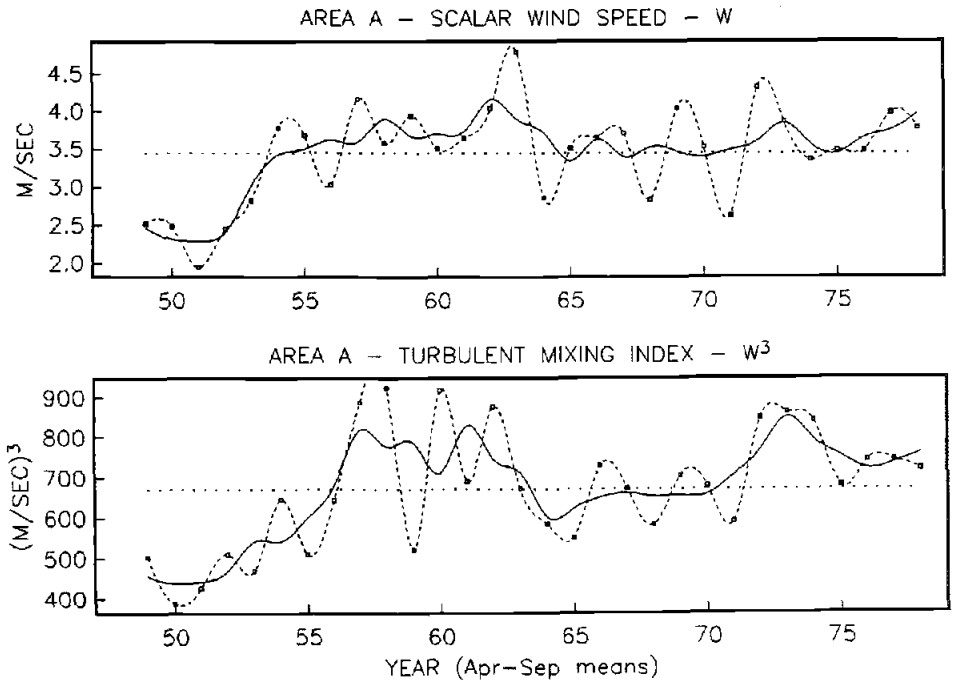

Figure V.7. April to September average values of monthly series of wind speed and "w^3" index derived from areal summaries of maritime reports. *Upper panel:* scalar wind speed (m sec^{-2}). *Lower panel:* "w^3 index (m^3 sec^{-3}). The solid line indicates the 3-year running mean.

used to compute the "w^3" index, is shown in the upper panel of Fig.V.7. The differences between the indications produced by the two series are appreciable, although the two series are obviously related. Thus, an estimate of turbulent mixing intensity based on averaged wind speed, even if it is a proper scalar average, involves the possibilty of substantial distortion in time-series properties.

V.5 Wind Stress Curl

The four time series of wind stress curl based on areal summaries of maritime reports were discussed in section IV.3 and displayed as 12-month running means in Fig. IV.5. Here we display the estimate for area 'A' compared to the corresponding 'mm' and '6hr' computations from analyzed data fields (Fig. V.8). During the period when all three series overlap, 1968-69, the agreement among them is very good, with several rather regular multi-year oscillations being indicated similarly in all three series. However, during the period previous, the 'mm' series and the maritime report series do not match nearly as well. A deep minima in 1956-57 in the maritime report-based series is not reflected at all in the 'mm' series. A peak in 1954 in the maritime report-based series corresponds to a relative minima in the 'mm' series.

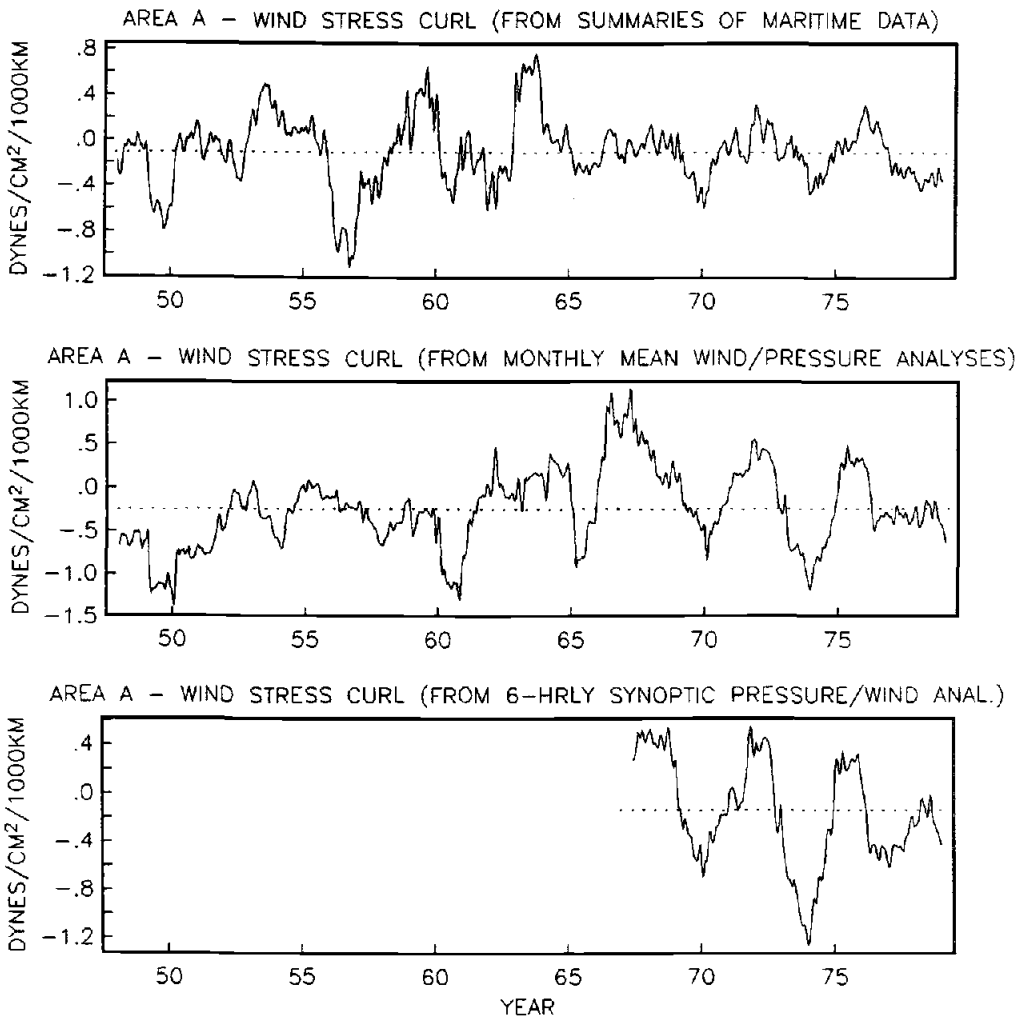

Figure V.8. 12-month running mean values of monthly series of wind stress curl for area 'A'. Units are dynes cm^{-2} per 1000 km. *Top panel:* series derived from areal summaries of maritime reports. *Second panel:* 'mm' series computed directly from monthly means of FNOC analyzed wind/pressure fields. *Bottom panel:* '6hr' series produced as monthly averages of computations from synoptic FNOC analyzed wind/pressure fields.

Although one cannot but guess as to which series may be in error in these cases, sampling error in the maritime report-based series seems a likely possibility. However, it may well be that the disagreement is mainly one of difference in scale; the 'mm' series may be reflecting a larger scale of variation. Certain of the features in the earlier parts of the two series do correspond rather well; e.g., the minima in 1949-50 and in 1960-61, etc.

Table V.3 presents linear correlation coefficients, for areas 'A' and 'B', among 12th-differenced series of the curl estimates generated from maritime report summaries and the corresponding 'mm' and '6hr' series based on meteorological analyses. The most highly intercorrelated series are the two series, 'mm' and '6hr', based on meteorological analyses. These also are the only series correlated with SST change (Table V.3); the sign of the correlation is negative which is correct for upward Ekman pumping associated with positive (cyclonic) wind stress curl to be associated with cooling of the surface layer. The correlation of wind stress curl to coastal sea level tends to be positive in the cases of the series produced from maritime report summaries, but this is likely to be largely due to the intercorrelation of these series with the alongshore stress series which were incorporated in their construction (see Tables IV.8 and IV.9). The only significant correlation found between coastal sea level and

Table V.3. Linear correlation coefficients among various 12th-differenced series of monthly estimates wind stress curl and SST evolution in areas 'A' and 'B' (Fig.IV.1), and of sea level at Vigo and Cascais. CURL: areal summary of maritime wind reports; CURLmm: computed from monthly mean pressure/wind analysis; CURL6hr: monthly means of computations from 6-hourly synoptic pressure/wind analyses; "Vigo" and "Cascais": monthly mean sea level at these stations corrected for local atmospheric pressure; "dSST": change of areal averaged sea surface temperature from beginning to end of a month.

Area 'A'

	CURL	CURLmm	CURL6hr
CURL			
CURLmm	.42		
CURL6hr	.53	.83	
Vigo	.02	-.12	-.09
dSST	.17	-.04	--

Area 'B'

	CURL	CURLmm	CURL6hr
CURL			
CURLmm	.46		
CURL6hr	.52	.87	
Cascais	.01	-.17	-.16
dSST	.29	-.24	--

a curl series computed from meteorological analyses is between the 'mm' series in area 'B' and sea level at Cascais. The significance of this negative correlation is obscure; it may be an artifact due to the correlation of wind stress curl with atmospheric pressure (Tables IV.8 and IV.9), which has been added to the raw sea level values to correct for the inverted barometer effect.

V.6 Generalizations

In the preceeding sections, differences among calculated variables designed to indicate identical processes were ascribed variously to (1) sampling errors due to differing data bases, (2) differences in spatial scale of the respective estimates, and (3) differences in the manner of averaging the data and/or in the step in the computation procedure at which the averaging is performed.

With respect to factor (2), the 'MII' series (Caton et al., 1978) appears to reflect the largest scales of any of the time series herein investigated. A substantial amount of actual nonseasonal interyear variability seems to occur on quite large scales, such that the increase in data base incorporated in a larger-scale index may more than compensate for artifacts due to incorporating increased spatial variability. However, it should be kept in mind that where the local details are of major interest, they may be lost in a larger scale description. The 'mm' and

'6hr' series (Bakun, 1973, 1975), reflect an intermediate spatial scale of variation, larger than the 5-degree latitude/longitude areal summaries. Coastal sea level correlated best with the larger scale indices of alongshore stress; SST evolution correlated best with the index series for alongshore stress and for turbulent mixing intensity which were computed on the same scale as the SST change, i.e., the 5-degree areal quadrangle scale.

With respect to factor (3), we found that it was very important to use vector-averaging or scalar-averaging as appropriate to the particular process; e.g., a series of indices of transfer of mechanical energy (such as the "w^3" index) computed from a source of vector-averaged wind data (such as represented by a monthly mean atmospheric pressure field) would probably not provide a very useful indication of variability. Distortions associated with estimating nonlinear dependencies from previously averaged data, i.e., estimating vector-average wind stress vector-average wind velocity or estimating scalar average third power of the wind speed from scalar-average wind speed, may be appreciable. However, the situation may be improved when there exists some constraint on the variance, such as where the directional variability of the wind stress is strongly constrained to parallel the coastal boundary (see Section V.2).

BIBLIOGRAPHY

Allen, J.S. 1973. Upwelling and coastal jets in a continuously stratified ocean. J. Phys. Oceanogr. 3: 245-257.

Allen, J.S. 1975. Coastal trapped waves in a stratified ocean. J. Phys. Oceanogr. 5: 300-325.

Anon. 1955. U.S. Navy Marine Climatic Atlas of the World. Volume I, North Atlantic Ocean. NAVAER 50-1-528. U.S. Gov. Print. Office, Wash. D.C. 19pp. + 275 charts.

Bakun, A. 1973. Coastal upwelling indices, west coast of North America, 1946-71. U.S. Dep. Commer. NOAA Tech. Rep. NMFS-SSRF 671. 103pp.

Bakun, A. 1975. Daily and weekly upwelling indices, west coast of North America, 1967-73. U.S. Dep. Commer. NOAA Tech. Rep. NMFS-SSRF 693. 115pp.

Bakun, A. 1978. Guinea Current upwelling. Nature 271: 147-150.

Bakun, A. 1985. Comparative studies and the recruitment problem: Searching for generalizations. CalCOFI Rep. 26: 30-40.

Bakun, A. 1986. Definition of environmental variability affecting biological processes in large marine ecosystems. p. 89-108. In: Sherman, K. and L Alexander (eds.), Variability and Management of Large Marine Ecosystems. AAAS, Wash. D.C. 319pp.

Bakun, A. 1987. Monthly variability in the ocean habitat off Peru as deduced from maritime observations, 1953-84. p. 46-74. In: D. Pauly and I. Tsukayama (eds.) The Peruvian Anchoveta and Its Upwelling Ecosystem: Three Decades of Change. ICLARM Studies and Reviews 15. Instituto del Mar del Peru (IMARPE), Callao, Peru; Deutsche Gesellschaft fur Technische Zusammenarbeit (GTZ), GmbH, Eschborn, Federal Republic of Germany; and International Center for Living Aquatic Resources Management (ICLARM), Manila, Philippines. 351pp.

Bakun, A., J. Beyer, D. Pauly, J.G. Pope, and G.D. Sharp. 1982. Ocean science in relation to living resources. Can. J. Fish. Aquat. Sci. 39: 1059-1070.

Bakun, A., D.R. McLain, and F.V. Mayo. 1974. The mean annual cycle of coastal upwelling off western North America as observed from surface measurements. Fish. Bull., U.S. 72(3): 843-844.

Bakun, A., and C.S. Nelson. 1977. Climatology of upwelling related processes off Baja California. CalCOFI Rep. 19: 107-127.

Bakun, A., and R.H. Parrish. 1980. Environmental inputs to fishery population models for eastern boundary current regions. p. 67-104. In: G.D. Sharp (ed.) Workshop on the Effects of Environmental Variation on the survival of Larval Pelagic Fishes, Lima, Peru, 20 Apr.-5 May, 1980. IOC Workshop Rep. 28: 323pp.

Beers, Y. 1953. Introduction to the Theory of Error. Addison-Wesley, Cambridge, Mass. 65pp.

Belveze, H. and K. Erzini. 1983. The influence of hydroclimatic factors on the availability of the sardine (*Sardina pilchardus*, Walbaum) in the Moroccan Atlantic fishery. p. 285-328. In: G.D. Sharp and J. Csirke (eds.) Proceedings of the Expert Consultation to Examine Changes in Abundance and Species Composition of Neritic Fish Resources. FAO Fish. Rep. 291. 1224pp.

Bowerman, B.L., and R.T. O'Connell. 1979. Time Series and Forecasting: An Applied Approach. Duxbury Press. North Scituate, Mass. 481pp.

Brunt, D. 1932. Notes on radiation in the atmosphere, I. Q.J.R. Meteorol. Soc. 58: 389-400.

Bydyko, M.I. 1956. The heat balance of the earth's surface (Teplova balans zemnoi poverkhnosti) Gidrometeorologicheskoe izdatel'stvo, Leningrad. 255p; Off. Tech. Ser., U.S. Dep. Commer., Wash. D.C., PB 131692.

Caton, F.G., M.J. Cuming, and B.R. Mendenhall. 1978. A Northern Hemisphere history of marine wind-based parameters. Technical Report MII Project M-231. (Copies available from A. Bakun, Pacific Fishereis Environmental Group, P.O. Box 831, Monterey, California 93942.) 116pp.

Chelton, D.B. 1980. Low frequency sea level variability along the west coast of North America. Ph.D. Thesis. University of California, San Diego.

Deardorff, J.W. 1968. Dependence of air-sea transfer coefficients on bulk stability. J. Geophys. Res. 73: 2549-2557.

Dickson, R.R., P.M. Kelly, J.M. Colebrook, W.S. Wooster, and D.H. Cushing. 1986. North winds and production in the eastern North Atlantic. ICES CM 1986/C:37. International Council for the Exploration of the Sea. 28pp.

Enfield, D.B. and J.S. Allen. 1980. On the structure and dynamics of monthly mean sea level anomalies along the Pacific Coast of North America. J. Phys. Oceanogr. 10: 557-578.

Evensen, A.J., and G. Veronis. 1975. Continuous representation of wind stress and wind stress curl over the world ocean. J. Mar. Res. 33, Supplement: 101-144.

Fedoseev, A. 1970. Geostrophic circulation. Rapp. P.-v. Reun. Cons. int. Explor. Mer 159: 32-37.

Fofonoff, N.P. 1962. Machine computations of mass transport in the North Pacific Ocean. J. Fish. Res. Board Can. 19: 121-1141.

Fofonoff, N.P., and C. Froese. MS. 1960. Programs for oceanographic computations and data processing on the electronic digital computer ALWAC III-E. M-1, miscellaneous programs. Fish. Res. Bd. Can. MS Rept. Oceanogr. and Limnol., No. 72. 35pp.

Gill, A.E., and Clarke, A.J. 1974. Wind-induced upwelling, coastal currents, and sea level changes. Deep-Sea Res. 21: 325-345.

Goldenberg, S.B., and J.J. O'Brien. 1981. Time and space variability of tropical Pacific wind stress. Mon. Weather Rev. 109(6): 1190-1207.

Hart, T.J. and R.I. Currie. 1960. The Benguela Current. Discovery Rep. 31: 123-298.

Hastenrath, S., and P.J. Lamb. 1977. Climatic Atlas of the Tropical Atlantic and Eastern Pacific Oceans. Univ. Wisconsin Press, Madison. 15pp. and 97 charts.

Hellerman, S. 1967. An updated estimate of the wind stress on the world ocean. Mon. Weather Rev. 95: 607-626. (See also 1968. Correction notice. Mon. Weather Rev. 96: 63-74.)

Hellerman, S., and M. Rosenstein. 1983. Normal monthly wind stress over the world ocean with error estimates. J. Phys. Oceanogr. 13: 1093-1104.

Hickey, B.M. 1979. The California Current System - hypotheses and facts. Progr. Oceanogr. 8(4): 191-279.

Hofmann, E.E., A.J. Busalacchi, and J.J. O'Brien. 1981. Wind generation of the Costa Rica Dome. Science 214: 552-554.

Holl, M.M., and B.R. Mendenhall. 1972. Fields by information blending, sea level pressure version. Fleet Numerical Weather Central Tech. Note 72-2, Monterey, Calif. 66pp.

Hughes, P., and E.D. Barton. 1974. Stratification and water mass structure in the upwelling area off northwest Africa in April/May 1969. Deep-Sea Res. 21: 611-628.

Hurlbert, H.E., and J.D. Thompson. 1973. Coastal upwelling on a beta-plane. J. Phys. Oceanogr. 6: 646-664.

Kraus, E.B. 1972. Atmosphere-ocean Interaction. Oxford Univ. Press. London. 229 pp.

Large, W.G. and S. Pond. 1981. Open ocean momentum flux measurements in moderate to strong winds. J. Phys. Oceanogr. 11: 324-336.

Large, W.G. and S. Pond. 1982. Sensible and latent heat flux measurements over the ocean. J. Phys. Oceanogr. 12: 462-482.

Lasker, R. 1978. The relationship between oceanographic conditions and larval anchovy food in the California Current: identification of factors leading to recruitment failure. Rapp. P.-v. Reun. Cons. Int. Explor. Mer. 173: 212-230.

Leetmaa, A., and A.F. Bunker. 1978. Updated charts of the mean annual wind stress, convergences in the Ekman layers, and Sverdrup transports in the North Atlantic. J. Mar. Res. 36: 311-322.

Levitus, S., and A.H. Oort. 1977. Global analysis of oceanographic data. Bull. Amer. Meteor, Soc. 58(12): 1270-1284.

Levitus, S. 1982. Climatological atlas of the world ocean. U.S. Dep. Commer. NOAA Prof. Pap. 13. 173pp.

List, R.J. 1949. Smithsonian Meteorological Tables. 6th ed. Smithson. Misc. Collec. 114. Smithsonian Institution press, Wash. D.C. 572 pp.

Lynn, R.J., K.A. Bliss, and L.E. Eber. 1982. Vertical and horizontal distributions of Seasonal mean temperature, salinity, sigma-t, stability, dynamic height, oxygen, and oxygen saturation in the California Current, 1950-1978. CalCOFI Atlas No. 30. 513pp.

Mason, J.E., and A. Bakun. 1986. Upwelling index update, U.S. West Coast, 33N-48N latitude. U.S. Dep. Commer. NOAA Tech. Memo. NMFS-SWFC-67. 82pp.

Marthaler, J.G. 1976. Comparison of sea level and currents off the Oregon Coast using mean monthly data. M.S. Thesis. Oregon State University. 64pp.

Mayr, E. 1982. The Growth of Biological Thought. Harvard Univ. Press, Cambridge, Mass. 974pp.

Mazeika, P.A. 1967. Thermal domes in the eastern tropical Atlantic Ocean. Limnol. Oceanogr. 12(3): 537-539.

McCreary, J.P., P.K. Kundu, and S.-Y. Chao. 1987. On the dynamics of the California Current system. J. Mar. Res. 45: 1-32.

McLain, D.R., R.E. Brainard, and J.G. Norton. 1985. Anomalous warm events in eastern boundary current systems. CalCOFI Rep. 26: 51-64.

Miyake, Y. 1952. A table of the saturated vapor pressure of sea water. Oceanogr. Mag. 4: 95-108.

Mittelstaedt, E. 1974. Some aspects of the circulation in the north-west African upwelling area off Cap Blanc. Tethys 6(1-2): 89-92.

Montgomery, R.B. 1938. Fluctuations in monthly sea level on Eastern U.S. Coast as related to dynamics of western North Atlantic Ocean. J. Mar. Res. 1: 165-185.

Munk, W.H. 1950. On the wind-driven ocean circulation. J. Meteor. 7: 79-93.

Murray, F.W. 1967. On the computation of saturation vapor pressure. J. Appl. Meteor. 6: 203-204.

Neter, J., and W. Wasserman. 1974. Applied Linear Statistical Models. Richard D. Irwin, Inc., Homewood, Illinois. 842pp.

Nelson, C.S. 1977. Wind stress and wind stress curl over the California Current. U.S. Dep. Commer. NOAA Tech. Rep. NMFS SSRF-714. 87pp.

Nelson, C.S., and D.M. Husby. 1983. Climatology of surface heat fluxes over the California Current region. U.S. Dep. Commer. NOAA Tech. Rep. NMFS SSRF-763. 155pp.

Nelson, G., and L. Hutchings. 1983. The Benguela upwelling area. Progr. Oceanogr. 12: 333-356.

Owen, R.W. 1980. Patterning of flow and organisms in the larval anchovy environment. p. 167-200. In: G.D. Sharp (ed.) Workshop on the Effects of Environmental Variation on the survival of Larval Pelagic Fishes, Lima, Peru, 20 Apr.-5 May, 1980. IOC Workshop Rep. 28: 323pp.

Parrish, R.H., and A.D. MacCall. 1978. Climatic variation and exploitation in the Pacific mackerel fishery. Calif. Dep. Fish Game, Fish. Bull. 167. 109pp.

Parrish, R.H., C.S. Nelson, and A. Bakun. 1981. Transport mechanisms and reproductive success of fishes in the California Current. Biol. Oceanogr. 1 (2): 175-203.

Parrish, R.H., A. Bakun, D.M. Husby, and C.S. Nelson. 1983. Comparative climatology of selected environmental processes in relation to eastern boundary current pelagic fish reproduction. p. 731-778. In: G.D. Sharp and J. Csirke (eds.) Proceedings of the Expert Consultation to Examine Changes in Abundance and Species Composition of Neritic Fish Resources. FAO Fish. Rep. 291. 1224pp.

Pattulo, J.G., W.H. Munk, R. Revelle, and E. Strong. 1955. The seasonal oscillation in sea level. J. Mar. Res. 18: 164-184.

Payne, R.E. 1972. Albedo of the sea surface. J. Atmos. Sci. 29: 959-970.

Pedlosky, J. 1974. Longshore currents, upwelling and bottom topography. J. Phys. Oceanogr. 4: 214-226.

Picaut, J. 1985. Major Dynamics Affecting the Eastern Tropical Atlantic and Pacific Oceans. CalCOFI Rep. 26: 41-50.

Reed, R.K., and D. Halpern. 1976. Observations of the California Undercurrent off Washington and Vancouver Island. Limnol. Oceanogr. 21(3): 389-398.

Reed,R.K. 1976. On estimation of long wave radiation from the oceans. J. Geophys. Res. 81: 5793-5794.

Reed,R.K. 1977. On estimating insolation over the ocean. J. Phys. Oceanogr. 7: 482-485.

Sandoval, E. 1971. The summer distribution of tuna in relation to the general oceanographic conditions off Chile and Peru. Bull. Far Seas Res. Lab. 5: 23-88.

Seckel, G.R., and F.H. Beaudry. 1973. The radiation from sun and sky over the North Pacific Ocean. (Abstr. 033.) EOS, Trans. Amer. Geophys. Un. 54: 1114.

Shannon, L.V., 1985. The Benguela ecosystem: Part 1. Evolution of the Benguela, physical features and processes. Oceanogr. Mar. Biol. Ann. Rev. 2: 105-182.

Shelton, P.A., A.J. Boyd, and M.J. Armstrong. 1985. The influence of large-scale environmental processes on neritic fish populations in the Benguela Current system. CalCOFI Rep. 26: 72-92.

Siegel, B. 1983. El Nino: the world turns topsy-turvy. The Los Angeles Times, Aug. 7, 1983: pp. 1 and 18-19.

Silva, S.N., and S. Neshyba. 1979. On the southernmost extention of the Peru-Chile Undercurrent. Deep-Sea Res. 26A: 1387-1393.

Smith, R.L. 1968. Upwelling. Oceanogr. Mar. Biol. Ann. Rev. 6: 11-46.

Smith, R.L. 1974. A description of current, wind and sea level variations during coastal upwelling off the Oregon coast, July-August 1972. J. Geophys. Res. 79: 435-443.

Smith, R.L. 1978. Poleward propagating perturbations in currents and sea levels along the Peru coast. J. Geophys. Res., 83 (C12): 6083-6092.

Stander, G.H. 1964. The pilchard of South West Africa. The Benguela Current off South West Africa. Invest. Rep. Mar. Res. Lab. S.W. Afr. 12. 122pp.

Sverdrup, H.U. 1947. Wind-driven currents in a baroclinic ocean; with application to the equatorial currents of the Eastern Pacific. Proc. Nat. Acad. Sci. 33(11): 318-326.

Sverdrup, H.U. 1953. On conditions for the vernal blooming of phytoplankton. J. Cons. int. Explor. Mer. 18: 287-295.

Tukey, J.W. 1977. Exploratory Data Analysis. Addison-Wesley, Reading, Mass. 506pp.

Wooster, W.S., and J.H. Jones. 1970. California undercurrent off Baja California. J. Mar. Res. 28(2): 235-250.

Wooster, W.S., A. Bakun, and D.R. McLain. 1976. The seasonal upwelling cycle along the eastern boundary of the North Atlantic. J. Mar. Res. 34(2): 131-141.

Wyllie, J.G. 1966. Geostrophic flow of the California Current at the surfacte and at 200 m. CalCOFI Atlas No. 4. 13pp. and 288 charts.

Wyrtki, K. 1963. The horizontal and vertical field of motion in the Peru Current. Bull. Scripps Inst. Oceanogr. 8(4): 313-346.

Wyrtki, K. 1964. Upwelling in the Costa Rica Dome. Fish. Bull. U.S. 63(2): 355-371.

Wyrtki, K. 1965. Summary of the physical oceanography of the eastern Pacific Ocean. Inst. of Mar. Res. Ref. 65-10, Scripps Inst. Oceeanogr., Univ. Calif., La Jolla. 69 pp., 9 charts.

Wyrtki, K., and G. Meyers. 1976. The trade wind field over the Pacific Ocean. J. Appl. Meteor. 15: 698-704.